Coherence Properties of the Radiation from X-ray Free Electron Lasers

E.A. Schneidmiller and M.V. Yurkov
Deutsches Elektronen Synchrotron (DESY), Hamburg, Germany

Abstract
A description of the statistical and coherence properties of the radiation from X-ray free electron lasers is one of the most complicated topics in free electron laser physics. Results of studies in this field are distributed over many papers published during the past three decades. We have made an attempt to put together all knowledge on the subject available to date. We avoid complicated mathematical derivations, and put the main emphasis on physical features and final results. Free electron laser theory has reached mature status, making it possible to present final results in an elegant form. Application of similarity techniques to the results of numerical simulations allowed us to derive universal scaling relations for the main characteristics of an X-ray free electron laser operating in the saturation regime: efficiency, coherence time, degree of transverse coherence, and pointing stability of the radiation. Statistical and coherence properties of the higher harmonics of the radiation are highlighted as well.

Keywords
Free electron laser; X-ray laser; self-amplified spontaneous emission FEL; SASE FEL; statistics; fluctuations; coherence; temporal coherence; spatial coherence; harmonics.

1 Introduction

Single-pass free electron laser (FEL) amplifiers starting from shot noise in the electron beam have been intensively developed during the last decades. An origin for this development was an idea born in the early 1980s to extend the operating wavelength range of FELs to the vacuum ultraviolet and X-ray bands [1–5]. Following the terminology of quantum lasers (amplified spontaneous emission), the term 'self-amplified spontaneous emission (SASE)' in connection with an FEL amplifier, starting from the shot noise, has been introduced in Ref. [5]. We note that this essentially quantum terminology does not reflect the physical properties of the device. In fact, FELs belong to a separate class of vacuum tube devices, and their operation is completely described in terms of classical physics (see Ref. [6] for more details).

Significant amounts of effort have been invested in the development of high brightness injectors, beam formation systems, linear accelerators, and undulators. The result was a rapid extension of the wavelength range from infrared to hard X-rays within one decade [7–18]. The first dedicated user facility, FLASH at DESY in Hamburg, has been in operation since 2005 and provides a wavelength range from 3.1 nm to 80 nm [10–16]. The Linac Coherent Light Source (LCLS) at Stanford was the first FEL operating in the hard X-ray regime, in the 0.15–1.5 nm wavelength range [17]. SACLA extended the wavelength range down to 0.06 nm [18]. The PAL X-ray free electron laser (XFEL) has produced its first light and is being commissioned at the time of writing this review [19–21]. Two other dedicated facilities are under commissioning at the moment, the European XFEL and the SwissFEL [22–24]. The main mode of operation of these facilities is SASE. One more soft X-ray FEL user facility is FERMI FEL, which uses external seeding [25].

The high-gain FEL amplifier starting from shot noise in the electron beam is a simple system consisting of a relativistic electron beam and an undulator. The FEL collective instability in the electron

beam produces an exponential growth (along the undulator) of the modulation of the electron density on the scale of the undulator radiation wavelength. The initial seed for the amplification process is fluctuation of the electron beam current. Since shot noise in the electron beam is a stochastic process, the radiation produced by a SASE FEL also possesses stochastic features. Its properties are naturally described in terms of statistical optics using notions of probability density distribution functions of the fields and intensities, correlation functions, notions of coherence time, degree of coherence, etc.

Development of the theoretical description of the coherence properties of the radiation from SASE FELs has spanned more than twenty years (see [26–45]). This subject is rather complicated, and it is worth mentioning that theoretical predictions agree well with experimental results obtained at FLASH [10–13, 46–49]. Some averaged output characteristics of SASE FELs in the framework of the one-dimensional model have been obtained [26, 27]. An approach for time-dependent numerical simulations of SASE FELs has been developed [28, 29]. Realization of this approach allowed some statistical properties of the radiation from a SASE FEL operating in linear and non-linear regimes to be obtained [30, 31]. A comprehensive study of the statistical properties of the radiation from the SASE FEL in the framework of the same model is presented in Ref. [32]. It has been shown that a SASE FEL operating in the linear regime is a completely chaotic polarized radiation source, described with Gaussian statistics. Short-pulse effects (for pulse durations comparable with the coherence time) have been studied [29, 33, 34]. An important practical result was prediction of the significant suppression of the fluctuations of the radiation intensity after a narrow-band monochromator, for the case of SASE FEL operation in the saturation regime [33]. Statistical description of the chaotic evolution of the radiation from SASE FEL has been presented [35, 36].

The first analytical studies of the problem of transverse coherence relate to the late 1980s [37, 38]. Later on, more detailed studies have been performed [39]. The problem of start-up from the shot noise has been studied analytically and numerically for the linear stage of amplification, using an approach developed in Ref. [38]. It has been found that the process of formation of transverse coherence is more complicated than that given by a naive physical picture of transverse mode selection. Namely, in the case of perfect mode selection, the degree of transverse coherence is defined by the interdependence of the longitudinal and transverse coherence. Comprehensive studies of the evolution of transverse coherence in the linear and non-linear regime of SASE FEL operation have been performed [40–43]. It has been found that the coherence time and the degree of transverse coherence reach maximum values at the end of the linear regime. Maximum brilliance of the radiation is achieved at the very beginning of the non-linear regime, which is also referred as a saturation point [41, 42]. The output power of the SASE FEL increases continuously in the non-linear regime, while the brilliance decreases after passing the saturation point.

Another important subject related to mode degeneration is fundamental limitation of the pointing stability of SASE FEL radiation. The radiation from a SASE FEL always has a limited degree of transverse coherence. When the transverse size of the electron beam significantly exceeds the diffraction limit, the mode competition effect does not provide selection of the ground mode, and spatial coherence degrades, owing to the contribution of the higher-order transverse modes. Important consequences of this effect are fluctuations of the spot size and of the pointing stability of the photon beam [50–52]. These fluctuations are fundamental and originate from the shot noise in the electron beam. The pointing instability effect becomes more pronounced for shorter wavelengths. We analyse in detail the case of an optimized SASE FEL and derive universal dependencies applicable to all operating and planned X-ray FELs. It is shown that the hard X-ray FELs driven by low-energy beams may exhibit poor spatial coherence and bad pointing stability.

Radiation of the electron beam in the planar undulator contains a rich harmonic spectrum. This refers to both incoherent and coherent radiation. Over the past years, significant research efforts have been devoted to studying the process of generation of higher harmonics in high-gain FELs [53–66]. Such an interest has mainly been driven by practical needs for prediction of the properties of XFELs. A fraction of a higher-harmonic content is very important for users planning experiments at an XFEL facility. On

the one hand, higher harmonics constitute rather harmful background for some classes of experiment. On the other hand, higher-harmonic radiation can significantly extend the operating band of the user facility. In both cases, it is highly desirable to know the properties of the higher-harmonic radiation. Analytical techniques have been used to predict properties of the higher harmonics for FEL amplifiers operating in the linear mode of operation [56,57]. However, most of the radiation power is produced in the non-linear regime, and a set of assumptions needs to be accepted in order to estimate the saturation power of higher harmonics on the base of extrapolation of analytical results. As for statistical properties, these could not be extrapolated from linear theory at all. Many studies have been performed with numerical simulation codes. These studies developed in two directions. The first direction is investigations of higher-harmonic phenomena by means of steady-state codes [58–61]. Although the results of these studies are applicable to externally seeded FEL amplifiers, it is relevant to appreciate that they gave the first predictions for high radiation power in higher harmonics of SASE FELs. Another direction was an extraction of the time structure for the beam bunching from time-dependent simulation code with subsequent use of analytical formulae of linear theory [56]. Recent studies of the mechanism of non-linear harmonic generation in SASE FEL have been presented [64,65].

This review is mainly based on our papers published during the last two decades. References to original papers of our colleagues working on the same problems are also made, and we believe that the reader can find further details therein. Analysis of higher harmonics of FEL radiation is restricted to the odd harmonics in the planar undulator. We consider only the non-linear harmonic generation mechanism. Owing to limitations of space, it was impossible to derive the results from first principles, and we decided to concentrate on a description of physical models and final results. The results themselves are strict results of FEL theory. The theory has now reached a mature status and allows rather complicated phenomena to be described in an elegant way. In addition, we widely use application of the similarity techniques to the results of numerical simulations. This allowed us to describe the saturation regime in detail, which is important from a practical point of view. Universal formulae that can be used in practical calculation are distributed across the text, which can be inconvenient for the reader. The review proceeds as follows. In Section 2, we present general statistical properties of SASE FEL radiation. We show that a SASE FEL operating in the exponential growth regime can be described by Gaussian statistics, and that properties of the radiation correspond to the properties of completely chaotic polarized light. In the framework of the one-dimensional model, in Section 3, we describe temporal properties of the radiation. Topics related to spatial coherence are described in Section 4, in the framework of three-dimensional FEL theory. Essential practical formulae are collected in Appendices A and B for the results of the one-dimensional and three-dimensional FEL theory, respectively. Finally, Appendix C describes statistical techniques for measurements of the main parameters of SASE FEL radiation. This is an extremely powerful technique allowing measurement of the FEL parameter ρ, coherence time, photon pulse duration, number of longitudinal and transverse modes, and degree of transverse coherence. It is based on fundamental principles, and measured values have strict physical meaning.

2 General properties of SASE FEL radiation

The amplification process in the SASE FEL starts from the shot noise in the electron beam; then it passes the stage of exponential amplification (high-gain linear stage) and finally enters saturation stage (see Fig. 1). At the initial stage of amplification, coherence properties are poor, and the radiation consists of a large number of transverse and longitudinal modes [6,67–73]. In the exponential stage of amplification, transverse modes with higher gain dominate over modes with lower gain as the undulator length progresses. This feature is also known as the mode competition process. Longitudinal coherence also improves in the high-gain linear regime [32,64,71]. The mode selection process stops at the onset of the non-linear regime, and maximum values of the degree of transverse coherence and the coherence time are reached at this point. If one traces the evolution of the brilliance of the radiation along the undulator length, there is always a point, which we define as the saturation point, where the brilliance reaches a
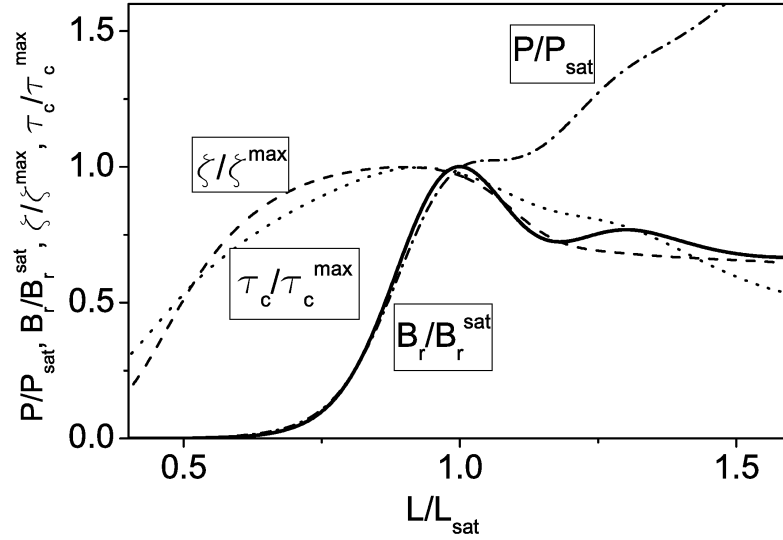
Fig. 1: Evolution of main characteristics of SASE FEL along the undulator: brilliance (solid line), radiation power (dash-dotted line), degree of transverse coherence (dashed line), and coherence time (dotted line). Brilliance and radiation power are normalized to saturation values. Coherence time and degree of transverse coherence are normalized to the maximum values. Undulator length is normalized to saturation length. The plot has been derived from the parameter set corresponding to $\hat{\epsilon} = 1$. Calculations made with simulation code FAST [77].

maximum value [41, 42]. The undulator length to saturation is in the range from about nine (hard X-ray SASE FELs) to eleven (visible-range SASE FELs) field gain lengths L_g [41, 42]. Figures 2 and 3 show the evolution of the temporal and spectral structure of the radiation pulse along the undulator: at $0.5L_g$ (beginning of the undulator), $5L_g$ (high-gain linear regime), and $10L_g$ (saturation regime). Figure 4 shows snapshots of the intensity distributions across a slice of the photon pulse. We see that many transverse radiation modes are excited when the electron beam enters the undulator. The radiation field generated by a SASE FEL consists of wavepackets (spikes [29]) which originate from fluctuations of the electron beam density. The typical length of a spike is approximately the coherence length. The spectrum of the SASE FEL radiation also exhibits a spiky structure. The spectrum width is inversely proportional to the coherence time, and a typical width of a spike in a spectrum is inversely proportional to the pulse duration. The amplification process selects a narrow band of the radiation, the coherence time increases, and the spectrum shrinks. Transverse coherence is also improved, owing to the mode selection process (Eq. (25)).

Figure 5 shows probability distributions of the instantaneous power density $I \propto |\tilde{E}|^2$ (top) and the instantaneous radiation power $P \propto \int I(\vec{r}_\perp)d\vec{r}_\perp$ (bottom). We see that transverse and longitudinal distributions of the radiation intensity exhibit rather chaotic behaviour. However, probability distributions of the instantaneous power density I and of the instantaneous radiation power P look more elegant and seem to be described by simple functions. The origin of this fundamental simplicity relates to the properties of the electron beam. The shot noise in the electron beam has a statistical nature that significantly influences the characteristics of the output radiation from a SASE FEL. Fluctuations of the electron beam current density serve as input signals in a SASE FEL. These fluctuations always exist in the electron beam, owing to the effect of shot noise. Initially, fluctuations are not correlated in space and time, but when the electron beam enters the undulator, beam modulation at frequencies close to the resonance frequency of the FEL amplifier initiates the process of the amplification of coherent radiation.
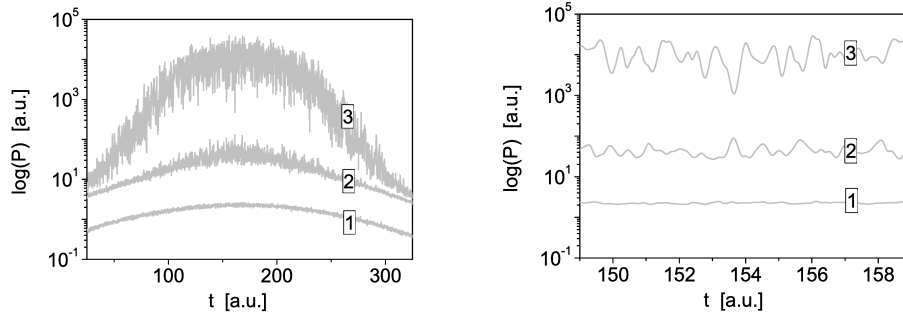
Fig. 2: Temporal structure of the radiation pulse at different undulator lengths. Indexes 1, 2, and 3 correspond to undulator lengths of $0.5L_\mathrm{g}$, $5L_\mathrm{g}$, and $10L_\mathrm{g}$, respectively. The plot in the right panel is an enlarged portion of the plot in the left panel. Calculations made using simulation code FAST [77].
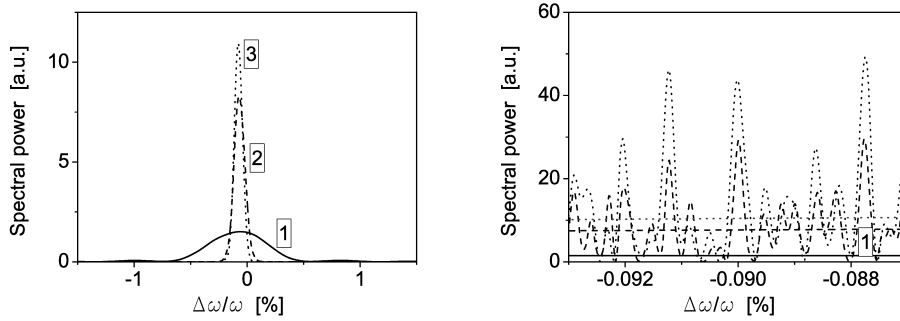

Fig. 3: Spectral structure of the radiation pulse at different undulator lengths. Solid, dashed, and dotted lines correspond to undulator lengths of $0.5L_\mathrm{g}$, $5L_\mathrm{g}$, and $10L_\mathrm{g}$, respectively. Left: envelope of the radiation spectrum. Right: enlarged portion of the radiation spectrum. Calculations made with simulation code FAST [77].
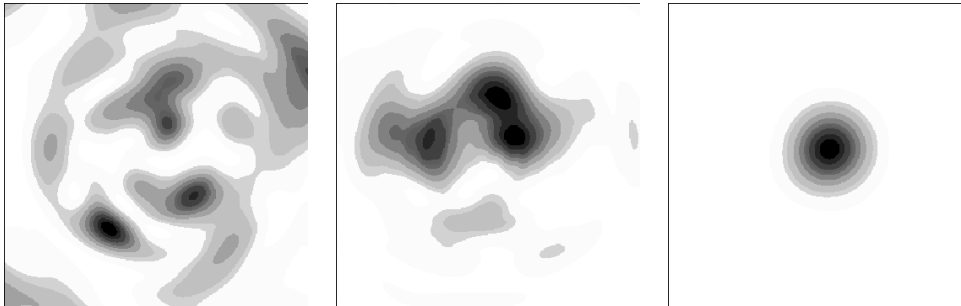

Fig. 4: Snapshots of the power density distribution in a slice at an undulator length of (left) $0.5L_\mathrm{g}$, (middle) $5L_\mathrm{g}$, and (right) $10L_\mathrm{g}$. Calculations made with simulation code FAST [77].

Let us consider a microscopic picture of the electron beam current at the entrance of the undulator. The electron beam current consists of moving electrons randomly arriving at the entrance of the undulator:

$$I(t) = (-e) \sum_{k=1}^{N} \delta(t - t_k) \,,$$

where $\delta(\ldots)$ is the delta function, $(-e)$ is the charge of the electron, N is the number of electrons in a bunch and t_k is the random arrival time of the electron at the undulator entrance. The electron beam
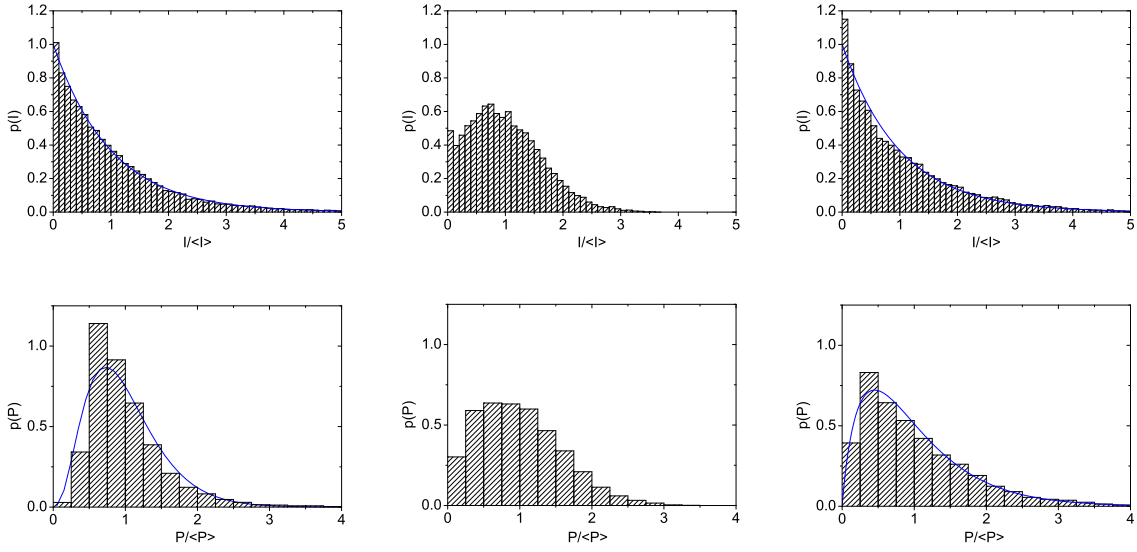
Fig. 5: Probability density distributions of (top) instantaneous power density $I = |\tilde{E}|^2$ and (bottom) instantaneous radiation power P from a SASE FEL at different stages of amplification: linear regime, saturation regime, and deep non-linear regime (undulator lengths, $5L_g$, $10L_g$, and $15L_g$, respectively). Top: solid lines on the power density histograms represent negative exponential distribution (Eq. (2)). Bottom: solid lines on power histograms represent gamma distribution (Eq. (3)) with $M = 1/\sigma_P^2$. $\hat{\epsilon} = 2$. Calculations made with simulation code FAST [77].

current $I(t)$ and its Fourier transform $\bar{I}(\omega)$ are:

$$I(t) = (-e) \sum_{k=1}^{N} \delta(t - t_k) = \frac{1}{2\pi} \int_{-\infty}^{\infty} \bar{I}(\omega) e^{-i\omega t} d\omega \,,$$

$$\bar{I}(\omega) = \int_{-\infty}^{\infty} e^{i\omega t} I(t) dt = (-e) \sum_{k=1}^{N} e^{i\omega t_k} \,. \tag{1}$$

It follows from Eq. (1) that the Fourier transformation of the input current, $\bar{I}(\omega)$, is the sum of large number of complex phasors with random phases $\phi_k = \omega t_k$. Thus, harmonics of the electron beam current can be described with Gaussian statistics.

The FEL process is simply an amplification of the initial shot noise in the narrow band near the resonance wavelength λ when both harmonics of the beam current and radiation are increasing. An FEL amplifier operating in the linear regime is simply a linear filter, and the Fourier harmonic of the radiation field is simply proportional to the Fourier harmonic of the electron beam current, $\bar{E}(\omega) = H_A(\omega - \omega_0)\bar{I}(\omega)$. Thus, the statistics of the radiation are Gaussian—the same as of the shot noise in the electron beam. This kind of radiation is usually referred to as completely chaotic polarized light, a well-known object in the field of statistical optics [74]. For instance, the higher-order correlation functions (time and spectral) are expressed via the first-order correlation function. The spectral density of the radiation energy and the first-order time correlation function form a Fourier transform pair (Wiener–Khinchin theorem). The real and imaginary parts of the slowly varying complex amplitudes of the electric field of the electromagnetic wave, $\tilde{E}$, have a Gaussian distribution. The instantaneous power density, $I = |\tilde{E}|^2$, fluctuates in accordance with the negative exponential distribution (see Fig. 5):

$$p(I) = \frac{1}{\langle I \rangle} \exp\left(-\frac{I}{\langle I \rangle}\right) \,. \tag{2}$$

Any integral of the power density, such as radiation power P (or radiation pulse energy E), fluctuates in accordance with the gamma distribution:

$$p(P) = \frac{M^M}{\Gamma(M)} \left(\frac{P}{\langle P \rangle} \right)^{M-1} \frac{1}{\langle P \rangle} \exp \left(-M \frac{P}{\langle P \rangle} \right) . \tag{3}$$

where $\Gamma(M)$ is the gamma function, with argument $M = 1/\sigma_P^2$, and $\sigma_P^2 = \langle (P - \langle P \rangle)^2 \rangle / \langle P \rangle^2$ is the relative dispersion of the radiation power. For completely chaotic polarized light, the parameter M has a clear physical interpretation—it is the number of modes [6]. Thus, the relative dispersion of the radiation power directly relates to the coherence properties of the SASE FEL operating in the linear regime.

When the amplification process enters a non-linear stage and reaches saturation, the statistics of the radiation significantly deviate from Gaussian. A particular signature of this change is illustrated in Fig. 5. We see that the probability distribution of the radiation intensity is not negative exponential, and that the probability distribution of the radiation power visibly deviates from a gamma distribution. As yet, there is no analytical description of the statistics in the saturation regime, and we refer the reader to the analysis of the results of numerical simulations [41]. A general feature of the saturation regime is that fluctuations in radiation intensity are significantly suppressed. When we trace the amplification process further in the non-linear regime, we find that fluctuations of the radiation intensity and radiation power increase, and that relevant probability distributions tend to those given by Eqs. (2) and (3). This behaviour hints that the properties of the radiation from a SASE FEL operating in the deep non-linear regime tend to be those of completely chaotic polarized light [32, 41].

Another practical problem refers to the probability distributions of the radiation intensity in the frequency domain, like that filtered by a monochromator. For SASE FEL radiation produced in the linear regime, the probability distribution radiation intensity is defined by Gaussian statistics, and it is negative exponential for a narrow-band monochromator. When the amplification process enters the saturation regime, this property still holds for the case of long electron pulses [6, 32] but is violated significantly for the case of short electron bunches, approximately equal to or less than the coherence length. In the latter case, fluctuations of the radiation intensity after the narrow-band monochromator are significantly suppressed, as has been predicted theoretically and measured experimentally at the FLASH FEL at DESY, operating in a femtosecond mode [33, 46].

All these considerations are related to the fundamental harmonic of the SASE FEL radiation. Radiation from a SASE FEL with a planar undulator has rich harmonics contents. Intensities of even harmonics are suppressed [75], but odd harmonics provide visible contribution to the total radiation power [53–65]. Comprehensive studies of the statistical properties of the odd harmonics have been conducted [64]. It has been found that the statistics of the high-harmonic radiation from the SASE FEL changes significantly with respect to the fundamental harmonic (with respect to Gaussian statistics). For the fundamental harmonic, the probability density function of the intensity is the negative exponential distribution: $p(W) = \langle W \rangle^{-1} \exp(-W/\langle W \rangle)$. The mechanism of higher-harmonic generation is equivalent to the transformation of the intensity W as $z = (W)^h$, where h is the harmonic number. It has been shown [64] that the probability distribution for the intensity of the hth harmonic is given by:

$$p(z) = \frac{z}{h \langle W \rangle} z^{(1-h)/h} \exp(-z^{1/h}/\langle W \rangle) . \tag{4}$$

The expression for the mean value is $\langle z \rangle = h! \langle W \rangle^h$. Thus, the hth-harmonic radiation for the SASE FEL has an intensity level roughly $h!$ times larger than the corresponding steady-state case, but with more shot-to-shot fluctuations than the fundamental [56]. The non-trivial behaviour of the intensity of the high harmonics reflects the complicated non-linear transformation of the fundamental harmonic statistics. In this case, Gaussian statistics are no longer valid. Practically, this behaviour occurs only at the very end of a high-gain exponential regime when coherent radiation intensity exceeds incoherent radiation intensity. When amplification enters the non-linear stage, probability distributions change dramatically on the scale

of the gain length, and in the saturation regime (and further downstream the undulator) the probability distributions of the radiation intensity of higher harmonics are already close to the negative exponential distribution [64].

2.1 Definitions of the statistical properties of radiation

In the proceeding sections we present a systematic description of the main statistical properties of SASE FEL radiation. We describe the radiation in terms of statistical optics [74]. Longitudinal and transverse coherence are described in terms of correlation functions. The first-order time correlation function, $g_1(t, t')$, is defined as:

$$g_1(\vec{r}, t - t') = \frac{\langle \tilde{E}(\vec{r}, t) \tilde{E}^*(\vec{r}, t') \rangle}{\left[\langle | \tilde{E}(\vec{r}, t) |^2 \rangle \langle | \tilde{E}(\vec{r}, t') |^2 \rangle \right]^{1/2}} . \tag{5}$$

For a stationary random process, the time correlation functions are dependent on only one variable, $\tau = t - t'$. The coherence time is defined as [6, 76]:

$$\tau_{\rm c} = \int_{-\infty}^{\infty} |g_1(\tau)|^2 {\rm d}\tau . \tag{6}$$

The transverse coherence properties of the radiation are described in terms of the transverse correlation functions. The first-order transverse correlation function is defined as:

$$\gamma_1(\vec{r}_\perp, \vec{r'}_\perp, z, t) = \frac{\langle \tilde{E}(\vec{r}_\perp, z, t) \tilde{E}^*(\vec{r'}_\perp, z, t) \rangle}{\left[\langle | \tilde{E}(\vec{r}_\perp, z, t)|^2 \rangle \langle | \tilde{E}(\vec{r'}_\perp, z, t)|^2 \rangle \right]^{1/2}} ,$$

where $\tilde{E}$ is the slowly varying amplitude of the amplified wave, $E = \tilde{E}(\vec{r}_\perp, z, t) e^{i\omega_0(z/c - t)} + \text{C.C.}$ We consider the model of a stationary random process, meaning that γ_1 does not depend on time. Following Ref. [41], we define the degree of transverse coherence as:

$$\zeta = \frac{\int |\gamma_1(\vec{r}_\perp, \vec{r'}_\perp)|^2 I(\vec{r}_\perp) I(\vec{r'}_\perp) {\rm d}\vec{r}_\perp {\rm d}\vec{r'}_\perp}{\left[\int I(\vec{r}_\perp) {\rm d}\vec{r}_\perp \right]^2} , \tag{7}$$

where $I \propto |\tilde{E}|^2$ is the radiation intensity.

An important figure of merit of the radiation source is the degeneracy parameter δ, the number of photons per mode (coherent state). Note that when $\delta \gg 1$, classical statistics are applicable, while a quantum description of the field is necessary as soon as δ is comparable to (or less than) one. Using the definitions of the coherence time (Eq. (6)) and of the degree of transverse coherence (Eq. (7)), we define the degeneracy parameter as

$$\delta = \dot{N}_{\rm ph} \tau_{\rm c} \zeta , \tag{8}$$

where $\dot{N}_{\rm ph}$ is the photon flux. The peak brilliance of the radiation from an undulator is defined as a transversely coherent spectral flux:

$$B_{\rm r} = \frac{\omega {\rm d} \dot{N}_{\rm ph}}{{\rm d}\omega} \frac{\zeta}{(\lambda/2)^2} = \frac{4\sqrt{2} c \delta}{\lambda^3} . \tag{9}$$

When deriving the right-hand term of the equation, we used the fact that the spectrum shape of SASE FEL radiation in a high-gain linear regime and near saturation is close to Gaussian [6]. In this case, the r.m.s. spectrum bandwidth σ_ω and coherence time obey the equation $\tau_{\rm c} = \sqrt{\pi}/\sigma_\omega$.

3   Temporal coherence of SASE FEL radiation

In this section, we present a comprehensive study of the phenomena related to the temporal coherence of SASE FEL radiation. The study is performed in the framework of the one-dimensional model with time-dependent simulation code FAST [6, 77]. We restrict our study to odd harmonics produced in the SASE FEL. We omit from consideration an effect of self-consistent amplification of the higher harmonics [56, 66]. In other words, we solve only the electrodynamic problem, assuming that particle motion is governed by the fundamental harmonic. The latter approximation is valid when the power in higher harmonics is much less than in the fundamental. We apply similarity techniques to the results of numerical simulations and derive universal relations describing general properties of the odd harmonics in the SASE FEL: power, statistical, and spectral properties. The results are illustrated for the first, third, and fifth harmonics having practical importance for X-ray FELs.

We consider planar undulator with the magnetic field:

$$H_z(z) = H_{\mathrm{w}} \cos(2\pi z/\lambda_{\mathrm{w}}) \,,$$

where λ_{w} is undulator period, and H_{w} is the peak magnetic field. In the SASE FEL, the radiation is produced by the electron beam during a single pass of the undulator. The amplification process starts from shot noise in the electron beam. During the amplification process, a powerful, coherent radiation is produced, having narrow-band near-resonance wavelength:

$$\lambda_0 = \frac{\lambda_{\mathrm{w}}}{2\gamma^2}(1 + K^2) \,, \tag{10}$$

where $K = e\lambda_{\mathrm{w}} H_{\mathrm{w}}/(2\sqrt{2}\pi mc^2)$ is the r.m.s. undulator parameter, γ is relativistic factor, and $(-e)$ and m are the charge and mass of an electron, respectively.

In the framework of the one-dimensional model, we consider amplification of the plane electromagnetic wave by the electron beam in the undulator. When space charge and energy spread effects can be neglected, operation of an FEL amplifier is described in terms of the gain parameter Γ and efficiency parameter (or FEL parameter) ρ (see, e.g. [4, 6]):

$$\rho = \frac{\lambda_{\mathrm{w}}}{4\pi} \left[\frac{4\pi^2 j_0 K^2 A_{\mathrm{JJ}}^2}{I_{\mathrm{A}} \lambda_{\mathrm{w}} \gamma^3} \right]^{1/3} \,, \qquad \Gamma = \frac{4\pi\rho}{\lambda_{\mathrm{w}}} \,. \tag{11}$$

Here, j_0 is the beam current density, $I_{\mathrm{A}} = mc^3/e \simeq 17$ kA, and $\omega = 2\pi c/\lambda$ is frequency of electromagnetic wave. The coupling factor K_h is given by

$$K_h = K(-1)^{(h-1)/2} \left[J_{(h-1)/2}(Q) - J_{(h+1)/2}(Q) \right] \,, \tag{12}$$

where $Q = K^2/[2(1 + K^2)]$. The FEL amplifier is a resonance device with an amplification bandwidth of about $\Delta\omega/\omega_0 \simeq 2\rho$ around the resonance frequency $\omega_0 = 2\pi c/\lambda_0$. In the linear stage of amplification, the radiation power W increases exponentially along the undulator length, $W \propto \exp[2z/L_{\mathrm{g}}]$, and the field gain length is about $L_{\mathrm{g}} \simeq 2/(\Gamma\sqrt{3})$. Saturation of the FEL amplifier occurs when relative energy loss by the electrons at one field gain length is approximately equal to the saturation parameter ρ.

A complete description of the start-up from shot noise in the FEL amplifier can be made only with time-dependent simulations of the FEL process. We do not present here general technical details of the time-dependent simulations; they are described in detail elsewhere [6, 77]. Details related to the particle loading tool can be found in Ref. [78]. We note merely that, within the accepted approximation (the particle's dynamics are governed by the fundamental harmonic), we can simply calculate the odd harmonics from the particle distribution, and the amplitude of the electric field scales as

$$E(z, t) \propto K_h \int\limits_0^z a_h(z', t - z'/c)\mathrm{d}z' \,, \tag{13}$$

where a_h is the hth harmonic of the beam bunching. Thus, we find that the coupling factor K_h, and the time-dependent integral of the beam bunching are factorized. This allows us to extract the universal ratio of the power of higher harmonics to the power of the fundamental harmonic.

3.1 Statistical properties of the odd harmonics of the radiation from SASE FEL

In this section, we present the results of numerical studies of the operation of the SASE FEL in the linear and non-linear regimes. In the framework of the accepted model, the input parameter of the system is the number of cooperating electrons $N_c = I/(e\rho\omega_0)$, where I is the beam current. Most of the statistical characteristics of the SASE FEL process are functions of N_c, only at fixed z coordinate [6, 32]. A typical range of the values of N_c is 10^6–10^9 for the SASE FELs of wavelength range from X rays to the infrared. The numerical results presented in this section, are calculated for the value $N_c = 3 \times 10^7$, which is typical for a vacuum ultraviolet FEL. It is worth mentioning that the dependence of the output parameters of the SASE FEL on the value of N_c is rather weak, in fact logarithmic. Therefore, the obtained results are pretty general and can be used for the estimation of the parameters of actual devices with sufficient accuracy.

3.1.1 Temporal characteristics

Figure 6 presents a typical time structure of the first and the third harmonic of the radiation from a SASE FEL at different undulator lengths $\hat{z} = \Gamma z = 10$–13. The normalized power of the hth harmonic is defined as $\hat{\eta}_h = \langle W_h \rangle \times (K_1/K_h)^2/(\rho W_b)$. Here, $\langle W_h \rangle$ is averaged radiation power in the hth harmonic, and $W_b = \gamma mc^2 I/e$ is the electron beam power. The longitudinal coordinate along the pulse is $\hat{s} = \rho\omega_0(z/\bar{v}_z - t)$, and $\bar{v}_z = v - cK^2/(2\gamma^2)$ is the velocity of the electron along the z axis, averaged over the undulator period. The head of the pulse is located in the positive direction of $\hat{s}$. The plot for the averaged power of the first harmonic is shown in Fig. 7 with a solid line. It can be seen that saturation is achieved at the undulator $\hat{z} = 13$. The saturation length is described well in terms of the number of cooperating electrons N_c [6, 32]:

$$\hat{z}_{\text{sat}} \simeq 3 + \frac{1}{\sqrt{3}} \ln N_c \ . \tag{14}$$

The normalized efficiency at saturation, $\hat{\eta}_{\text{sat}} = \langle W_{\text{sat}} \rangle/(\rho W_b) \simeq 1.08$, is almost independent of the value of N_c. The dashed and dotted lines in the figure show a normalized power ratio, $\hat{\eta}_h/\hat{\eta}_1 = (\langle W_h \rangle/\langle W_1 \rangle) \times (K_1/K_h)^2$, for the third and fifth harmonics. One can notice that the power of the higher harmonics is greater than the shot noise level only at the end of the linear regime. This becomes clear if one takes into account the fact that the shot noise level of the beam bunching is about $1/\sqrt{N_c}$. We consider an example typical for a vacuum ultraviolet FEL with $N_c = 3 \times 10^7$, which corresponds to the shot noise beam bunching $a \simeq 2 \times 10^{-4}$. When the FEL amplifier operates in the linear regime, odd harmonics increase as a_1^h, and we expect from this simple physical estimate that coherent contribution into higher harmonics can exceed the shot noise level only for the values of the beam bunching at the fundamental harmonic $a_1 \gtrsim 0.1$, i.e. at the end of the linear regime. Note that the shot noise level increases when approaching the X-ray region.

The plots presented in Fig. 6 allow the evolution of the third harmonic power to be traced from $\hat{z} = 10$ (when it just starts to exceed the shot noise level) up to saturation point $\hat{z} = 13$. At $\hat{z} = 10$–11, the SASE FEL operates in the high-gain linear regime, and the beam bunching in the fundamental harmonic is small, $|a_1| \ll 1$. In this case, one can expect the well-known mechanism of the higher-harmonic generation, i.e. $a_h \propto a_1^h$, and the spikes of the third harmonic radiation become rather pronounced. However, the noisy nature of the SASE FEL makes a big difference to the behaviour of the growth rates with respect to predictions given in the framework of steady-state simulations [58, 59]. Analysing the plot for the power growth rate (see Fig. 8) we can state that, in practical situations, the prediction of the steady-state theory (the growth rate of higher harmonics is proportional to the harmonic number) is valid only for the third harmonic, and then only on a short piece of undulator close to saturation, of about one
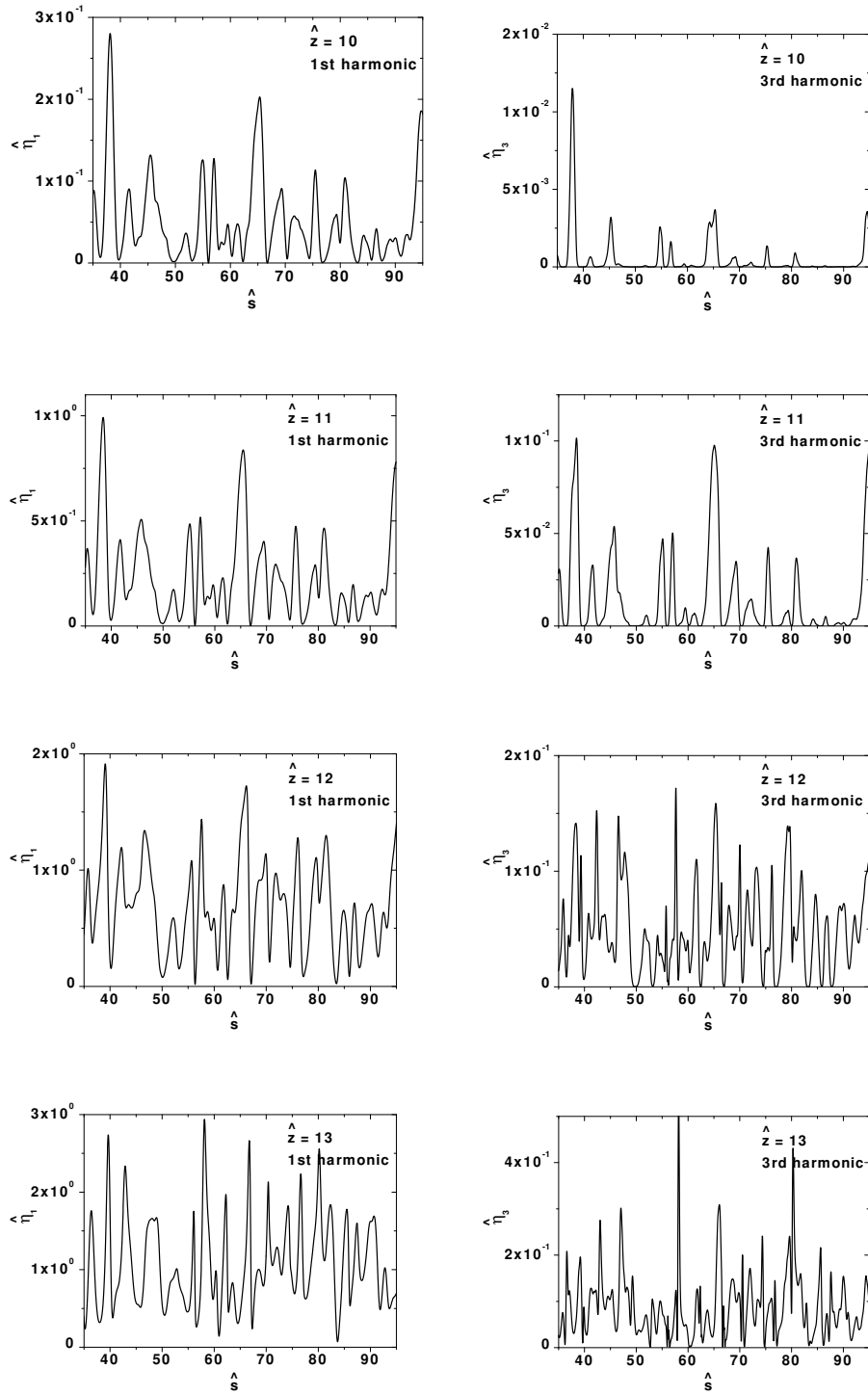
Fig. 6: Normalized power in the radiation pulse versus $\hat{s} = \rho\omega_0(z/\bar{v}_z - t)$ at different lengths of the FEL amplifier $\hat{z} = 10$–13. Left and right columns correspond to the fundamental and third harmonic, respectively. Calculations made with simulation code FAST [77].
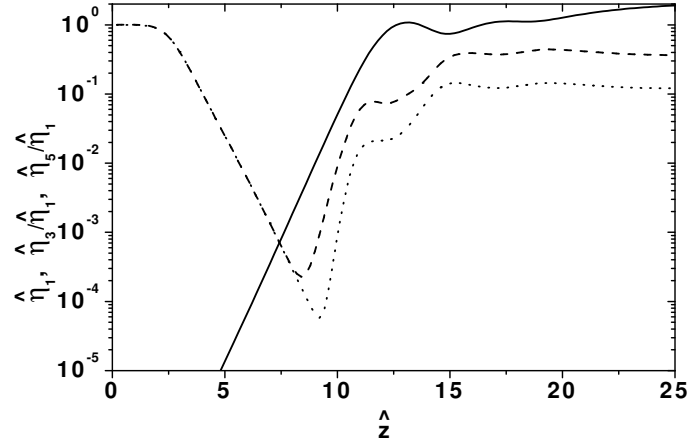
549

Fig. 7: Normalized averaged power of a fundamental harmonic of SASE FEL, $\hat{\eta}_1 = P_1/(\rho P_{\mathrm{beam}})$, as a function of a normalized undulator length (solid line). Dashed and dotted lines show normalized power ratio, $\hat{\eta}_h/\hat{\eta}_1 = (W_h/W_1) \times (K_1/K_h)^2$ for the third and fifth harmonics, respectively. Calculations made with simulation code FAST [77].
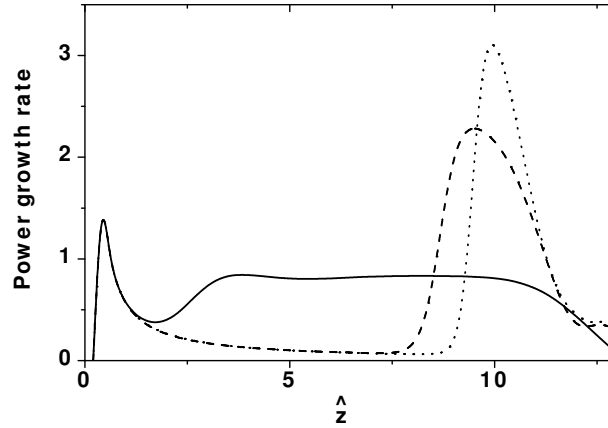
Fig. 8: Normalized power growth rate for the first, third, and fifth harmonic (solid, dashed, and dotted line, respectively). Calculations made with simulation code FAST [77].

gain length. Also, a prediction for the relation between averaged values of the beam bunching at the third harmonic, $< |a_3|^2 >= 6 < |a_1|^2 >^3$, holds only approximately, and is strongly violated for higher harmonics, because of the strong contribution of the shot noise. This feature of the SASE FEL has been highlighted qualitatively in early papers [56] with the analysis of simulation results obtained with code GINGER [55]. Here we simply present a more quantitative study.

The plots in Fig. 7 present a general result for a ratio of the power in the higher harmonics with respect to the fundamental one. For the saturation, we find a universal dependency:

$$\frac{\langle W_3 \rangle}{\langle W_1 \rangle}|_{\mathrm{sat}} = 0.094 \times \frac{K_3^2}{K_1^2} , \qquad \frac{\langle W_5 \rangle}{\langle W_1 \rangle}|_{\mathrm{sat}} = 0.03 \times \frac{K_5^2}{K_1^2} . \tag{15}$$
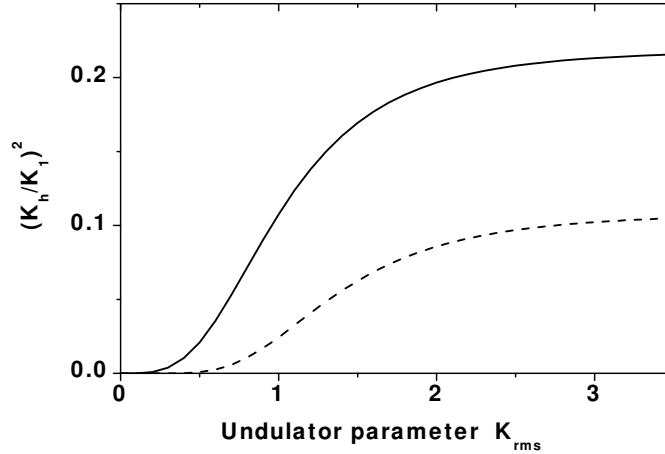
Fig. 9: Ratio of coupling factors, $(K_h/K_1)^2$, for the third (solid line) and the fifth (dashed line) harmonics with respect to the fundamental harmonic versus the r.m.s. value of undulator parameter $K_{\rm rms}$. Calculations made with simulation code FAST [77].

Universal functions for the ratio $(K_h/K_1)^2$ are plotted in Fig. 9. Asymptotic values for large values of the undulator parameter are $(K_3/K_1)^2 \simeq 0.22$ and $(K_5/K_1)^2 \simeq 0.11$. Thus, we can state that the contribution of the third harmonic into the total radiation power of SASE FEL at saturation could not exceed a level of 2%. Thus, its influence on the beam dynamics should be small. This result justifies a basic assumption used for derivation of a universal relation, Eq. (15). A contribution of the fifth harmonic to the total power at saturation could not exceed the value of 0.3%.

Another important topic is an impact of the electron beam quality on the non-linear harmonic generation process. In the framework of the one-dimensional theory, this effect is described by the energy spread parameter $\hat{\Lambda}_{\rm T}^2$ [6]:

$$\hat{\Lambda}_{\rm T}^2 = \frac{\langle (\Delta E)^2 \rangle}{\rho^2 E_0^2} \,,$$

where $\langle (\Delta E)^2 \rangle$ is the r.m.s. energy spread and $E_0 = \gamma m c^2$ is the nominal energy of the electrons. Thus, the result given by Eq. (15) is generalized to the case of finite energy spread with the plot presented in Fig. 10. We see that the energy spread in the electron beam suppresses the power of the higher harmonics. Within the practical range of $\hat{\Lambda}_{\rm T}^2$, this suppression can be about a factor of three for the third harmonic, and about an order of magnitude for the fifth harmonic. For practical estimates, one should use an effective value of the energy spread, describing the contribution of the energy spread and the emittance to the longitudinal velocity spread [6]:

$$\frac{\langle (\Delta E)^2 \rangle_{\rm eff}}{E_0^2} = \frac{\langle (\Delta E)^2 \rangle}{E_0^2} + \frac{2\gamma_z^4 \epsilon^2}{\beta^2} \,,$$

where γ_z is the longitudinal relativistic factor ($\gamma_z^2 = \gamma^2/(1 + K^2)$), ϵ is the beam emittance, and β is the focusing beta function. The plot in Fig. 10 covers the practical range of parameters for X-ray FELs. The saturation length at $\hat{\Lambda}_{\rm T}^2 = 0.5$ is increased by a factor of 1.5 with respect to the 'cold' beam case $\hat{\Lambda}_{\rm T}^2 = 0$.
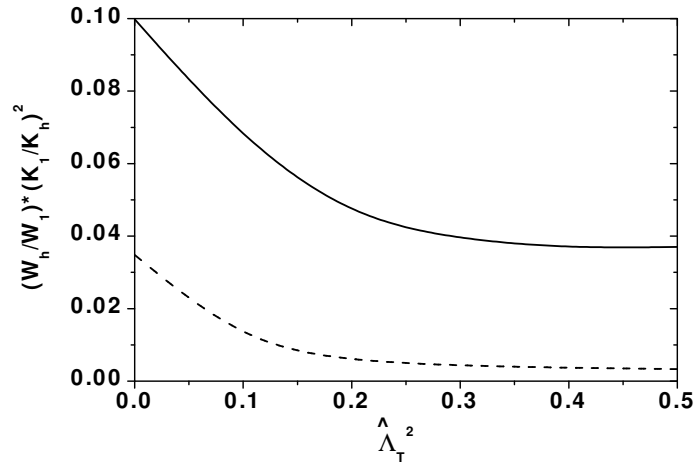
Fig. 10: Normalized power ratio at saturation, $(W_h/W_1) \times (K_1/K_h)^2$, for the third (solid line) and fifth (dashed line) harmonic as a function of energy spread parameter $\hat{\Lambda}_{\mathrm{T}}^2$. SASE FEL operates at saturation. Calculations made with simulation code FAST [77].

3.1.2 Probability distributions

The next step of our study is the behaviour of the probability distribution of the instantaneous power. In Fig. 11 we show the normalized r.m.s. deviation of the instantaneous radiation power, $\sigma_{\mathrm{w}} = \langle (W - \langle W \rangle)^2 \rangle^{1/2}/\langle W \rangle$, as a function of the undulator length. We see that, at the initial stage of SASE FEL operation, the r.m.s. deviation of the instantaneous power is equal to one for all harmonics. As we already discussed in Section 2, this is a consequence of the start-up from the shot noise in the electron beam. The statistical properties of the undulator radiation and of the radiation from SASE FEL operating in the linear regime are governed by Gaussian statistics [6, 32]. An important feature of the Gaussian statistics is that the normalized r.m.s. deviation of the instantaneous radiation power is equal to the unity. For the fundamental harmonic, the statistics of the radiation are non-Gaussian when the amplification process enters the non-linear mode [6, 32]. For the higher harmonics, non-Gaussian statistics take place when the non-linear harmonic generation starts to dominate over incoherent radiation (at $\hat{z} \gtrsim 8$ in the present numerical example). Analytical theory of non-linear harmonic generation [56] predicts a value of $\sigma_{\mathrm{w}} \simeq 4$ for the third harmonic. Analysis of the relevant curve in Fig. 11 shows that this prediction holds approximately in a short piece of the undulator length only. As we explained, this is because non-linear harmonic generation starts to dominate over incoherent radiation only at the values of the beam bunching at the fundamental harmonic $a_1 \sim 0.1$. However, at such a value of the beam bunching, the modulation of the beam density already deviates from a sinusoidal shape, owing to non-linear effects.

Probability density distributions for the instantaneous power of the fundamental and the third harmonic are presented in Fig. 12. The SASE radiation is a stochastic object and, at a given time, it is impossible to predict the amount of energy that flows to a detector. The initial modulation of the electron beam is defined by the shot noise and has a white spectrum. The high-gain FEL amplifier cuts and amplifies only a narrow frequency band of the initial spectrum $\Delta\omega/\omega \ll 1$. In the time domain, the temporal structure of the fundamental harmonic radiation is chaotic with many random spikes, with a typical duration given by the inverse width of the spectrum envelope. Even without performing numerical simulations, we can describe some general properties of the fundamental harmonic of the radiation from the SASE FEL operating in the linear regime. Indeed, in this case we deal with Gaussian statistics. As a result, the probability distribution of the instantaneous radiation intensity W should be the negative exponential probability density distribution of Eq. (2) [6, 32]. One should remember that the notion of
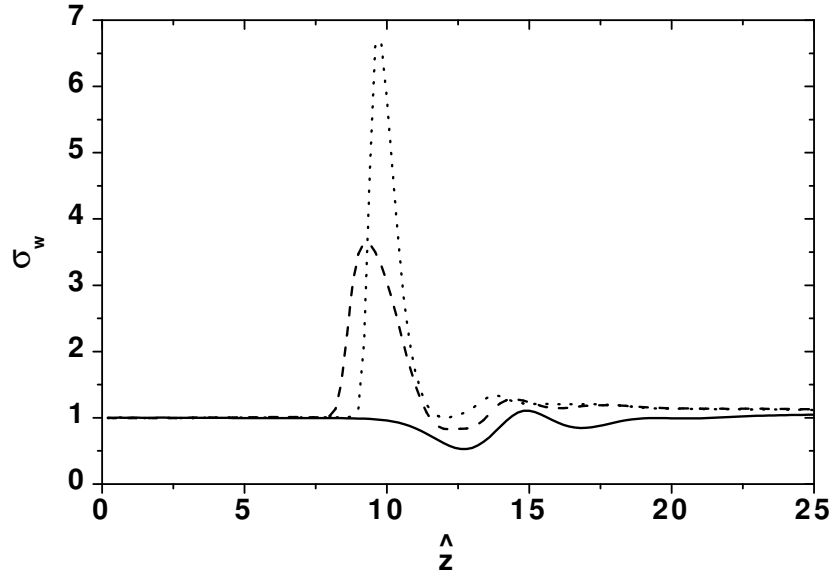
Fig. 11: Normalized r.m.s. deviation of fluctuations of instantaneous radiation power as a function of normalized undulator length. Solid, dashed, and dotted lines correspond to fundamental, third, and fifth harmonics, respectively. Calculations made with simulation code FAST [77].

the instantaneous intensity refers to a certain moment in time, and that the analysis must be performed over an ensemble of pulses. Also, the energy in the radiation pulse E_{rad} should fluctuate in accordance with the gamma distribution of Eq. (3) [6, 32]. These properties are well known in statistical optics as properties of completely chaotic polarized radiation [74].

As discussed in Section 2, the statistics of the high-harmonic radiation from the SASE FEL change significantly with respect to the fundamental harmonic (e.g., with respect to Gaussian statistics), The probability density function of the instantaneous intensity of higher harmonics SASE radiation (Eq. (4)) is a non-linear transformation of Eq. (2). Using this distribution, we obtain the expression for the mean value: $\langle z \rangle = h! \langle W \rangle^h$. Thus, the hth-harmonic radiation for the SASE FEL has an intensity level roughly $h!$ times larger than the corresponding steady-state case, but with more shot-to-shot fluctuations than the fundamental [56]. The non-trivial behaviour of the intensity of the high harmonics reflects the complicated non-linear transformation of the fundamental harmonic statistics. One can see that Gaussian statistics are no longer valid. The upper plots in Fig. 12 give an illustration to these consideration. Although in our practical example we do not have a pure linear amplification regime, the probability density functions for the instantaneous power follow the prediction of Eq. (4) rather well.

Analysis of the probability distributions in Fig. 12 shows that, in the non-linear regime, near the saturation point, the distributions change significantly with respect to the linear regime for both the fundamental and the third harmonic. An important message is that at the saturation point the third harmonic radiation exhibits much more noisy behaviour (nearly negative exponential) while stabilization of the fluctuations of the fundamental harmonics takes place.
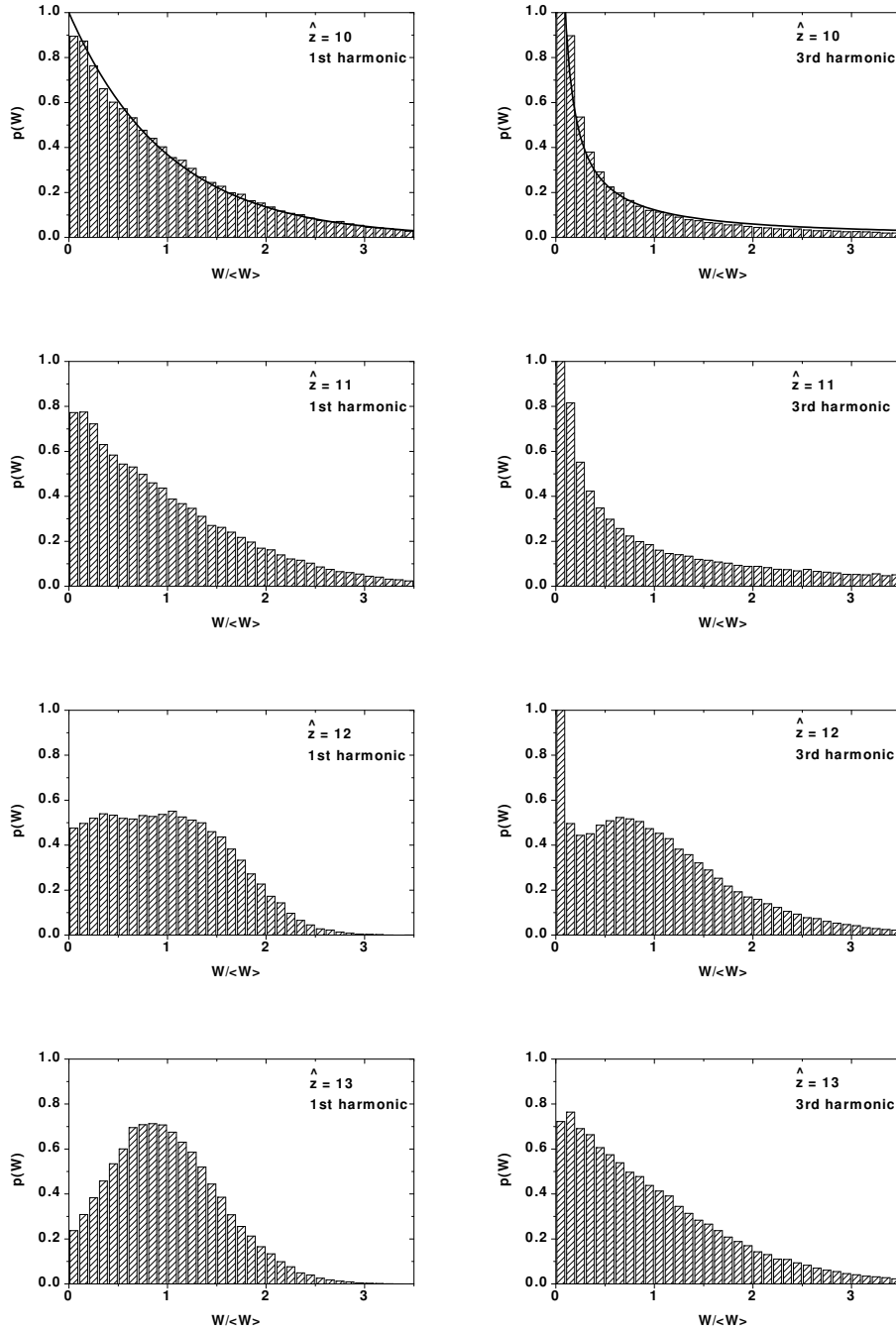
Fig. 12: Probability distribution of instantaneous radiation power at different lengths of the FEL amplifier $\hat{z} = 10$–13. Left and right columns correspond to fundamental and 3rd harmonic, respectively. Solid line shows probability density function (Eq. (4)). Calculations made with simulation code FAST [77].

3.1.3 Correlation functions

The first- and second-order time correlation functions are defined as:

$$g_1(t - t') = \frac{\langle \tilde{E}(t) \tilde{E}^*(t') \rangle}{\left[\langle |\tilde{E}(t)|^2 \rangle \langle |\tilde{E}(t')|^2 \rangle \right]^{1/2}} \;, \qquad g_2(t - t') = \frac{\langle |\tilde{E}(t)|^2 |\tilde{E}(t')|^2 \rangle}{\langle |\tilde{E}(t)|^2 \rangle \langle |\tilde{E}(t')|^2 \rangle} \;. \tag{16}$$

In Fig. 13 we show the evolution of the time correlation functions of the first and second order. At each normalized position along the undulator, $\hat{z}$, they are plotted against the normalized variable $\hat{\tau} = \rho \omega_0 (t - t')$. The upper plot in Fig. 13 corresponds to the linear stage of SASE FEL operation. In the case of the fundamental harmonic, we deal with a Gaussian random process and the relation between the correlation functions holds for $g_2(t - t') = 1 + |g_1(t - t')|^2$. This feature does not hold for higher harmonics. The non-trivial behaviour of the correlation functions reflects the complicated non-linear evolution of the SASE FEL process. The second-order correlation function of the zero argument, $g_2(0)$, takes values smaller or larger than two, but always larger than unity. Note that there is a simple relation between $g_2(0)$ and the normalized r.m.s. power deviation: $g_2(0) = 1 + \sigma_{\mathrm{w}}^2$ (see Fig. 11). It is a well-known result of statistical optics that the cases of $g_2(0) = 1$ and $g_2(0) = 2$ correspond to stabilized single-mode laser radiation and to completely chaotic radiation from a thermal source, respectively. The values of $g_2(0)$ between 1 and 2 belong to some intermediate situation. In classical optics, a radiation source with $g_2(0) < 1$ cannot exist but the case of $g_2(0) > 2$ is possible. As one can see from Fig. 13, the latter phenomenon (known as superbunching) occurs for higher harmonics of SASE FEL, or for the fundamental when the SASE FEL operating in the non-linear regime.

Figure 14 shows the dependence on the undulator length of the normalized coherence time $\hat{\tau}_{\mathrm{c}} = \rho \omega_0 \tau_{\mathrm{c}}$, where τ_{c} is given by Eq. (6). For the fundamental harmonic, the coherence time achieves its maximal value near the saturation point and then decreases drastically. The maximum value of $\hat{\tau}_{\mathrm{c}}$ depends on the saturation length and, therefore, on the value of the parameter N_{c}. With logarithmic accuracy, we have the following expression for the coherence time of the fundamental harmonic:

$$(\hat{\tau}_{\mathrm{c}})_{\mathrm{max}} \simeq \sqrt{\frac{\pi \ln N_{\mathrm{c}}}{18}} \;. \tag{17}$$

Longitudinal coherence for higher harmonics evolves in three different stages. Initially (up to $\hat{z} = 7$–8, see Fig. 14) coherence time increases linearly, as it should, for the spontaneous emission of radiation from the undulator. When the process of non-linear harmonic generation starts to dominate over the spontaneous emission, the coherence time drops sharply. At positions around $\hat{z} = 10$–11, we obtain some plateau where the ratio of the coherence time of the hth harmonic to that of the first harmonic scales as $1/\sqrt{h}$. At these distances, the SASE FEL still operates in the exponential regime when the amplitude of the beam bunching is visibly less than unity, and the intensity of the hth harmonic scales as I_1^h. Such a mechanism of non-linear harmonic generation leads to scaling of the coherence time as $1/\sqrt{h}$. To explain this, we refer to Fig. 6, which presents the temporal structure of the radiation pulse. The radiation pulse consists of a number of spikes (wavepackets). For the sake of simplicity, let us approximate a wavepacket with a Gaussian, $G_1(\hat{s})$, with an r.m.s. width σ_1. Non-linear transformation of the intensity for the hth harmonic gives us envelope $G_h \propto G_1^h$. Therefore, the relevant spike for the hth harmonic is $\sigma_h = \sigma_1/\sqrt{h}$. In other words, sharpening of the peaks in intensity distribution leads to suppression of coherence times for higher harmonics. When the amplification process enters the non-linear stage ($\hat{z} \gtrsim 11$), the relative sharpening of the intensity peaks of higher harmonics becomes stronger, and coherence time starts decrease again. In fact, as one can find from Fig. 13, the coherence time at the saturation point ($\hat{z} = 13$) for higher harmonics approximately decreases inversely proportional to the harmonic number h.
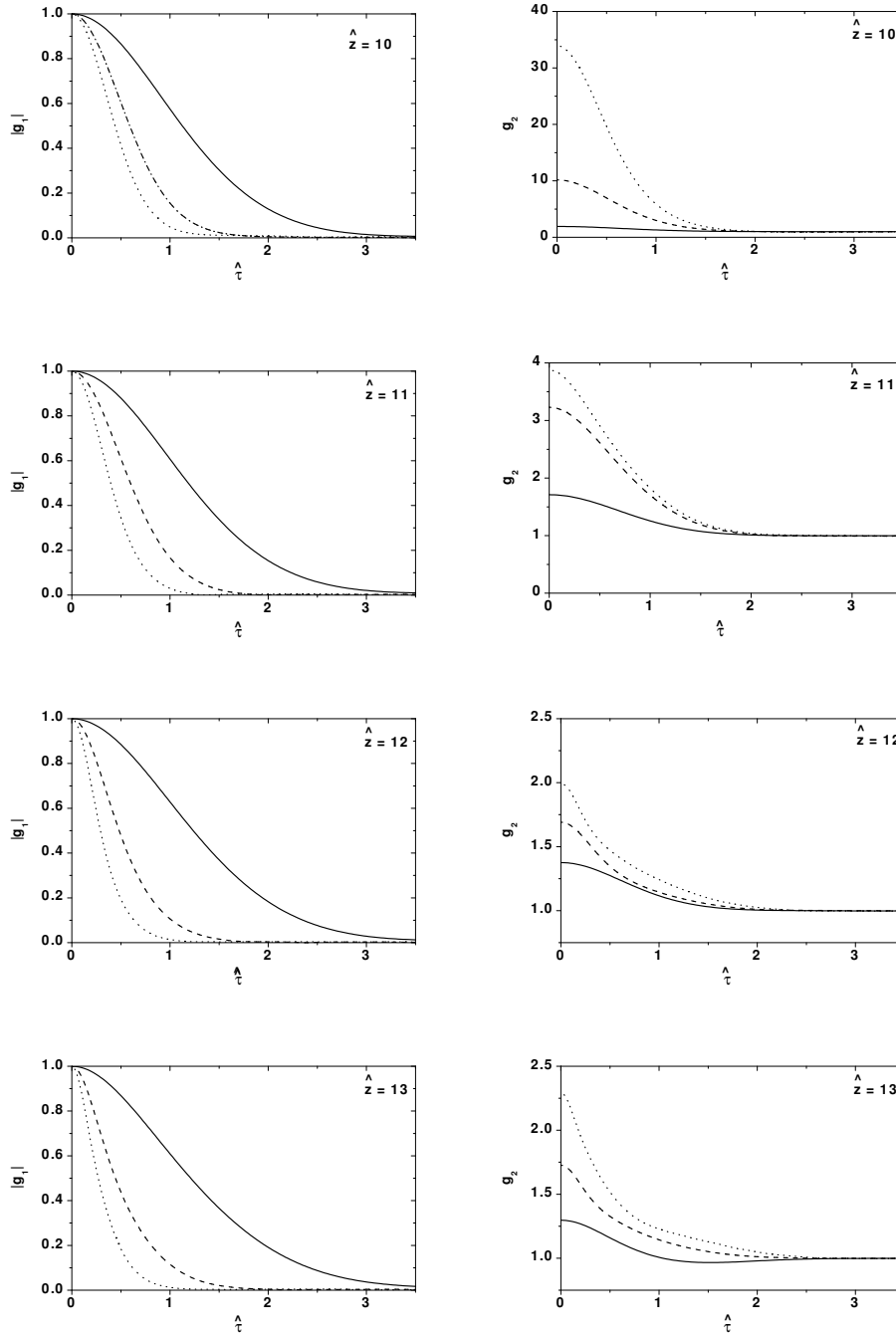
Fig. 13: First-order (left column) and second-order (right column) correlation function at different lengths of the FEL amplifier $\hat{z} = 10$–13. Solid, dashed, and dotted lines correspond to fundamental, third, and fifth harmonics, respectively. Calculations made with simulation code FAST [77].
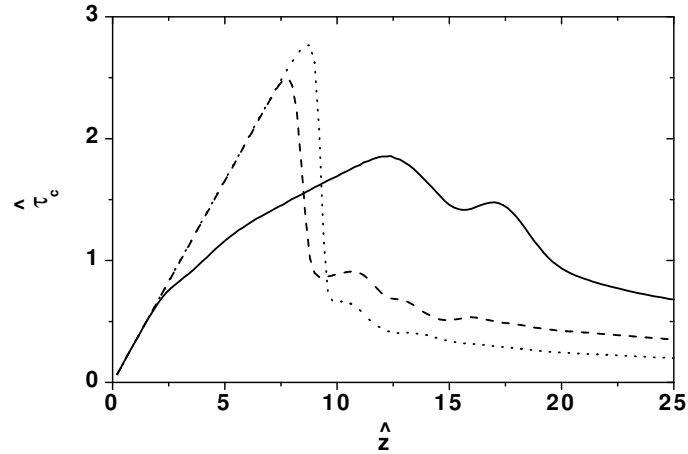
Fig. 14: Normalized coherence time of SASE FEL as a function of normalized undulator length. Solid, dashed, and dotted lines correspond to fundamental, third, and fifth harmonics, respectively

When comparing radiation spectra, it is convenient to use the normalized spectral density, $H(\hat{C})$, defined as

$$\int\limits_{-\infty}^{\infty} d\hat{C} H(\hat{C}) = 1 \, .$$

Here $\hat{C} = [2\pi/\lambda_{\mathrm{w}} - \omega(1 + K^2)/(2c\gamma^2)]/\Gamma$ is the detuning parameter. The frequency deviation, $\Delta\omega$, from the nominal value of ω_h can be recalculated as $\Delta\omega = -2\rho\omega_h\hat{C}$. Since we consider the model of a long rectangular bunch, the function $H(\hat{C})$ can be treated as the normalized spectral density of both the radiation energy and the power.

The spectral density of the radiation energy and the first-order time correlation function form a Fourier transform pair [74]:

$$G(\Delta\omega) = \frac{1}{2\pi} \int\limits_{-\infty}^{\infty} d\tau g_1(\tau) \exp(-\mathrm{i}\Delta\omega\tau) \, . \tag{18}$$

This is the so-called Wiener-Khinchin theorem.

The temporal structures of the radiation pulses (see Fig. 6) are used to calculate the first-order time correlation function (see Fig. 13). Then the radiation spectra are reconstructed by Fourier transformation of the first-order time correlation function. Figure 15 shows the evolution of the radiation spectra of the SASE FEL radiation from the end of the linear regime to saturation. Note that the spectrum width of the higher harmonics from SASE FEL differs significantly from that of incoherent radiation. For the case of incoherent radiation, the relative spectrum width $\Delta\omega/\omega_h$ scales inversely proportional to the harmonic number h [79]. One can see that the situation changes dramatically for the case when the non-linear harmonic generation process starts to dominate. At saturation, we find that the relative spectrum bandwidth is nearly the same for all odd harmonics.

3.2 Short-pulse effects in SASE FEL

Up to now we have studied the properties of the SASE FEL radiation in the framework of a stationary process, i.e. we considered the model of a long electron bunch with a rectangular profile. In this section,
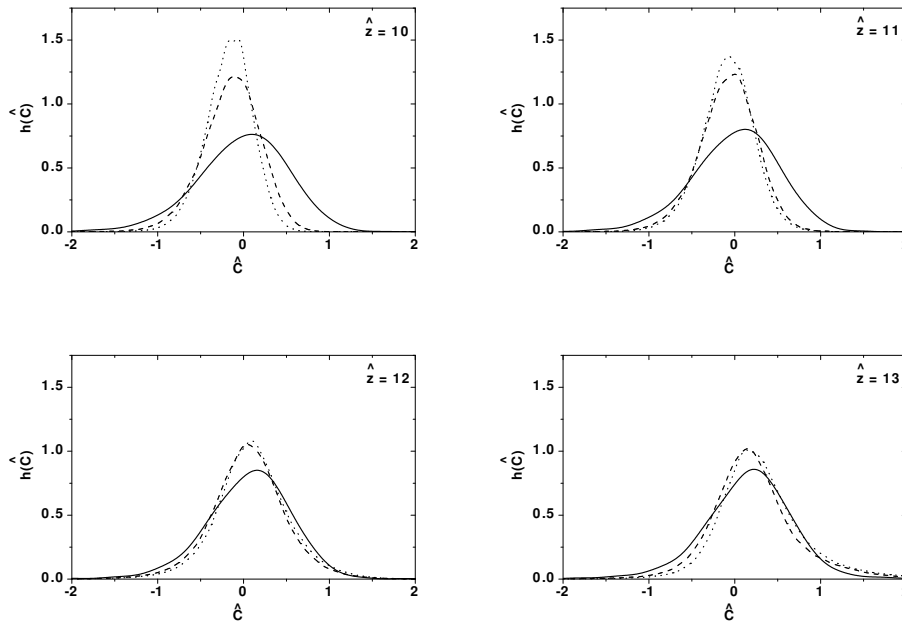
Fig. 15: Normalized spectrum at different lengths of the undulator: $\hat{z} = 10$–13. Solid, dashed, and dotted lines correspond to fundamental, third, and fifth harmonics, respectively. Calculations made with simulation code FAST [77].

we analyse the statistical properties of the radiation from a SASE FEL driven by short electron bunches. In the linear regime, the radiation from a SASE FEL is a Gaussian random process. When approaching saturation point, the statistical properties of the radiation change drastically on a scale of one field gain length. We devote particular attention to the analysis of fluctuations of the total energy in the radiation pulse and after a narrow-band monochromator. We show that slippage effects result in a set of novel features of SASE FEL operating in the non-linear regime. In particular, for very short pulses, we observe the effect of stabilization of fluctuations of energy in the radiation pulse and fluctuations of the energy after the narrow-band monochromator. The suppression factor scales as a square root of the pulse length.

To be specific, we consider an electron beam with a Gaussian axial profile of the current density:

$$S(\hat{s}) = \frac{j(\hat{s})}{j_{\max}} = \exp\left(-\frac{\hat{s}^2}{2\hat{\sigma}_{\mathrm{b}}^2}\right) \, ,$$

where $\hat{\sigma}_{\mathrm{b}} = \rho\omega_0\sigma_{\mathrm{b}}/c$ and σ_{b} is the r.m.s. bunch length. Here and in the following, the normalization is performed with respect to the maximum current density, $j_{\max}$. The r.m.s. bunch length is assumed to be large, $\omega_0\sigma_{\mathrm{b}}/c \gg 1$, or, in normalized form: $\hat{\sigma}_{\mathrm{b}} \gg \rho$. Under this assumption, we can neglect the contribution of the coherent seed to the input signal of the FEL amplifier starting from the shot noise. Since ρ is always much less than unity, we can investigate short-pulse effects, when the bunch is comparable to (or even much shorter than) the typical slippage distance $c/(\rho\omega_0)$.

Even without simulations, we can predict the general properties of the radiation from a SASE FEL operating in the linear regime. Indeed, shot noise in the electron beam is a Gaussian random process [32]. The FEL amplifier, operating in the linear regime, can be considered as a linear filter that does not change statistics. As a result, the radiation is also a Gaussian random process. In this case, the probability distribution of the instantaneous radiation power should be the negative exponential distribution (the notion of instantaneous power refers to a certain moment of time and a certain z coordinate, and that the analysis must be performed over an ensemble of pulses). Also, the finite-time integrals of

the instantaneous power and the integrated spectral density (measured after the monochromator) should fluctuate in accordance with the gamma distribution. Nevertheless, a reasonable question arises as to what are the features of the radiation from SASE FEL operating in the non-linear mode and, in particular, at saturation and post-saturation regime.

In the case of a SASE FEL driven by a short electron bunch, we deal with non-stationary random process, and temporal coherence can be described in terms of an effective correlation function [6]:

$$g_1^{(\text{eff})}(\tau) = \frac{\int\limits_{-\infty}^{\infty} \langle \tilde{E}(\bar{t} + \tau/2)\tilde{E}^*(\bar{t} - \tau/2)\rangle \mathrm{d}\bar{t}}{\int\limits_{-\infty}^{\infty} \langle |\tilde{E}(\bar{t})|^2\rangle \mathrm{d}\bar{t}} \, , \tag{19}$$

where $\bar{t} = (t + t')/2$ and $\tau = t - t'$.

The normalized envelope of the radiation power spectrum and the effective correlation function are connected by a Fourier transform [6]:

$$\frac{\langle |\bar{E}(\Delta\omega)|^2\rangle}{\int\limits_{-\infty}^{\infty} \langle |\bar{E}(\Delta\omega)|^2\rangle \mathrm{d}(\Delta\omega)} = \frac{1}{2\pi}\int\limits_{-\infty}^{\infty} \mathrm{d}\tau g_1^{(\text{eff})}(\tau)\mathrm{e}^{\mathrm{i}\Delta\omega\tau} \, . \tag{20}$$

In other words, the correlation function $g_1^{(\text{eff})}(\tau)$ effectively describes the case of a long rectangular bunch producing the same spectrum as that of a bunch with a gradient profile.

It is natural to define the coherence time for the non-stationary process as

$$\tau_{\text{c}} = \int\limits_{-\infty}^{\infty} \mathrm{d}\tau |g_1^{(\text{eff})}(\tau)|^2 \, . \tag{21}$$

To obtain the output characteristics of the radiation from SASE FEL, one should perform a large number of simulation runs with a time-dependent simulation code. The result of each run contains parameters of the output radiation (field and phase) stored in the boxes over the full length of the radiation pulse. At the next stage of the numerical experiment, the data arrays should be handled to extract information on statistical properties of the radiation. Probability distribution functions of the instantaneous radiation power, of the finite-time integrals of the instantaneous power, and of the radiation energy after the monochromator installed at the exit of the SASE FEL are calculated by plotting histograms of large amounts of statistical data.

3.2.1 *Average energy and fluctuations*

The time structure of a sample radiation pulse and the radiation power averaged over an ensemble are presented in Fig. 16 for different bunch lengths. It can be seen that, for values of $\hat{\sigma}_{\text{b}}$ of about unity, the radiation pulse is visibly shifted from the centre of the electron bunch, owing to the slippage effect. In Fig. 17, the number of modes M is plotted against the longitudinal coordinate for different bunch lengths. The SASE FEL operates in the linear regime, and the number of modes is $M = 1/\sigma_{\mathcal{E}}^2$, where $\sigma_{\mathcal{E}}^2 = \langle(\mathcal{E} - \langle\mathcal{E}\rangle)^2\rangle/\langle\mathcal{E}\rangle^2$ is the relative energy dispersion in the radiation pulse.

Figure 18 shows the evolution of the averaged efficiency along the undulator length. The averaged efficiency is defined as $\langle\hat{\eta}\rangle = \langle E_{\text{rad}}\rangle/(\rho\gamma m_{\text{e}}c^2 N)$, where E_{rad} is energy in the radiation pulse, and N is the number of electrons in the bunch. The dashed line in Fig. 18 represents the averaged efficiency for the case of a long electron bunch with a rectangular profile. The amplification process involves three stages: start-up from shot noise, a stage of exponential gain, and a non-linear stage. Let us define the saturation
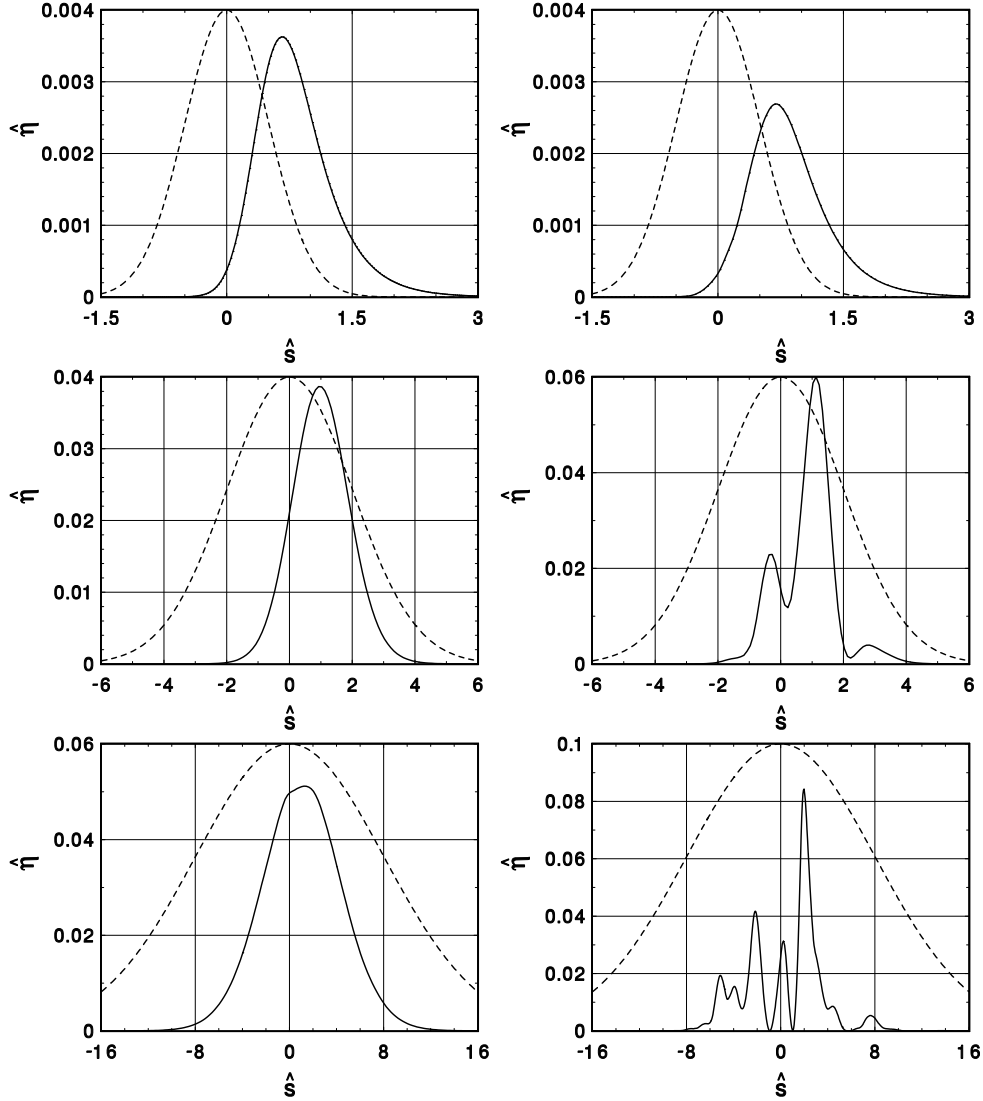
Fig. 16: Averaged (left column) and typical single-shot (right column) axial distribution over $\hat{s} = \rho\omega_0(z/\bar{v}_z - t)$ of normalized radiation power from SASE FEL for different r.m.s. bunch lengths of $\hat{\sigma}_b = 0.5$, 2, and 8 (upper, middle, and lower plots, respectively). Dashed lines represent axial profile of the beam current. The normalized length of the undulator is $\hat{z} = 10$. Calculations made with simulation code FAST [77].

point as the first maximum of the gain curve. At $\hat{\sigma}_b \lesssim 2$, the saturation length increases as $\hat{z}_{sat} \propto 1/\sqrt{\hat{\sigma}_b}$, and the averaged saturation efficiency decreases as $\langle\hat{\eta}\rangle \propto \sqrt{\hat{\sigma}_b}$. These features of short bunch effects were addressed in an earlier paper [29]. Figure 19 shows the dependence of the saturation efficiency on the bunch length. It can be seen that the saturation efficiency quickly approaches an asymptotical value. A comparison with the case of a long electron pulse with a rectangular profile (the dashed line in the plot) shows that only 60% of electrons produce radiation. This is a consequence of the gradient profile of the electron bunch.

Figure 20 (left plot) shows the evolution along the undulator of the radiation pulse energy, fluctuations of the radiation pulse energy, and the r.m.s. photon pulse length. A maximum of the fluctuations of the radiation pulse energy and a minimum radiation pulse duration are obtained at the end of the exponential gain regime. Normalized values of these parameters (E/E_{sat}, σ_E/σ_E^{max}, and $\sigma_{ph}/\sigma_{ph}^{min}$) exhibit nearly universal dependencies for the r.m.s. electron pulse duration $\rho\omega\sigma_z \gtrsim 1$, as shown in the right plot in Fig. 20. This allows us to derive the universal dependency of the r.m.s. electron pulse length
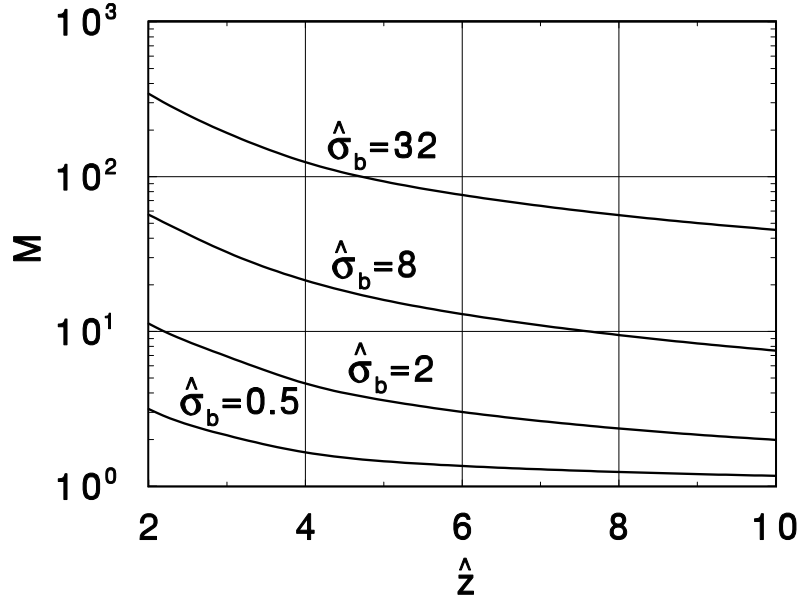
Fig. 17: Number of modes in the radiation pulse for Gaussian electron bunches of different lengths versus undulator length: SASE FEL operates in linear regime. Calculations were made with simulation code FAST [77].
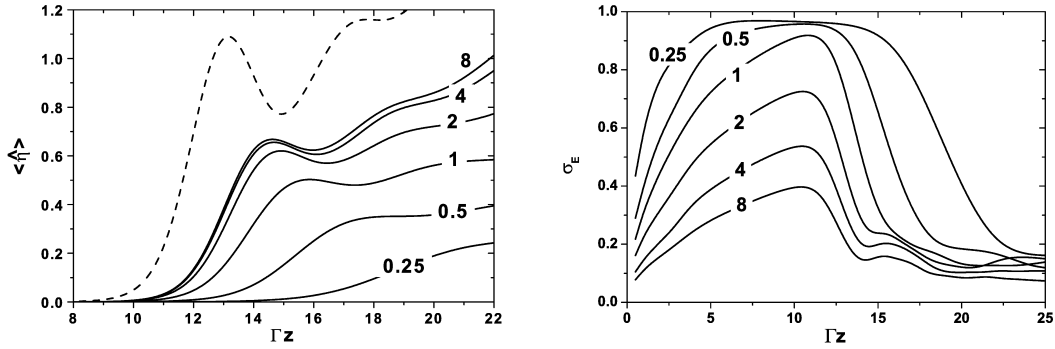

Fig. 18: Left: Averaged efficiency of SASE FEL versus undulator length $\hat{z} = \Gamma z$ for different lengths of electron bunch $\hat{\sigma}_{\mathrm{b}} = 0.25$-8. Right: normalized r.m.s. deviation of energy in radiation pulse; $N_{\mathrm{c}} = 10^8$. Dashed line represents case of long electron pulse with rectangular profile. Calculations made with simulation code FAST [77].

and the minimum FWHM radiation pulse length $\tau_{\mathrm{ph}}^{\mathrm{min}} = \sqrt{2\pi}\sigma_{\mathrm{ph}}^{\mathrm{min}}$ at the end of the linear regime as a function of the number of modes in the radiation pulse (see Fig. 21). For $M \gtrsim 2$ we have, with reasonable practical accuracy:

$$\sigma_z \simeq \tau_{\mathrm{ph}}^{\mathrm{min}} \simeq \frac{M\lambda}{5\rho} \simeq \frac{M\lambda L_{\mathrm{sat}}}{5c\lambda_{\mathrm{w}}} \ . \tag{22}$$

The minimum radiation pulse duration expressed in terms of the coherence time is $\tau_{\mathrm{ph}}^{\mathrm{min}} \simeq 0.7 \times M \times \tau_{\mathrm{c}}$.

Lengthening of the radiation pulse occurs when the amplification process enters the saturation regime. This happens because of two effects. The first effect is lasing to saturation of the tails of the electron bunch, and the second effect is pulse lengthening due to slippage effects (just simply one radiation wavelength per one undulator period). The effect of lasing tails gives the same relative radiation pulse lengthening as is illustrated in the bottom plot in Fig. 20. At the saturation point, pulse lengthening is about a factor of 1.4 with respect to the minimum pulse for the linear regime given by Eq. (22), and is increased up to a factor of two in the deep non-linear regime. It can also be seen that the slippage effect is more pronounced for relative lengthening of short pulses.
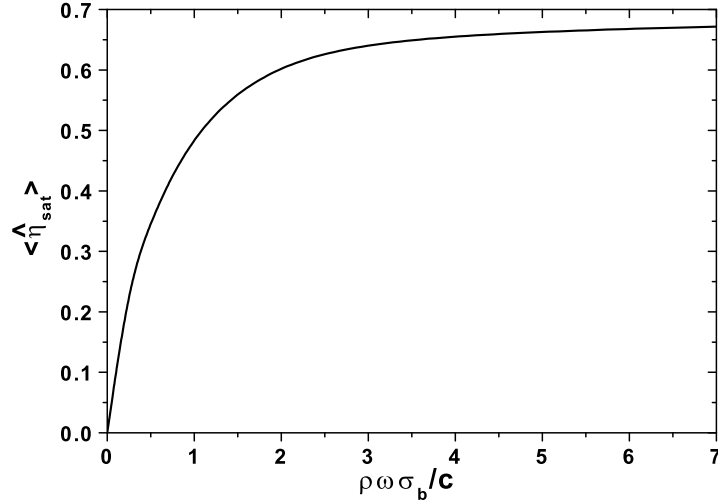
Fig. 19: Averaged efficiency of SASE FEL at saturation versus length of electron bunch. Calculations made with simulation code FAST [77].
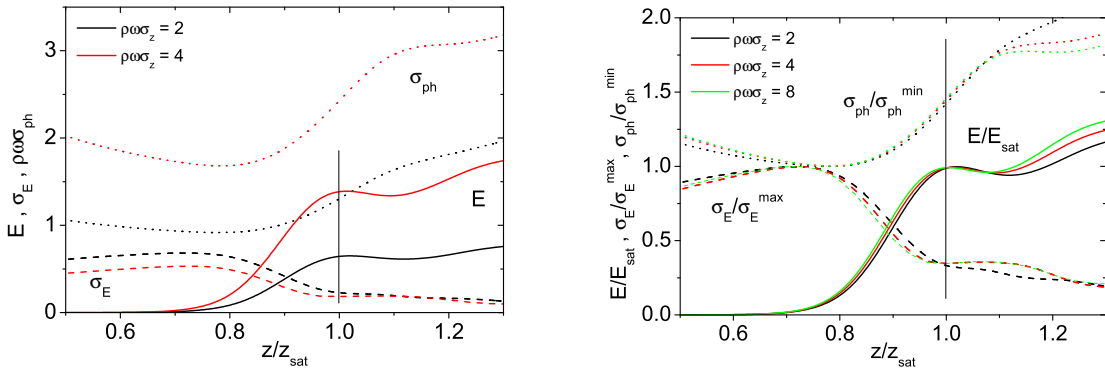

Fig. 20: Evolution of the energy in the radiation pulse E (solid line), fluctuations of the radiation energy σ_{E} (dashed line), and r.m.s. radiation pulse duration $\rho\omega\sigma_{\mathrm{ph}}$ (dotted line) versus undulator length. Black, red, and green lines correspond to electron r.m.s. pulse durations $\rho\omega\sigma_{\mathrm{z}}$ of 2, 4, and 8, respectively. Values on the right plot are normalized as E/E_{sat}, $\sigma_{\mathrm{E}}/\sigma_{\mathrm{E}}^{\mathrm{max}}$, and $\sigma_{\mathrm{ph}}/\sigma_{\mathrm{ph}}^{\mathrm{min}}$.

3.2.2 *Correlation functions and coherence time*

The effective correlation function is calculated as follows. We perform a large number of simulation runs, calculate the spectrum of each pulse, and calculate the envelope of the normalized averaged spectrum. Equation (20) is used to calculate the first-order correlation function. The plot of the effective correlation function $g_1(\tau)$ at saturation is shown in Fig. 22. The circles in this plot represent the correlation function for the case of a long electron pulse with a rectangular profile [32]. Figure 23 shows plots for the coherence time $\hat{\tau}_{\mathrm{c}}$ (Eq. (21)) for different electron pulse lengths. Analysis of these results allows us to state that for the bunch length $\hat{\sigma}_{\mathrm{b}} \gtrsim 4$ we have good agreement between the case of finite pulse duration and asymptotic results for a long pulse with a rectangular profile. Conversely, at short bunch length, $\hat{\sigma}_{\mathrm{b}} \lesssim 2$, the behaviour of the coherence time differs visibly from an asymptotic one. This is a clear indication of a different physical process.
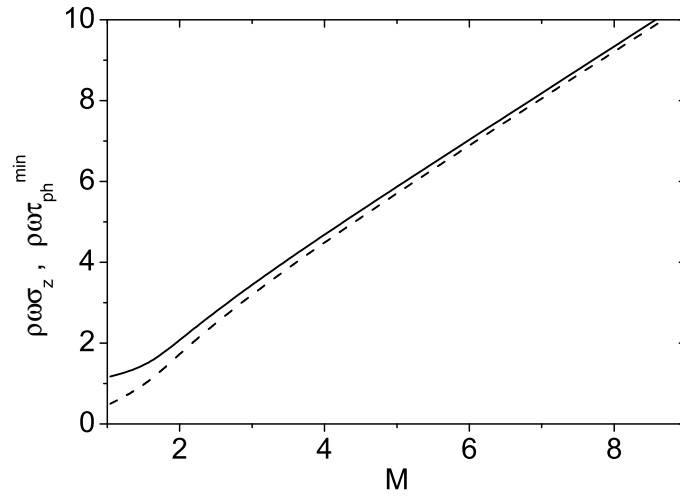
Fig. 21: The r.m.s. electron pulse duration σ_z (dashed curve) and minimum FWHM photon pulse duration τ_{ph}^{min} at the end of the linear regime (solid curve) versus the number of modes in the radiation pulse M.
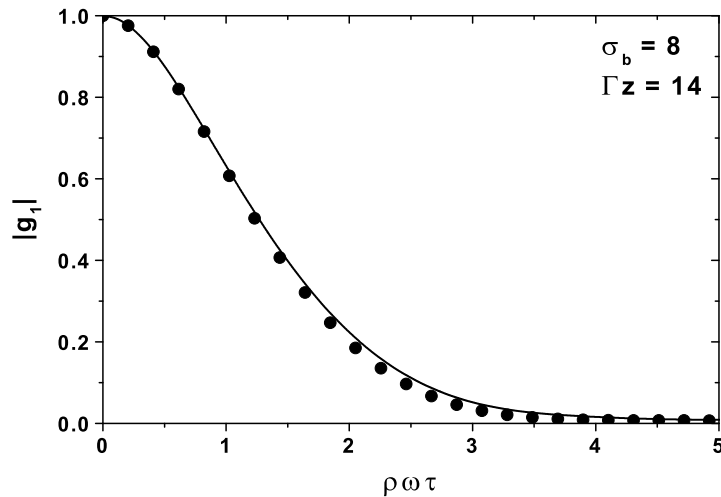

Fig. 22: Module of first-order time correlation function, where $\hat{\sigma}_b = 8$ and $N_c = 10^8$; SASE FEL operates at saturation, $\hat{z} = 14$. Circles correspond to the case of a long electron bunch with a rectangular profile. Calculations made with simulation code FAST [77].

3.2.3 Fluctuations of energy in the radiation pulse

The right plot in Fig. 18 shows the normalized r.m.s. deviation of energy in the radiation pulse. There is a straightforward explanation for the behaviour of the fluctuations in the linear regime: the number of longitudinal modes decreases with the pulse length and the undulator length. The radiation of the SASE FEL operating in the linear regime is a Gaussian random process, so the probability distribution of the energy in the radiation pulse is a gamma distribution. The situation changes drastically when the amplification process enters a non-linear stage. It is seen that deviation of energy drops quickly on a scale of a field gain length. For a long pulse, fluctuations are suppressed as $1/\sqrt{\hat{\sigma}_b}$, which is a consequence of increasing the number of statistically independent spikes in the radiation pulse [29]. The physical
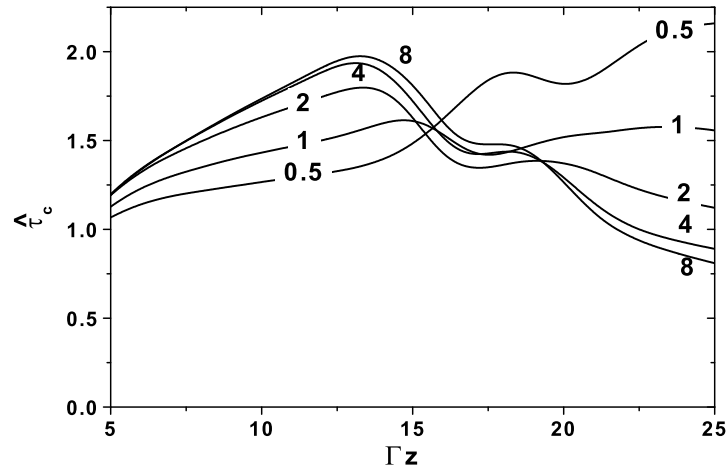
Fig. 23: Normalized coherence time $\hat{\tau}_c$ versus undulator length. Electron bunch length varies within the limits $\hat{\sigma}_b = 0.5\text{--}8$; $N_c = 10^8$. Calculations made with simulation code FAST [77].
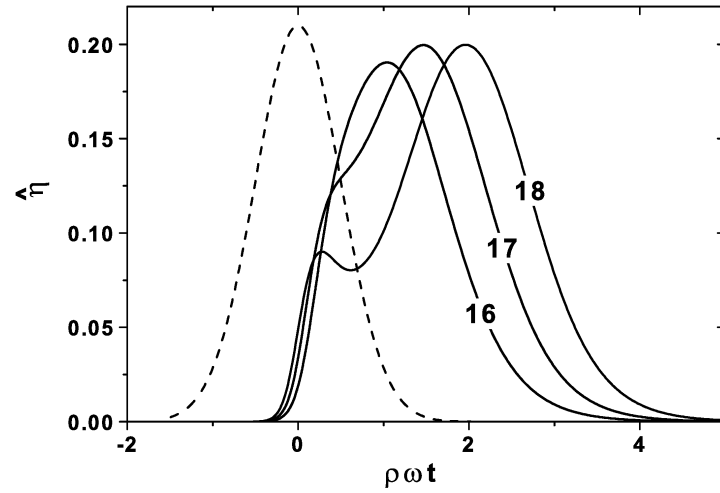

Fig. 24: Averaged normalized radiation power versus time; SASE FEL operates in the non-linear regime. Undulator lengths are $\hat{z} = 16$, 17, and 18. Dashed line represents electron bunch profile ($\hat{\sigma}_b = 0.5$). Calculations made with simulation code FAST [77].

picture becomes quite different for the bunch length $\hat{\sigma}_b \lesssim 2$: the deviation of energy in the radiation pulse starts to decrease with the bunch length as $\sqrt{\hat{\sigma}_b}$. The nature of this phenomenon can be understood by analysing the structure of the radiation pulse (see Fig. 24). At the end of the linear mode of operation, a SASE FEL driven by a short electron bunch produces radiation pulses of nearly the same shape, but with amplitudes fluctuating by almost negative exponential distribution. When the amplification process enters the non-linear stage, the radiation power is saturated, and pulses sleep forward. A further increase in the total energy occurs, due to the radiation of bunched electron beam. Since maximal bunching of the electron beam is limited to unity, this additional radiation is well stabilized, leading to overall stability of the total energy in the radiation pulse.

Simulations show that the statistics of the radiation also change drastically near the saturation point, on a scale of one field gain length. Figure 25 shows the evolution of the probability density
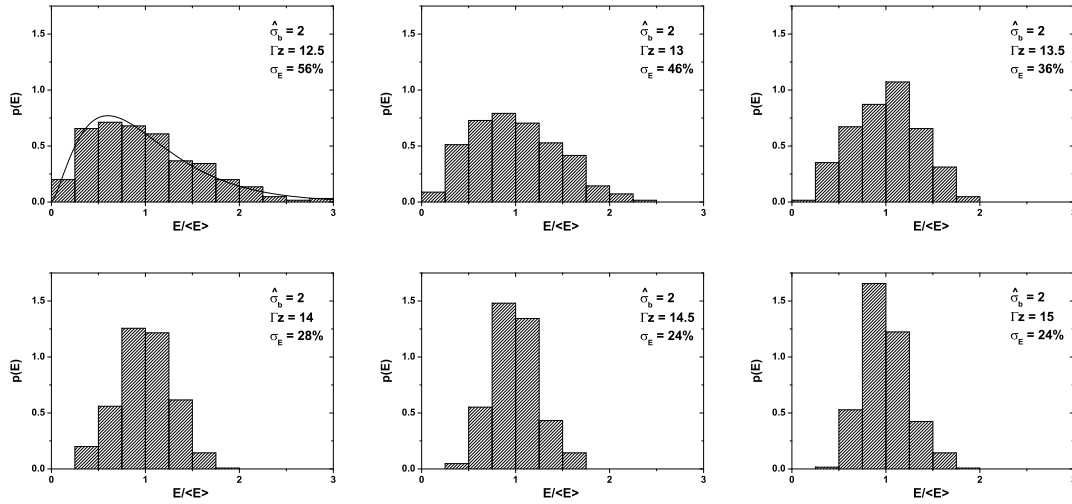
Fig. 25: Probability density distribution of energy in radiation pulse for different undulator lengths; electron pulse length, $\hat{\sigma}_b = 2$. Solid curve represents gamma distribution. Calculations made with simulation code FAST [77].

distribution of energy in the radiation pulse for different lengths of the undulator. The electron pulse length is $\hat{\sigma}_b = 2$. The solid curve represents a gamma distribution. Such behaviour is also typical for shorter bunch lengths.

3.2.4 *Fluctuations of energy after narrow-band monochromator*

Let us study the statistics of SASE FEL radiation filtered through a narrow-band monochromator. Plots of the normalized r.m.s. deviation of energy after a narrow-band monochromator versus undulator length are presented in Fig. 26. In the linear stage of SASE FEL operation, the value of normalized energy deviation is equal to unity, and energy fluctuates in accordance with a negative exponential distribution. This is a consequence of the fact that, in this case, radiation is a Gaussian random process. However, in the non-linear mode of operation, we obtain a significant decrease in fluctuations when the pulse length decreases (see Fig. 27). This effect has a simple physical explanation. When a SASE FEL driven by a short bunch operates in the linear regime, radiation pulses have a similar shape each time, but the amplitude fluctuates by an almost negative exponential distribution (see left plot in Fig. 16). When the amplification process enters the non-linear stage, amplitudes of different pulses are equalized, owing to saturation effects, while keeping the close shape (see right plot in Fig. 28). The spectrum of the radiation pulse is given by the Fourier transform of the radiation field, and at saturation we obtain a nearly similar spectrum envelope for different pulses (see right plot in Fig. 29). As a result, we can expect that fluctuations of the radiation energy after a narrow-band monochromator should follow fluctuations of the total energy in the radiation pulse. Figure 30 confirms this simple physical consideration. At saturation, fluctuations of the energy after the narrow-band monochromator decrease as $\sigma_M \simeq \sigma_E \propto \sqrt{\hat{\sigma}_b}$.

Study of the amplification process in the SASE FEL driven by an electron bunch of finite pulse duration allows us to make the following conclusions. For the bunch length $\hat{\sigma}_b \gtrsim 4$, asymptotical results [32] for a long rectangular bunch are applicable. At $\hat{\sigma}_b \lesssim 2$, the SASE FEL exhibits quite different behaviour, caused by the strong influence of slippage effects. In addition to a reduction in the FEL gain and efficiency [29], short-pulse effects strongly influence the statistical properties of the radiation in the non-linear regime. In particular, for very short pulses, we found the effect of stabilization of fluctuations of energy in the radiation pulse and fluctuations of the energy after the narrow-band monochromator. The suppression factor scales as $\sqrt{\hat{\sigma}_b}$ with electron bunch length. This effect has been measured experimentally at the TTF FEL [46].
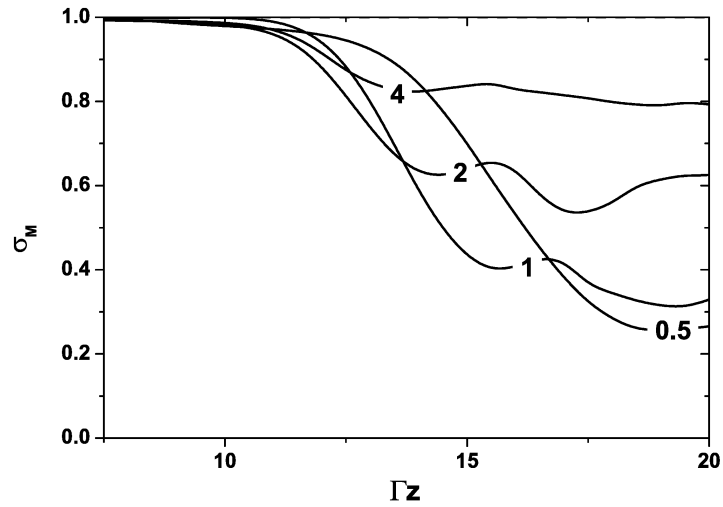
Fig. 26: Normalized r.m.s. deviation of energy after narrow-band monochromator versus undulator length. Electron bunch length changes within the limits $\hat{\sigma}_{\mathrm{b}} = 0.5\text{--}4$. $N_{\mathrm{c}} = 10^8$. Calculations made with simulation code FAST [77].
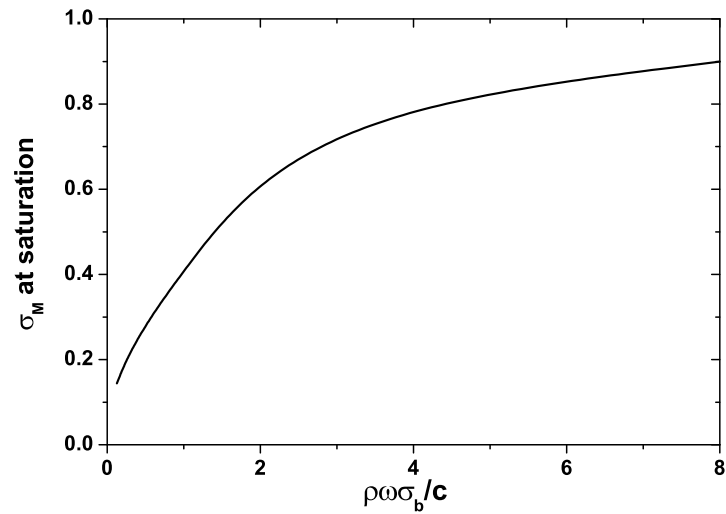

Fig. 27: Normalized r.m.s. deviation of energy after narrow-band monochromator versus length of electron bunch; SASE FEL operates at saturation. Calculations made with simulation code FAST [77].

4 Transverse coherence

At the initial stage of amplification, the spatial coherence is poor, and the radiation consists of a large number of transverse modes. Longitudinal coherence is poor as well. In the exponential stage of amplification, transverse modes with higher gain dominate over modes with lower gain as the undulator length progresses. This feature is also known as the mode competition process. Longitudinal coherence is also improving in the high-gain linear regime. The mode selection process stops at the onset of the non-linear regime, and maximum values of the degree of the transverse coherence and of the coherence time are reached at this point. The undulator length to saturation is in the range of about nine (hard X-ray SASE FELs) to eleven (visible-range SASE FELs) field gain lengths [41]. The situation with
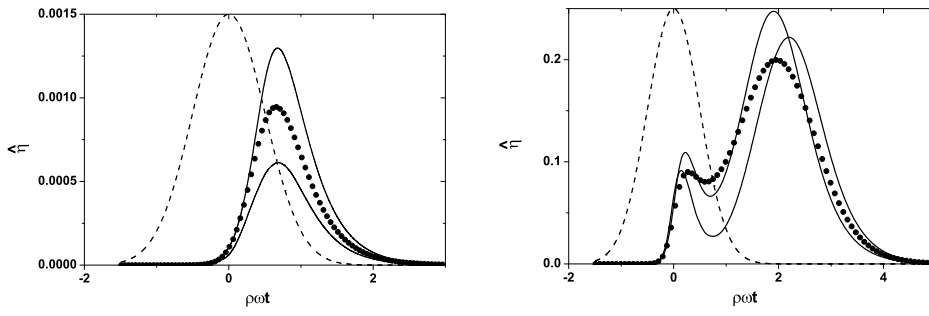
Fig. 28: Normalized power of SASE FEL radiation in (left) the linear regime and (right) at saturation. Solid curves are single pulses, and circles represent averaging over many pulses; dashed curve is electron bunch profile, $\hat{\sigma}_{\mathrm{b}} = 0.5$. Calculations made with simulation code FAST [77].
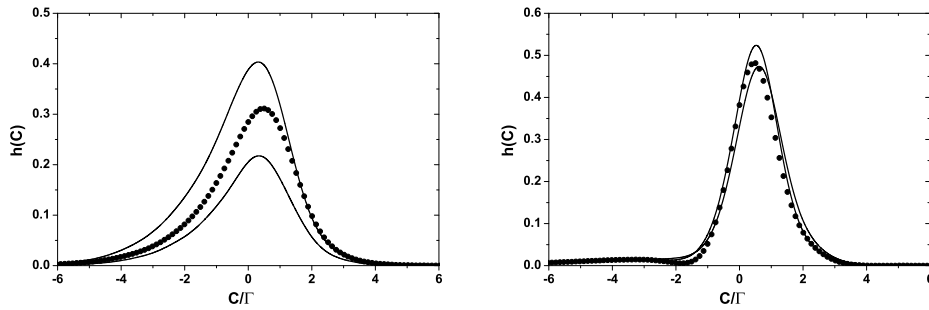

Fig. 29: Spectrum of SASE FEL radiation in (left) the linear regime and (right) at saturation. Solid curves are single pulses (see Fig. 16); circles represent averaging over many pulses. Electron bunch length, $\hat{\sigma}_{\mathrm{b}} = 0.5$. Calculations made with simulation code FAST [77].
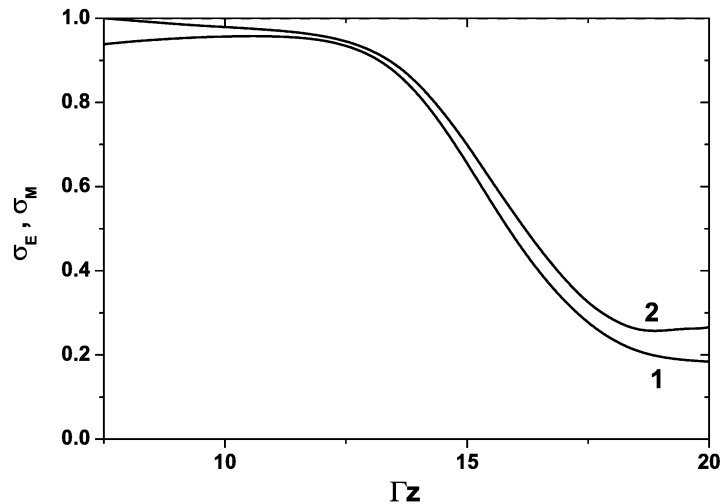

Fig. 30: Normalized r.m.s. deviation of (1) total energy in the radiation pulse and (2) energy after narrow-band monochromator versus undulator length. Length of electron bunch, $\hat{\sigma}_{\mathrm{b}} = 0.5$. Calculations made with simulation code FAST [77].

transverse coherence is favourable when the relative separation of the field gain between the fundamental and higher modes exceeds 25–30%. In this case, the maximum degree of transverse coherence can exceed 90% [39, 41]. Further development of the amplification process in the non-linear stage leads to visible degradation of the coherence properties.

Separation of the gain of the FEL radiation modes mainly depends on the value of the diffraction parameter. An increase in the value of the diffraction parameter results in less relative separation of the gain of the modes. In this case, we deal with the mode degeneration [6, 68]. Since the number of gain lengths to saturation is limited, the contribution of the higher spatial modes to the total power increases with the value of the diffraction parameter, and the transverse coherence degrades. The range of large diffraction parameter values is typical for SASE FELs operating in the hard X-ray wavelength range. It is also worth noticing that a spread of longitudinal velocities (due to energy spread and emittance) helps to suppress high-order modes, thus improving transverse coherence properties. This consideration suggests that a tight focusing of the electron beam in the undulator can be important for reaching a good coherence, owing to a reduction of the diffraction parameter and an increase of the velocity spread.

In this section, we present a thorough analysis of the coherence properties of the radiation from a SASE FEL. The analysis is performed in the framework of three-dimensional theory. We find that there is such a parameter range where the degree of transverse coherence of the radiation from SASE FEL is visibly less than unity. We also show that the pointing stability of the SASE FEL beam suffers from insufficient mode selection of higher spatial radiation modes, which happens for large values of the diffraction parameter.

4.1 FEL radiation modes

We consider an axisymmetrical model of the electron beam. It is assumed that the transverse distribution function of the electron beam is Gaussian, so that the r.m.s. transverse size of the matched beam is $\sigma = \sqrt{\epsilon\beta}$, where ϵ is the r.m.s. beam emittance and β is the beta function. In the framework of the three-dimensional theory, the operation of a short-wavelength FEL amplifier is described by the following parameters: the diffraction parameter B, the energy spread parameter $\hat{\Lambda}_{\mathrm{T}}^2$, the betatron motion parameter $\hat{k}_\beta$, and the detuning parameter $\hat{C}$ [6, 70]:

$$B = 2\bar{\Gamma}\sigma^2\omega/c\,, \qquad\qquad \hat{C} = C/\bar{\Gamma}\,,$$
$$\hat{k}_\beta = 1/(\beta\bar{\Gamma})\,, \qquad\qquad \hat{\Lambda}_{\mathrm{T}}^2 = (\sigma_{\mathrm{E}}/E)^2/\bar{\rho}^2\,, \qquad (23)$$

The gain parameter $\bar{\Gamma}$ and efficiency parameter $\bar{\rho}$ are given by:

$$\bar{\Gamma} = \left[\frac{I}{I_{\mathrm{A}}}\frac{8\pi^2 K^2 A_{\mathrm{JJ}}^2}{\lambda\lambda_{\mathrm{w}}\gamma^3}\right]^{1/2}\,, \qquad \bar{\rho} = \frac{\lambda_{\mathrm{w}}\bar{\Gamma}}{4\pi}\,. \qquad (24)$$

Here, $E = \gamma mc^2$ is the energy of electron, γ is a relativistic factor, and $C = 2\pi/\lambda_{\mathrm{w}} - \omega/(2c\gamma_z^2)$ is the detuning of the electron with nominal energy $\mathcal{E}_0$. Note that the efficiency parameter $\bar{\rho}$ entering the equations of the three-dimensional theory relates to the one-dimensional parameter ρ as $\rho = \bar{\rho}/B^{1/3}$ [4, 6]. The following notation is used here: I is the beam current, $\omega = 2\pi c/\lambda$ is the frequency of the electromagnetic wave, λ_{w} is undulator period, K is the r.m.s. undulator parameter, $\gamma_z^{-2} = \gamma^{-2} + \theta_s^2$, $I_{\mathrm{A}} = mc^3/e = 17$ kA is the Alfven current, $A_{\mathrm{JJ}} = 1$ for a helical undulator and $A_{\mathrm{JJ}} = J_0(K^2/2(1 + K^2)) - J_1(K^2/2(1 + K^2))$ for a planar undulator. J_0 and J_1 are the Bessel functions of the first kind. The energy spread is assumed to be Gaussian with r.m.s. deviation σ_{E}.

The amplification process in a SASE FEL starts from the shot noise in the electron beam. At the initial stage of amplification, the coherence properties are poor, and the radiation consists of a large number of transverse and longitudinal modes [6, 39, 67–73]:

$$\tilde{E} = \sum_{m,n}\int \mathrm{d}\omega A_{mn}(\omega, z)\Phi_{mn}(r, \omega)\exp[\Lambda_{mn}(\omega)z + \mathrm{i}m\phi + \mathrm{i}\omega(z/c - t)]\,. \qquad (25)$$
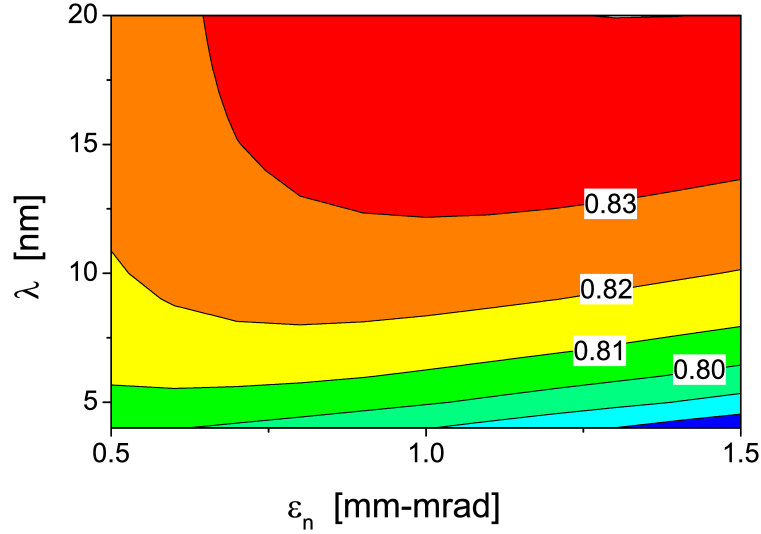
Fig. 31: Contour plot of ratio of maximum field gain of TEM_{10} to field gain of the ground TEM_{00} mode versus radiation wavelength and emittance: beam current, 1.5 kA; beta function, 10 m. Calculations made with simulation code FAST [77].

Each mode is characterized by the eigenvalue $\Lambda_{mn}(\omega)$ and the field distribution eigenfunction $\Phi_{mn}(r, \omega)$. The real part of the eigenvalue $\mathrm{Re}(\Lambda_{mn}(\omega))$ is referred to as the field gain. The field gain length is $L_g = 1/\mathrm{Re}(\Lambda_{mn}(\omega))$. Eigenvalues and eigenfunctions are the solutions of the eigenvalue equation [69, 70]. Each eigenvalue has a maximum at a certain frequency (or, at a certain detuning), so that the detuning for each mode is chosen automatically in the case of a SASE FEL (in contrast with seeded FELs, where the detuning can be set to any value). Thus, we will in fact deal with the three dimensionless parameters: B, $\hat{k}_\beta$, and $\hat{\Lambda}_{\mathrm{T}}^2$.

Let us look closer at the properties of the radiation modes. The gains for several modes are depicted in Fig. 31 as functions of the diffraction parameter. The values for the gain correspond to the maximum of the scan over the detuning parameter $\hat{C}$. The curve for the TEM_{00} mode shows the values of normalized gain $\mathrm{Re}(\Lambda_{00}/\bar{\Gamma})$. Curves for the higher spatial modes show the ratio of the gain of the mode to the gain of the fundamental mode, $\mathrm{Re}(\Lambda_{mn}/\Lambda_{00})$. Sorting of the modes by the gain results in the following ranking: TEM_{00}, TEM_{10}, TEM_{01}, TEM_{20}, TEM_{11}, TEM_{02}. The gain of the fundamental TEM_{00} mode is always above the gain of higher-order spatial modes. The difference in the gain between the fundamental TEM_{00} mode and higher-order spatial modes is pronounced for small values of the diffraction parameter $B \lesssim 1$. The gain of higher-order spatial modes approaches, asymptotically, the gain of the fundamental mode for large values of the diffraction parameter. In other words, the effect of mode degeneration takes place. Its origin can be understood through a qualitative analysis of the eigenfunctions (distribution of the radiation field in the near zone). Figure 32 shows eigenfunctions of the FEL radiation modes for two values of the diffraction parameter, $B = 1$ and $B = 10$. We observe that, for small values of the diffraction parameter, the field of the higher spatial modes spans far away from the core of the electron beam, while the fundamental TEM_{00} mode is more confined. This feature provides a higher coupling factor of the radiation with the electron beam and higher gain. For large values of the diffraction parameter, all radiation modes shrink to the beam axis, which results in equalization of coupling factors and of the gain. Asymptotically, the eigenvalues of all modes tends to the one-dimensional asymptote as [43]:

$$\Lambda_{mn}/\bar{\Gamma} \simeq \frac{\sqrt{3}+\mathrm{i}}{2B^{1/3}} - \frac{(1+\mathrm{i}\sqrt{3})(1+n+2m)}{3\sqrt{2}B^{2/3}} \,. \tag{26}$$

For a SASE FEL, the undulator length to saturation is in the range from about nine (hard X-ray range) to eleven (visible range) field gain lengths [41, 42, 65]. The mode selection process stops
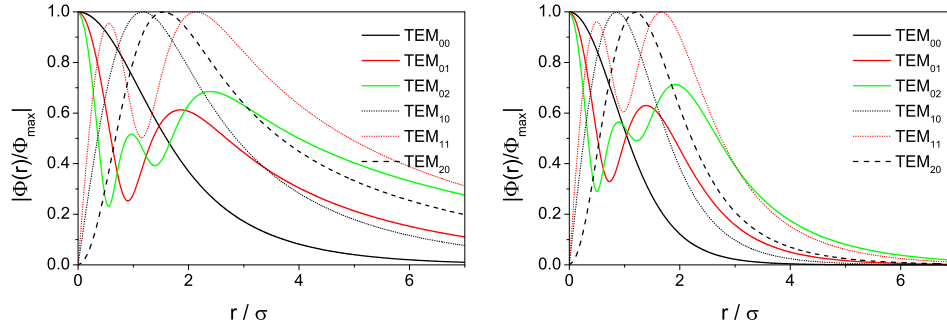
Fig. 32: Amplitude of the eigenfunctions of the FEL radiation modes, $|\Phi_{mn}(r)|/|\Phi_{\max}|$. Left: diffraction parameter $B = 1$. Right: $B = 10$. Detuning corresponds to the maximum of the gain. Energy spread parameter, $\hat{\Lambda}_T^2 \to 0$; betatron motion parameter, $\hat{k}_\beta \to 0$. Colour codes refer to the radial index of the mode: 0, black; 1, red; 2, green. Line type codes refer to the azimuthal index of the mode: 0, solid line; 1, dotted line; 2, dashed line. Calculations made with simulation code FAST [77].

at the onset of the non-linear regime, about two field gain lengths before saturation. Let us make a simple estimate of the value of the diffraction parameter $B = 10$ and the cold electron beam, $\hat{\Lambda}_T^2 \to 0$, and $\hat{k}_\beta \to 0$. We get from Fig. 31 that the ratio of the gain $\mathrm{Re}(\Lambda_{10}/\Lambda_{00})$ is equal to 0.87. With an assumption of similar values of coupling factors, we find that the ratio of the field amplitudes at the onset of the non-linear regime is about of factor of three only. An estimate of the contribution of the higher spatial modes to the total power is about 10%. Another numerical example for $B = 1$ gives the ratio $\mathrm{Re}(\Lambda_{10}/\Lambda_{00}) = 0.73$, and the ratio of field amplitudes exceeds a factor of 10. Thus, an excellent transverse coherence of the radiation is not expected for a SASE FEL with a diffraction parameter $B \gtrsim 10$ and a small velocity spread in the electron beam.

A longitudinal velocity spread due to the energy spread and emittance serves as a tool for selective suppression of the gain of the higher spatial modes [6,68]. Figures 33 and 34 show the dependence of the gain of TEM_{00} and TEM_{10} modes on the betatron motion parameter and the energy spread parameter. We see that with the fixed value of the diffraction parameter, the mode degeneration effect can be relaxed at the price of gain reduction.

The betatron motion can influence the gain of different modes (and, therefore, transverse coherence properties) via two different mechanisms. First, the particles move across the beam, thus transferring the information between different points in the beam cross-section. Second, as already mentioned, there is a spread of longitudinal velocities that has a similar effect as the energy spread (and is usually more important than the first one). One can introduce a combination of parameters B and $\hat{k}_\beta$ that can, to some extent, be similar to the energy spread parameter:

$$(\hat{\Lambda}_T^2)_{\mathrm{eff}} = B^2 \hat{k}_\beta^4 \tag{27}$$

Finally, let us note that the situation with transverse coherence is favourable when relative separation of the gain between the fundamental and higher spatial modes is more than 25–30%. In this case, the degree of transverse coherence can reach values above 90% at the end of the high-gain linear regime [39, 43]. Further development of the amplification process in the non-linear stage leads to a significant degradation of the spatial and temporal coherence [41, 42, 65].

4.2 Coherence properties of the radiation from the FLASH free electron laser

In the current experimental situation, many parameters of the electron beam at FLASH depend on practical tuning of the machine. Analysis of measurements and numerical simulations shows that, depending on the tuning of the machine, emittance may change from about 1 to about 1.5 mm-mrad. Tuning at
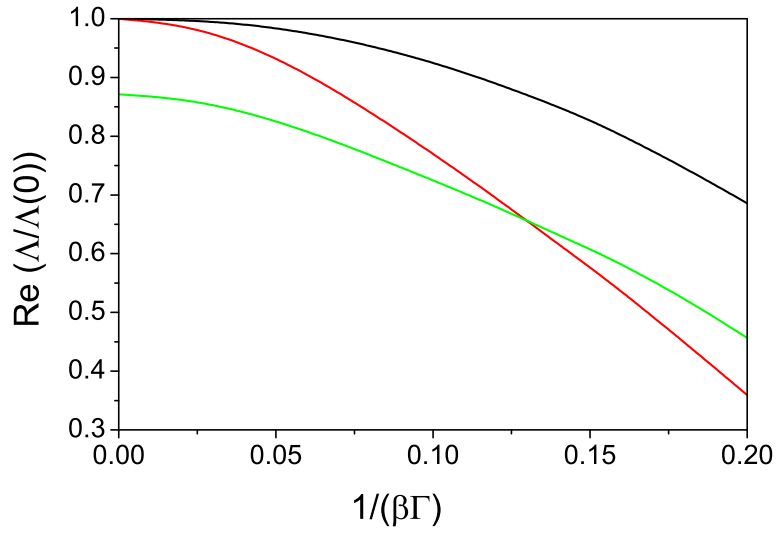
Fig. 33: Dependence of gain of (black) TEM$_{00}$ and (red) TEM$_{10}$ modes on betatron motion parameter $\hat{k}_\beta = 1/(\beta\bar{\Gamma})$. Values normalized to those at $\hat{k}_\beta \to 0$. Green curve shows ratio of gain of TEM$_{10}$ mode to gain of TEM$_{00}$ mode. Diffraction parameter, $B = 10$; energy spread parameter, $\hat{\Lambda}_T^2 \to 0$. Calculations made with simulation code FAST [77].
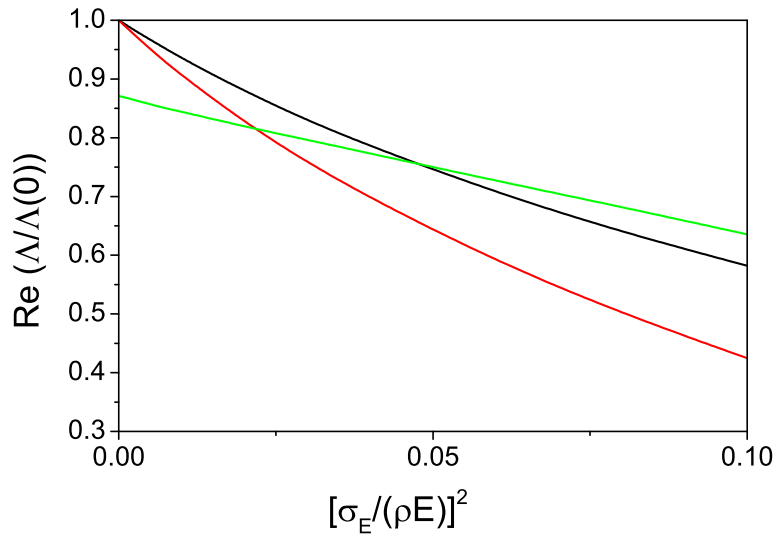

Fig. 34: Dependence of gain of (black) TEM$_{00}$ and (red) TEM$_{10}$ modes on energy spread parameter $\hat{\Lambda}_T^2$. Values normalized to those at $\hat{\Lambda}_T^2 \to 0$. Green curve shows ratio of gain of TEM$_{10}$ mode to gain of TEM$_{00}$ mode. Diffraction parameter, $B = 10$; betatron oscillation parameter, $\hat{k}_\beta \to 0$. Calculations made with simulation code FAST [77].

small charges may enable smaller values of the emittance, down to 0.5 mm-mrad, to be reached. The peak current may change in the range from 1 kA to 2 kA, depending on the tuning of the beam formation system. An estimate of the local energy spread is σ_{E} [MeV] $\simeq 0.1 \times I$ [kA]. The average beta function in the undulator is about 10 m.

Let us choose a reference working point with a radiation wavelength 8 nm, r.m.s. normalized emittance 1 mm-mrad, and beam current 1.5 kA. The parameters of the problem for this reference point are: diffraction parameter, $B = 17.2$; energy spread parameter, $\hat{\Lambda}_{\mathrm{T}}^2 = 1.7 \times 10^{-3}$; betatron motion parameter, $\hat{k}_\beta = 5.3 \times 10^{-2}$. Then the reduced parameters at other working points can be easily recalculated using the scaling:

$$\hat{k}_\beta \propto \frac{1}{\beta I^{1/2} \lambda^{1/4}}, \qquad \hat{\Lambda}_{\mathrm{T}}^2 \propto I \lambda^{1/2}, \qquad B \propto \frac{\epsilon_n \beta I^{1/2}}{\lambda^{1/4}} .$$

The effective contribution of the emittance to the longitudinal velocity spread (Eq. (27)) scales as

$$(\hat{\Lambda}_{\mathrm{T}}^2)_{\mathrm{eff}} \propto \frac{\epsilon_n^2}{\beta^2 I \lambda^{3/2}}$$

and equals 2.3×10^{-3} at the considered working point.

Analysing these simple dependencies in terms of their effect on mode separation, we can state that:

– Dependencies on the wavelength are relatively weak (except for $(\hat{\Lambda}_{\mathrm{T}}^2)_{\mathrm{eff}}$), i.e. one should not expect a significantly better transverse coherence at longer wavelengths. Moreover, mode separation can even be somewhat improved at shorter wavelengths, owing to a significant increase in $(\hat{\Lambda}_{\mathrm{T}}^2)_{\mathrm{eff}}$.
– Reduction of the peak current (by going to a weaker bunch compression) would lead to an improvement of mode separation (even though the energy spread parameter would smaller). Obviously, the peak power at the saturation would be reduced.
– Dependence on the normalized emittance is expected to be weak because of the two competing effects. Mode separation due to a change of the diffraction parameter can be to a large extent compensated by a change of the longitudinal velocity spread. As we will see next, this does indeed indeed in the considered parameter range.

A contour plot for the value of the diffraction parameter B for the value of beta function of 10 m and the value of beam current 1.5 kA is prese0nted in Fig. 35. We see that the value of the diffraction parameter is $B \gtrsim 10$ in the whole parameter space. Figure 31 shows the ratio of the field gain $\mathrm{Re}(\Lambda_{10}(\omega))$ to the value of the field gain $\mathrm{Re}(\Lambda_{00}(\omega))$ of the fundamental mode. We see that this ratio is above 0.8 in the whole range of parameters, and we can expect significant contribution of the first azimuthal mode to the total radiation power. We can also notice relatively weak dependencies on the emittance and on the wavelength.

We illustrate the general characteristics of FLASH with a specific numerical example for FLASH operating at the wavelength of 8 nm, peak current 1.5 kA, and r.m.s. normalized emittance 1 mm-mrad.

4.2.1   Radiation power

Figure 36 shows the evolution along the undulator of the radiation power in the fundamental harmonic. Higher values of the peak current and smaller emittances would enable higher radiation powers to be achieved. When the amplification process enters the non-linear stage, a process of non-linear harmonic generation takes place [53–61, 64]. Contour plots in Fig. 37 show the relevant contribution to the total power of the third and the fifth harmonic at the saturation point. A general observation is that the relative contribution of the higher harmonic is higher for smaller values of the emittance. With the value of the normalized emittance of 1 mm-mrad, partial contributions for the third and the fifth harmonic are
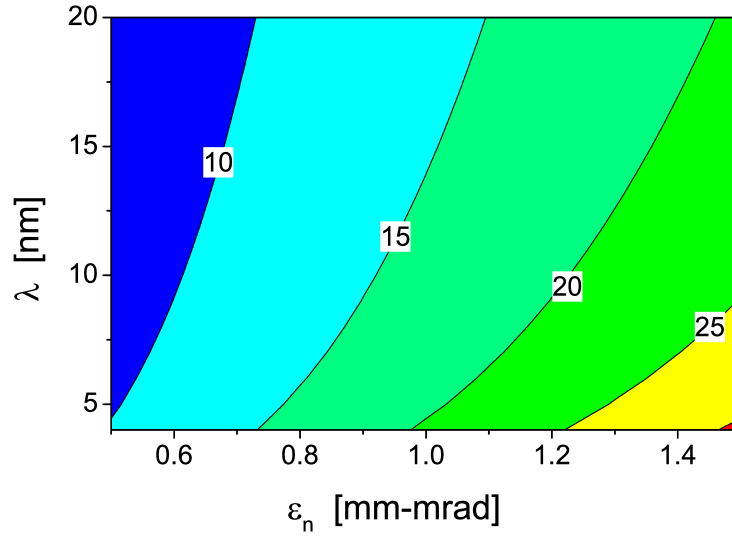
Fig. 35: Contour plot for diffraction parameter B versus normalized emittance and radiation wavelength. Beam current, 1.5 kA; beta function, 10 m. Calculations made with simulation code FAST [77].
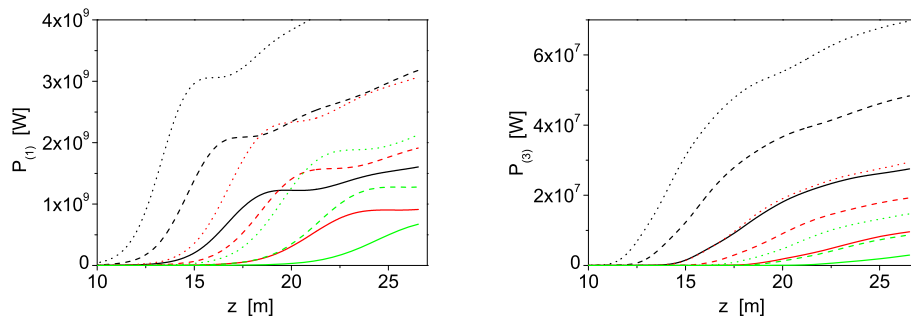

Fig. 36: Evolution of radiation power along undulator for (left) fundamental and (right) third harmonics. Colour codes (black, red, and green) refer to different emittances, $\epsilon_n = 0.5$, 1, and 1.5 mm-mrad. Line styles (solid, dash, and dot) refer to different values of peak current, 1 kA, 1.5 kA, and 2 kA. Radiation wavelength, 8 nm; beta function, 10 m. Calculations made with simulation code FAST [77].

0.7×10^{-2} and 2×10^{-4}, respectively. Note that this result is fairly close to that described by universal scaling law of Eq. (15), with an appropriate correction for longitudinal velocity spread derived in the previous section.

4.2.2 Temporal coherence

Plots in Fig. 38 show the coherence time for the whole parameter range for the fundamental and the third harmonic. In the high-gain linear regime, the coherence time increases as a square root of undulator length. It reaches a maximum value just before saturation point, and then decreases. The value of the coherence time at the saturation is close to that derived in the previous section in the framework of the one-dimensional theory (Eq. (17)), in terms of the FEL parameter ρ [4] and the number of cooperating electrons $N_c = I/(e\rho_{1D}\omega)$ [6]. The coherence time for the higher harmonics at the saturation point and in the post-saturation amplification stage can be derived using the scaling derived in the previous section—it scales inversely proportional to the harmonic number, while the relative spectrum bandwidth remains constant with the harmonic number.
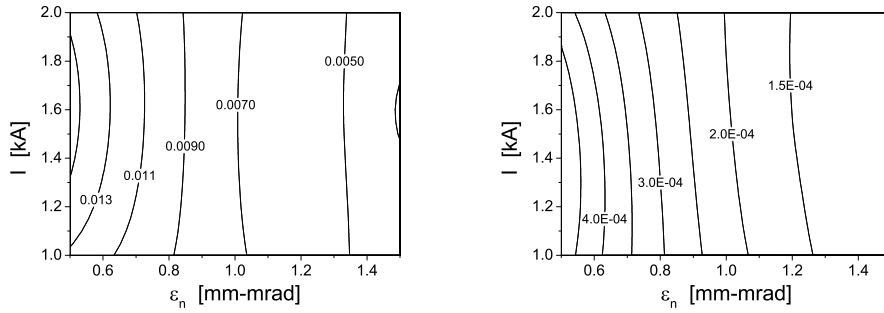
Fig. 37: Partial contribution of (left) third and (right) fifth harmonics to the total power versus peak beam current and emittance. Left and right parts of the plots are the saturation point and undulator end, respectively. Radiation wavelength, 8 nm; beta function, 10 m; beam current, 1.5 kA; r.m.s. normalized emittance, 1 mm-mrad. Calculations made with simulation code FAST [77].
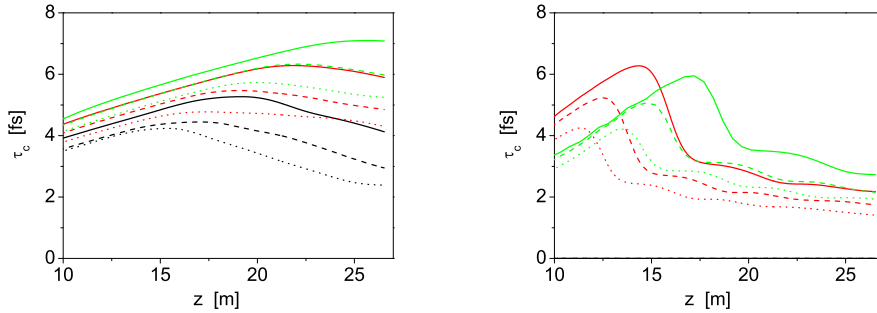

Fig. 38: Evolution along undulator of coherence time of radiation at (left) fundamental and (right) third harmonics. Colour codes (black, red, and green) refer to different emittance, $\epsilon_n = 0.5$, 1, and 1.5 mm-mrad. Line styles (solid, dash, and dot) refer to different values of peak current, 1 kA, 1.5 kA, and 2 kA. Radiation wavelength, 8 nm; beta function, 10 m. Calculations made with simulation code FAST [77].

4.2.3 Spatial coherence

Figure 39 presents an overview of the degree of transverse coherence in the considered parameter space. In our studies of coherent properties of FELs [41], we have found that, for an optimized SASE FEL, the degree of transverse coherence can be as high as 0.96. One can see from Fig. 39 that, in the considered cases, the degree of transverse coherence for the first harmonic is visibly less.

We should distinguish two effects limiting the degree of transverse coherence at FLASH. The first one is called mode degeneration and was intensively discussed in this paper. This physical phenomenon takes place at large values of the diffraction parameter [6]. Figure 40 shows the contribution of higher azimuthal modes to the total power for the specific example of emittance 1 mm-mrad and peak current 1.5 kA. The contribution of the first azimuthal modes decreases in the high-gain linear regime, but only to 12%, and then starts to increase in the non-linear regime, reaching 16% at the undulator end.

The second effect is connected with a finite longitudinal coherence; it was discovered in Ref. [39] and discussed in Refs. [41, 42]. The essence of the effect is a superposition of mutually incoherent fields produced by different longitudinally uncorrelated parts of the electron bunch. In the exponential gain regime, this effect is relatively weak, but it prevents a SASE FEL from reaching full transverse coherence, even when only one transverse eigenmode survives [39]. In the deep non-linear regime beyond FEL saturation, this effect can be strong and can lead to a significant degradation of the degree of transverse coherence [41, 42]. In particular, as one can see from Fig. 39, this effect limits the degree of transverse coherence to about 50% when FLASH operates in the deep non-linear regime.
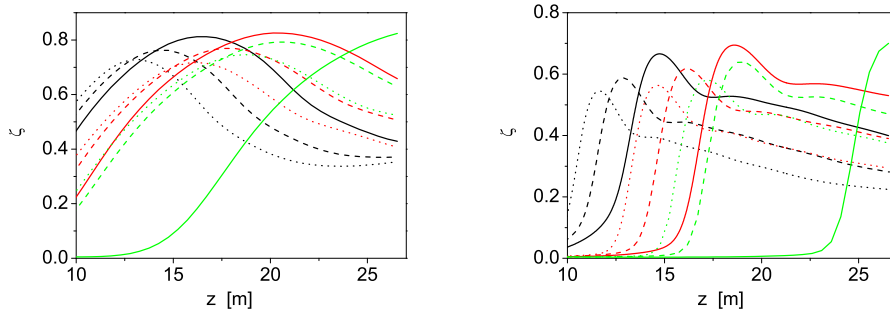
Fig. 39: Evolution along undulator of degree of transverse coherence of radiation. Left: fundamental frequency (8 nm). Right: third harmonic (2.66 nm). Colour codes (black, red, and green) refer to different emittances, $\epsilon_n = 0.5$, 1, and 1.5 mm-mrad. Line styles (solid, dash, and dot) refer to different values of peak current, 1 kA, 1.5 kA, and 2 kA. Radiation wavelength, 8 nm; beta function, 10 m. Calculations made with simulation code FAST [77].
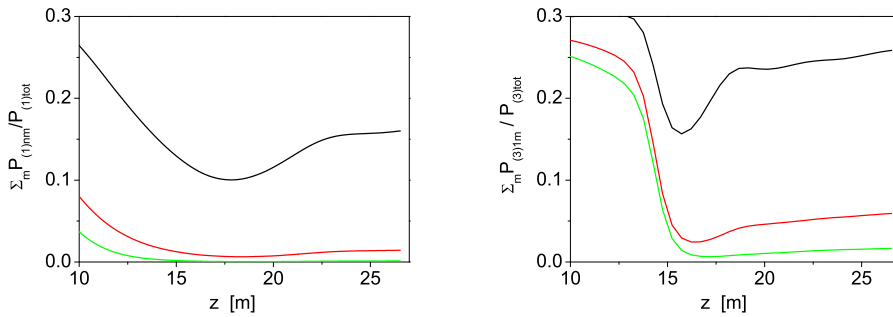

Fig. 40: Partial contribution of the higher azimuthal modes for (left) fundamental and (right) third harmonic. Black, red, and green curves refer to modes with $n = \pm 1$, $n = \pm 2$, and $n = \pm 3$, respectively. Radiation wavelength, 8 nm; beta function, 10 m; beam current, 1.5 kA; r.m.s. normalized emittance, 1 mm-mrad. Calculations made with simulation code FAST [77].

Higher harmonics are derived from the non-linear process governed by the fundamental harmonic. As a result, the coherence properties of the harmonics follow the same tendencies as the fundamental, but with visibly lower degree of transverse coherence [65].

Note that an easier way to improve the transverse coherence dramatically would be to decrease the beam current such that saturation is achieved at the very end of the undulator. This would eliminate not only the degradation in the deep non-linear regime, but would also improve the mode selection process because the diffraction parameter is then reduced while the velocity spread due to emittance is increased. According to our expectations, the degree of transverse coherence might reach around 90% in this regime. Such a regime was realized at FLASH on a user's demand, but it is not typical for the machine operation because the peak power is low due to a low peak current.

One can also suppress unwanted effects in the deep non-linear regime by kicking the electron beam at the saturation point (or close to it) when the peak current is high. Then one can still have a high power and an improved (about 70–80%) degree of transverse coherence. Further improvement could be achieved by reducing the beta function (thus improving the mode selection, as discussed).

4.2.4 Pointing stability and mode degeneration

Mode degeneration has a significant impact on the pointing stability of a SASE FEL. Let us illustrate this effect with a specific example for FLASH, operating with average energy in the radiation pulse of 60 µJ. The left plot in Fig. 41 shows evolution along the undulator of the radiation energy in azimuthally
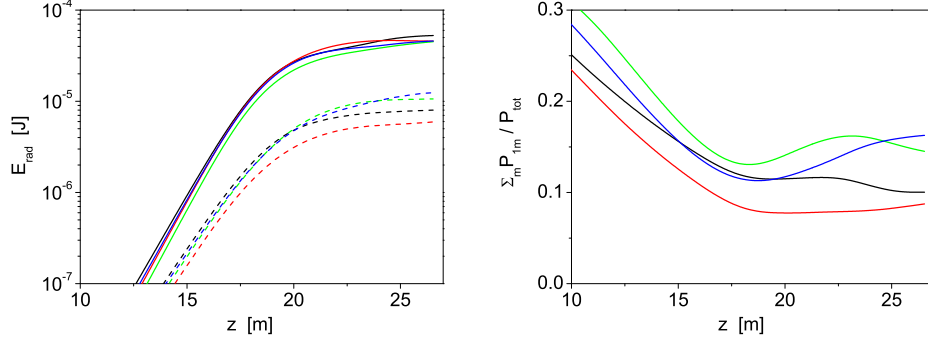
Fig. 41: Left: evolution of energy in radiation pulse versus undulator length. Colour codes (black to blue) correspond to different shots. Line styles correspond to total energy in the azimuthally symmetrical $\sum \mathrm{TEM}_{0m}$ modes (solid lines), and in the first azimuthal modes $\sum \mathrm{TEM}_{1m}$ (dashed lines). Right: partial contribution of the first azimuthal modes to the total radiation power, $\sum P_{1m}/P_{\mathrm{tot}}$. Radiation wavelength, 8 nm; beta function, 10 m; beam current, 1.5 kA; r.m.s. normalized emittance, 1 mm-mrad. Calculations made with simulation code FAST [77].

symmetrical modes and of the energy in the modes with azimuthal index $n = \pm 1$. The right plot in this figure shows relative contribution to the total radiation energy of the modes with azimuthal index $n = \pm 1$. Four consecutive shots are shown here. Temporal profiles of the radiation pulses are presented in Fig. 42. The intensity distributions in the far zone for these four shots are shown in four rows in Fig. 43. Four profiles on the left-hand side of each row show intensity distributions in the single slices for the times 40 fs, 50 fs, 60 fs, and 70 fs. The right column presents intensity profiles averaged over full shots. We see that the transverse intensity patterns in the slices have a rather complicated shape, owing to interference of the fields of statistically independent modes with different azimuthal indexes. The shape of the intensity distributions changes on a scale of coherence length. Averaging the slice distributions over the radiation pulse results in a smoother distribution. However, it can clearly be seen that the spot shape of a short radiation pulse changes from pulse to pulse. The centre of gravity of the radiation pulse visibly jumps from shot to shot. The position of the pulse also jumps from shot to shot; this is frequently referred to as bad pointing stability. Note that the effect illustrated here is a fundamental one, which takes place as a result of the mode degeneration when the contribution of the higher azimuthal modes to the total power is pronounced (10–15% in our case). Only in the case of a long radiation pulse, or after averaging over many pulses, do we come asymptotically to an azimuthally symmetrical radiation distribution.

4.3 Optimized SASE FEL

The best properties of the output radiation from SASE FEL correspond to the case when the fundamental TEM_{00} mode dominates over higher-order spatial modes. Thus, the standard procedure for optimization of the SASE FEL is optimization for the maximum gain of the fundamental mode. For given parameters of the electron beam and the undulator there always exists an optimum focusing beta function β_{opt}, which provides a minimum gain length L_{g} of the fundamental mode [66, 80]:

$$L_{\mathrm{g0}} = 1.67 \left(\frac{I_{\mathrm{A}}}{I}\right)^{1/2} \frac{(\epsilon_n \lambda_{\mathrm{w}})^{5/6}}{\lambda^{2/3}} \frac{(1+K^2)^{1/3}}{K A_{\mathrm{JJ}}} (1 + \delta) \, ,$$

$$\beta_{\mathrm{opt}} \simeq 11.2 \left(\frac{I_{\mathrm{A}}}{I}\right)^{1/2} \frac{\epsilon_n^{3/2} \lambda_{\mathrm{w}}^{1/2}}{\lambda K A_{\mathrm{JJ}}} (1 + 8\delta)^{-1/3} \, ,$$

$$\delta = 131 \frac{I_{\mathrm{A}}}{I} \frac{\epsilon_n^{5/4}}{\lambda^{1/8} \lambda_{\mathrm{w}}^{9/8}} \frac{\sigma_\gamma^2}{(K A_{\mathrm{JJ}})^2 (1 + K^2)^{1/8}} \, . \tag{28}$$
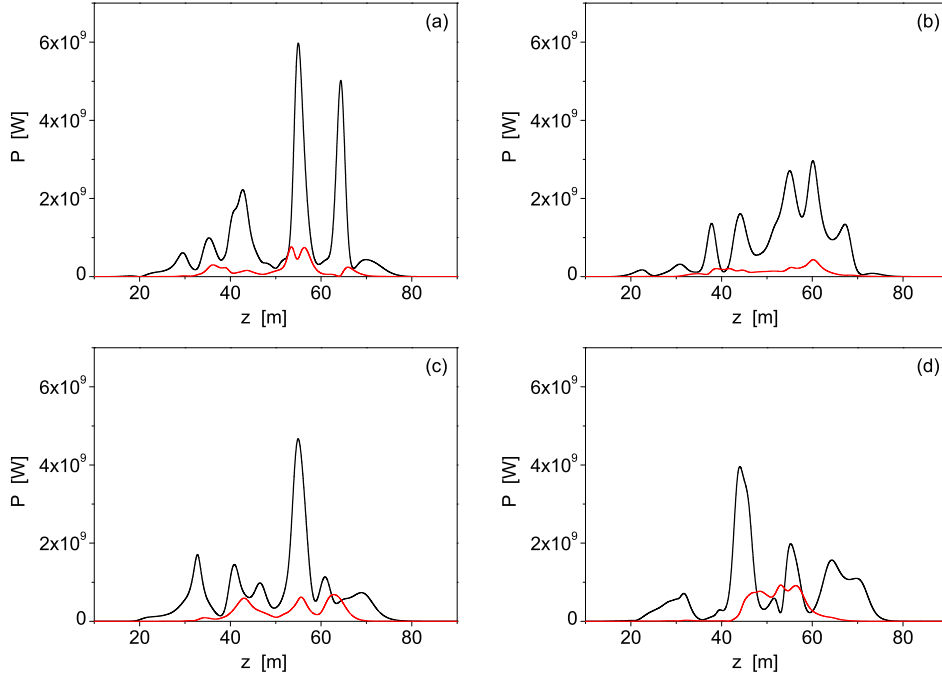
Fig. 42: Temporal structure of four radiation pulses. Black: power of azimuthally symmetrical modes. Red: power of first azimuthal modes. Radiation wavelength, 8 nm; beta function, 10 m; beam current, 1.5 kA; r.m.s. normalized emittance, 1 mm-mrad; undulator length, 27 m. Calculations made with simulation code FAST [77].

A realization of the conditions of Eq. (28) is referred to as an optimized FEL amplifier. Sometimes, for technical reasons, the focusing beta function might be $\beta > \beta_{\text{opt}}$. In such a case, the gain length can be approximated as follows:

$$L_{\text{g}}(\beta) \simeq L_{\text{g}}(\beta_{\text{opt}}) \left[1 + \frac{(\beta - \beta_{\text{opt}})^2 (1 + 8\delta)}{4\beta_{\text{opt}}^2} \right]^{1/6}, \qquad \text{for } \beta > \beta_{\text{opt}} \tag{29}$$

Here $\epsilon_n = \gamma\epsilon$ is the r.m.s. normalized emittance, $\sigma_\gamma = \sigma_\varepsilon/mc^2$ is the r.m.s. energy spread (in units of the rest energy), and factor A_{JJ} is the usual coupling factor defined in the previous sections. Equation (28) provides an accuracy better than 5% in the range of parameters

$$1 < \frac{2\pi\epsilon}{\lambda} < 5, \qquad \delta < 2.5 \left\{ 1 - \exp\left[-\frac{1}{2} \left(\frac{2\pi\epsilon}{\lambda} \right)^2 \right] \right\} \tag{30}$$

The saturation length of the optimized SASE FEL is given by [42]:

$$L_{\text{sat}} \simeq 0.6 \, L_{\text{g}} \ln \left(\frac{N_\lambda L_{\text{g}}}{\lambda_{\text{w}}} \right). \tag{31}$$

Here, $N_\lambda = I\lambda/c$ is the number of electrons per wavelength. When operating vacuum ultraviolet and X-ray SASE FELs, one typically has $L_{\text{sat}} \simeq (10 \pm 1) \times L_{\text{g}}$.

For small energy spread, $\delta \ll 1$, the physical parameters describing operation of the optimized FEL, the diffraction parameter B, and the parameter of betatron oscillations $\hat{k}_\beta$, are functions of the only parameter $\hat{\epsilon} = 2\pi\epsilon/\lambda$ [6,41]:

$$B = 2\bar{\Gamma}\sigma^2\omega/c \simeq 12.5 \times \hat{\epsilon}^{5/2},$$
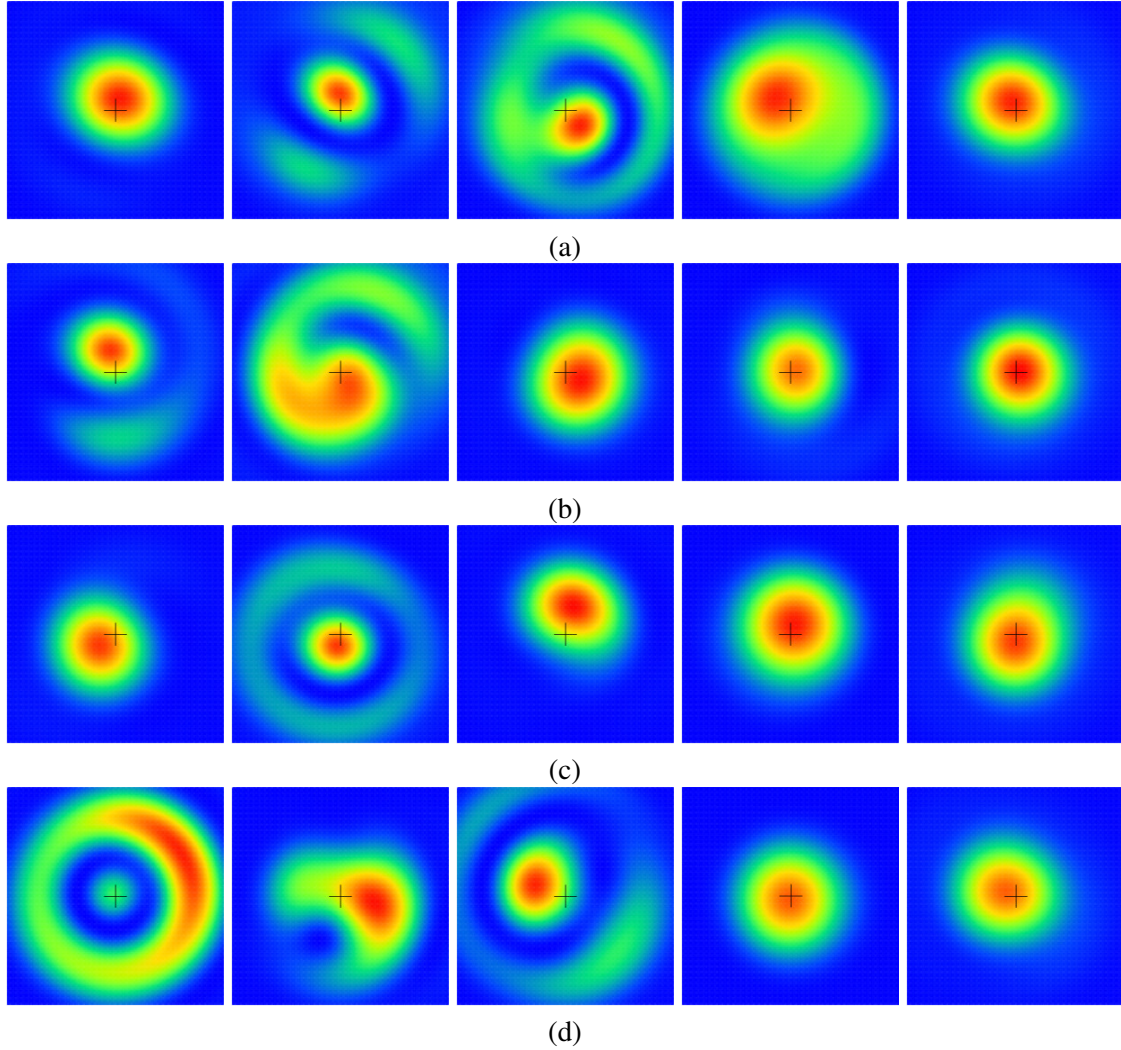$$\hat{k}_\beta = 1/(\beta\bar{\Gamma}) \simeq 0.158 \times \hat{\epsilon}^{-3/2}. \tag{32}$$

Fig. 43: Profiles of radiation intensity in the far zone. Rows (a–d) correspond to specific shots with temporal structures presented in Fig. 42 (plots a–d). Profiles on the right-hand side show average intensity over full pulse. Profiles 1 to 4 from the left-hand side show intensity distributions of selected slices corresponding to 40 fs, 50 fs, 60 fs, and 70 fs, respectively. Crosses denote the geometrical centre of the radiation intensity averaged over many shots. Radiation wavelength, 8 nm; beta function, 10 m; beam current, 1.5 kA; r.m.s. normalized emittance, 1 mm-mrad; undulator length, 27 m. Calculations made with simulation code FAST [77].

The diffraction parameter B directly relates to diffraction effects and the formation of transverse coherence. If diffraction expansion of the radiation on a scale of the field gain length is comparable to the transverse size of the electron beam, we can expect a high degree of transverse coherence. For this range of parameters, the value of the diffraction parameter is small. If diffraction expansion of the radiation is small (which happens at large values of the diffraction parameter), we can expect significant degradation in the degree of transverse coherence. This effect occurs simply because different parts of the beam produce radiation nearly independently. In terms of the radiation expansion in the eigenmodes of Eq. (25), this range of parameters corresponds to the degeneration of modes [6]. The diffraction parameter for an optimized XFEL exhibits strong dependence on the parameter $\hat{\epsilon}$ (see Eq. (32)), and we can expect the degree of transverse coherence to drop rapidly with the increase of the parameter $\hat{\epsilon}$.

4.3.1 Characteristics of the radiation from optimized SASE FEL operating in the saturation regime

Figure 1 shows the evolution of the main characteristics of a SASE FEL along the undulator. If one traces the evolution of the brilliance (degeneracy parameter) of the radiation along the undulator length, there is always a point (defined as the saturation point [41]) where the brilliance reaches a maximum value. The best properties of the radiation in terms of transverse and longitudinal coherence are achieved just before the saturation point, and these values then degrade significantly, despite the radiation power continuing to increase with undulator length.

Application of similarity techniques allows us to derive universal parametric dependencies of the output characteristics of the radiation at the saturation point. As mentioned in Section 2, within accepted approximations (optimized SASE FEL and negligibly small energy spread in the electron beam), normalized output characteristics of a SASE FEL at the saturation point are functions of only two parameters: $\hat{\epsilon} = 2\pi\epsilon/\lambda$ and the number of electrons in the volume of coherence $N_c = IN_g\lambda/c$, where $N_g = L_g/\lambda_w$ is the number of undulator periods per gain length. Characteristics of practical interest are: saturation length L_{sat}, saturation efficiency $\eta_{sat} = P_{sat}/P_b$ (ratio of the radiation power to the electron beam power $P_b = \gamma mc^2 I/e$), coherence time τ_c, degree of transverse coherence ζ, degeneracy parameter δ, and brilliance B_r. Applications of similarity techniques to the results of numerical simulations of a SASE FEL [41] gives us the following result:

$$\hat{L}_{sat} = \bar{\Gamma}L_{sat} \simeq 2.5 \times \hat{\epsilon}^{5/6} \times \ln N_c \, ,$$
$$\hat{\eta} = P/(\bar{\rho}P_b) \simeq 0.17/\hat{\epsilon} \, ,$$
$$\hat{\tau}_c = \bar{\rho}\omega\tau_c \simeq 1.16 \times \sqrt{\ln N_c} \times \hat{\epsilon}^{5/6} \, ,$$
$$\sigma_\omega = \sqrt{\pi}/\tau_c \, . \tag{33}$$

These expressions provide reasonable practical accuracy for $\hat{\epsilon} \gtrsim 0.5$. With logarithmic accuracy in terms of N_c, characteristics of the SASE FEL expressed in a normalized form are only functions of the parameter $\hat{\epsilon}$. The saturation length, FEL efficiency, and coherence time exhibit monotonous behaviour in the parameter space of modern XFELs ($\hat{\epsilon} \simeq 0.5, \ldots, 5$). The situation with the degree of transverse coherence at saturation is more complicated, as we can see from Fig. 44—degradation of spatial coherence at small emittances seems to be counter-intuitive. To understand the origin of this phenomenon, we trace in Fig. 45 the degree of transverse coherence ζ versus the reduced propagation coordinate z/z_{sat} for different values of the parameter $\hat{\epsilon}$. The typical behaviour of the degree of transverse coherence is that it increases in the exponential stage of amplification, reaches a maximum value at the saturation point, and degrades in the post-saturation regime. The increase of the degree of transverse coherence in the exponential stage of amplification happens because of two physical effects. The first effect is the mode selection process, which is reflected in Eq. (25). As we have shown, smaller values of the diffraction parameter provide better mode selection. Simple calculations of the gain (see Fig. 46) shows that, for values of diffraction parameter less than or approximately equal to one (diffraction-limited beam), one should expect almost 100% contribution of the fundamental mode to the total power. However, this is not the case. The maximum degree of transverse coherence is degraded for smaller emittances, as we can see from Fig. 45. The physical effect responsible for such a degradation is the interdependence of the poor longitudinal coherence and transverse coherence [39]. We pay attention to the feature that, owing to the start-up from shot noise, every radiation mode entering Eq. (25) is excited within a finite spectral bandwidth. This means that, in the high-gain linear regime, the radiation of the SASE FEL is formed by many fundamental TEM$_{00}$ modes with different frequencies. The transverse distribution of the radiation field of the mode is also different for different frequencies. A smaller value of the diffraction parameter (i.e. smaller value of $\hat{\epsilon}$) corresponds to larger deviation of the radiation mode from the plane wave. This effect explains the degradation of the transverse coherence at small values of $\hat{\epsilon}$. The degree of transverse coherence asymptotically approaches unity as $(1-\zeta) \propto 1/z \propto 1/\ln N_c$ at small values of the emittance. The maximum value of the degree of transverse coherence is about 0.96 and is achieved at $\hat{\epsilon} \simeq 1$.
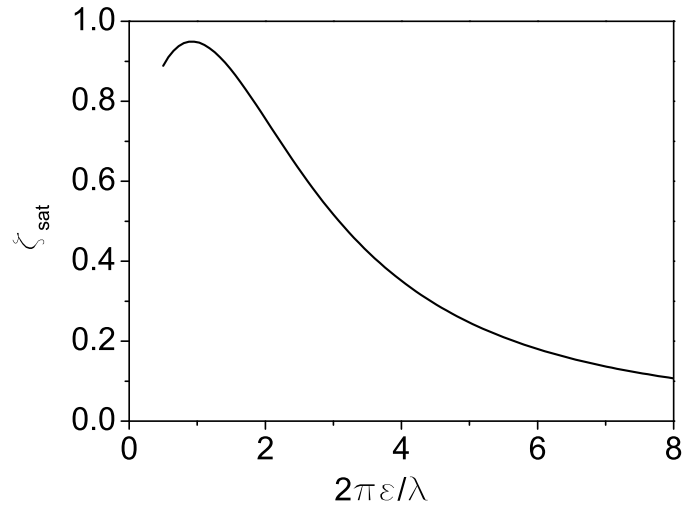
Fig. 44: Degree of transverse coherence ζ_{sat} in saturation point versus $\hat{\epsilon}$. Number of electrons in coherence volume, $N_c = 4 \times 10^6$. Calculations made with simulation code FAST [77].
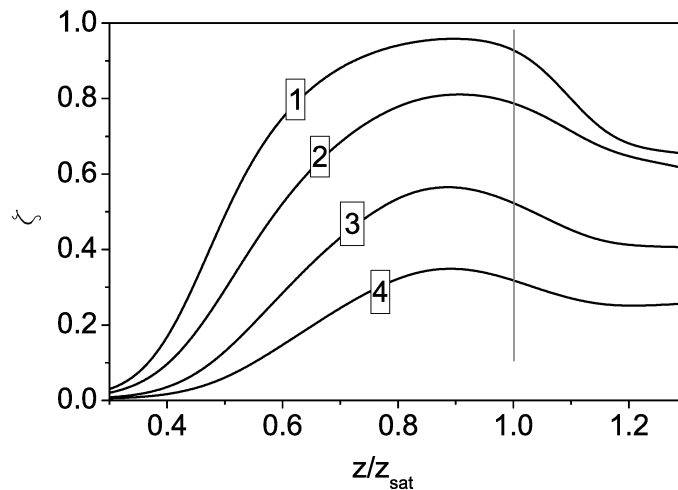

Fig. 45: Evolution of degree of transverse coherence along undulator length for $\hat{\epsilon} = 0.5, 1, 2, 3$, and 4. Undulator length normalized to saturation length. Calculations made with simulation code FAST [77].

When the parameter $\hat{\epsilon}$ is large, the diffraction parameter is also large, leading to degeneration of the radiation modes. The amplification process in the SASE FEL passes a limited number of field gain lengths and, starting from some value of $\hat{\epsilon}$ the linear stage of amplification, becomes too short to provide the mode selection process of Eq. (25). When the amplification process enters the non-linear stage, the mode content of the radiation becomes even richer, owing to independent growth of the radiation modes in the non-linear medium (see Fig. 47). Thus, at large values of $\hat{\epsilon}$, the degree of transverse coherence is limited by poor mode selection. Analytical estimates show that, in the limit of large emittance, $\hat{\epsilon} \gg 1$, the degree of transverse coherence scales as $1/\hat{\epsilon}^2$. To avoid complications, we present here just a fit for
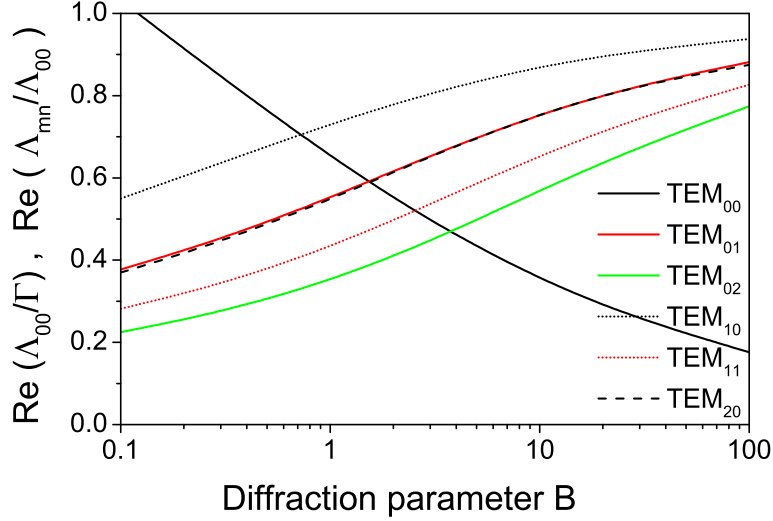
Fig. 46: Ratio of maximum gain of higher modes to maximum gain of fundamental mode $\mathrm{Re}(\Lambda_{mn})/\mathrm{Re}(\Lambda_{00})$ versus diffraction parameter B. Energy spread parameter, $\hat{\Lambda}_{\mathrm{T}}^2 \to 0$, betatron motion parameter, $\hat{k}_\beta \to 0$. Colour codes refer to radial index of the mode: 0, black; 1, red; 2, green. Line type codes refer to azimuthal index of the mode: 0, solid line, 1, dotted line; 2, dashed line. Black solid line shows gain of the fundamental mode $\mathrm{Re}(\Lambda_{00})/\bar{\Gamma}$. Calculations made with simulation code FAST [77].

the degree of transverse coherence for the number of electrons in the coherence volume $N_{\mathrm{c}} = 4 \times 10^6$:

$$\zeta_{\mathrm{sat}} \simeq \frac{1.1\hat{\epsilon}^{1/4}}{1 + 0.15\hat{\epsilon}^{9/4}} \,. \tag{34}$$

Recalculation from reduced to dimensional parameters is straightforward. For instance, the saturation length is $L_{\mathrm{sat}} \simeq 0.6 \times L_{\mathrm{g}} \times \ln N_{\mathrm{c}}$. Using Eq. (33), we can calculate the normalized degeneracy parameter $\hat{\delta} = \hat{\eta}\zeta\hat{\tau}_{\mathrm{c}}$ and then the brilliance (Eq. (9)):

$$B_r \left[\frac{\text{photons}}{\text{sec mrad}^2 \text{ mm}^2 \text{ 0.1\% bandw.}} \right] \simeq 4.5 \times 10^{31} \times \frac{I[\mathrm{kA}] \times E[\mathrm{GeV}]}{\lambda[\ ]} \times \hat{\delta} \,. \tag{35}$$

4.3.2 Coherence properties of the higher odd harmonics

We start the analysis with a specific numerical example corresponding to $\hat{\epsilon} = 0.5$. This operating point corresponds to the maximum degree of transverse coherence that can be achieved in SASE FEL [41, 42, 44]. Figure 48 shows a slice of the temporal structure of the radiation pulse from a SASE FEL operating in the saturation regime. Already, this specific example provides a lot of physical information. We note that the spikes of all harmonics are well aligned in space, illustrating an effect of non-linear harmonic generation: higher harmonics radiate only by those parts of the electron bunch that have been effectively modulated by the fundamental harmonic. We also notice that the typical scale of the radiation intensities of the third (fifth) harmonic is in the range of a few per cent (per mille) of the fundamental. Even a brief look at the spike widths in Fig. 48 gives us an idea that the coherence time of the third harmonic is significantly less than that of the fundamental harmonic. The spikes of the fifth harmonic are shorter than those of the third harmonic; thus, the coherence time of the fifth harmonic should be even less.

The plots in Fig. 49 show the evolution along the undulator of the radiation power and brilliance. The longitudinal coordinate is normalized to the saturation length of the fundamental harmonic. The brilliance and power of the harmonics are normalized to the values corresponding to the saturation point of the fundamental harmonic. We see that the radiation powers of all harmonics continue to increase
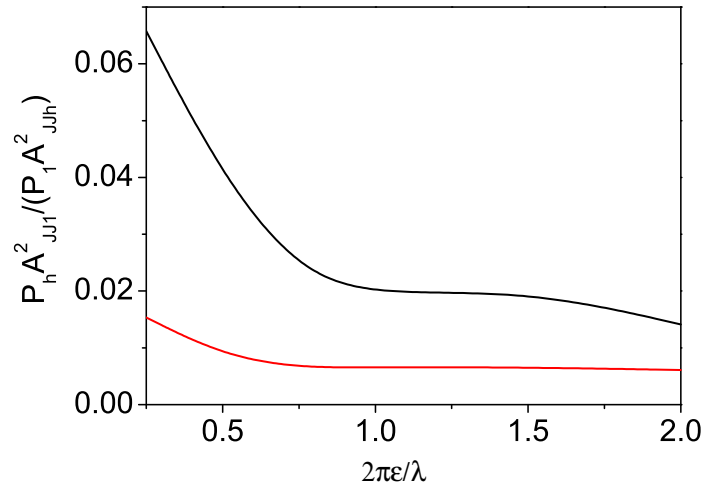
Fig. 47: Optimized XFEL. Ratio of powers in the (black) third and (red) fifth harmonics to the power of the fundamental harmonic versus $\epsilon = \hat{2\pi\epsilon}/\lambda$; SASE FEL operates at saturation point. Calculations made with simulation code FAST [77].
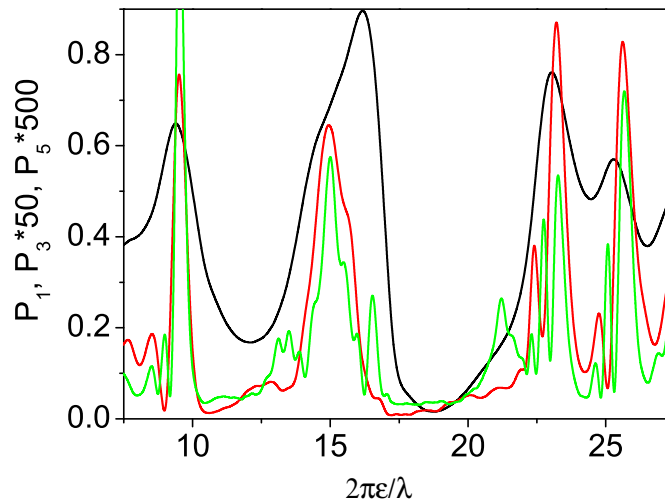

Fig. 48: Optimized XFEL. Temporal structure of radiation pulse in saturation point for $\hat{\epsilon} = 0.5$. Black, red, and green lines refer to first, third, and fifth harmonics, respectively. Calculations made with simulation code FAST [77].
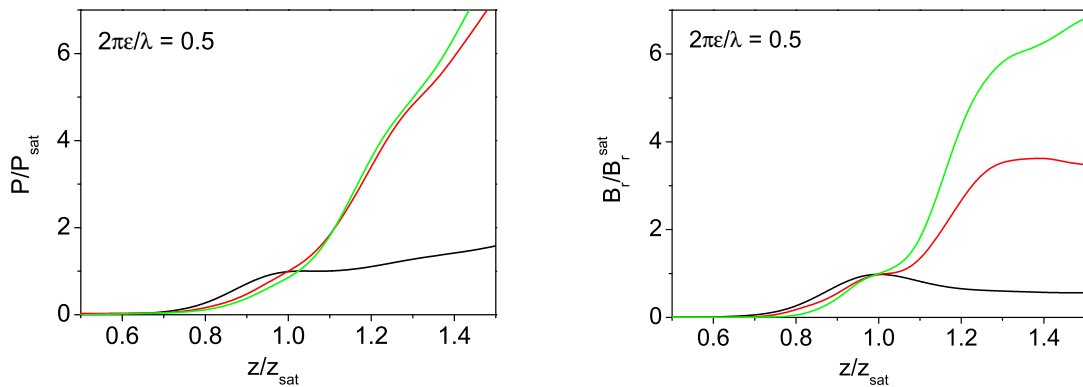
Fig. 49: Left: optimized XFEL: FEL power versus undulator length. Right: brilliance versus undulator length. All values normalized to values corresponding to the values at the saturation point of the first harmonic. Black, red, and green lines refer to first, third, and fifth harmonic, respectively. Calculations made with simulation code FAST [77].

after the saturation point of the fundamental harmonic. The increase in power of the third and the fifth harmonic is visibly faster than that of the fundamental. An important feature is that the brilliances of the higher harmonics also continue to increase after the saturation point. The maximum brilliance of the higher harmonics is reached in the deep non-linear regime, mainly as a result of faster growth of the harmonic radiation power with respect to the fundamental. This means that in a parameter range of $\hat{\epsilon} \approx 0.5$, the electron beam after saturation remains a relatively good amplification medium for higher harmonics. The contribution of higher harmonics to the total radiation power depends strongly on how long the amplification process develops after the saturation point.

The plots in Fig. 50 show the evolution along the undulator of the coherence time and degree of transverse coherence. We multiplied the coherence time by the harmonic number h to bring all curves into scale. We find an important feature; that coherence time in the saturation regime scales inversely proportional to harmonic number. Moreover, the relative spectrum bandwidth $\Delta\omega_h/\omega_h$ remains constant for all harmonics. This finding confirms the result obtained earlier in the framework of the one-dimensional model [64]. Note that recent measurements of the harmonic properties at FLASH and LCLS [13, 81] are in good qualitative agreement with the results reported here.

Figure 49 shows the evolution of the degree of transverse coherence along the undulator. Note that we illustrate the parameter space providing the maximum degree of transverse coherence in the fundamental harmonic (about 95%) for an optimized X-ray FEL. An important observation is that the degree of transverse coherence for higher harmonics is visibly less. There is nothing unusual in this result. Qualitatively, it can be explained by the general feature of frequency multiplication schemes, which also amplify noise progressively with harmonic number [82]. The fundamental harmonic already contains visible noise content, resulting in a reduced degree of transverse coherence, and we can readily expect further reduction for higher harmonics. An example of similar physical behaviour is the degradation of longitudinal coherence in the high-gain harmonic generation scheme [83].

As already mentioned, the characteristics of the optimized FEL in the saturation point depend only on the parameter, $\hat{\epsilon}$. Figure 51 shows the dependence of the degree of transverse coherence for the first, third, and fifth harmonic on the value of the emittance parameter. We see that the maximum values of the degree of transverse coherence correspond to values of $\hat{\epsilon} \approx 0.5$. While the coherence properties of the fundamental harmonic do not change too much when $\hat{\epsilon}$ increases to 2, we obtain a significant degradation for the third harmonic.
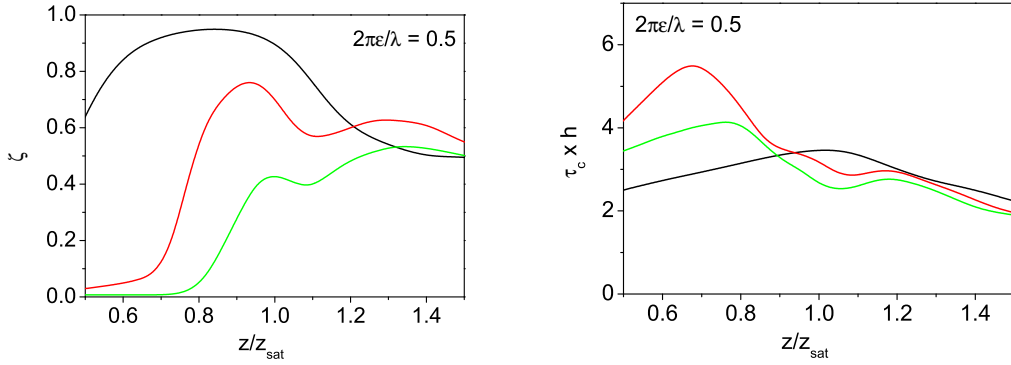
Fig. 50: Optimized XFEL. Left: degree of transverse coherence, ζ. Right: normalized coherence time, $\hat{\tau}_c$, versus undulator length for $\hat{\epsilon} = 0.5$. Black, red, and green lines refer to first, third, and fifth harmonic, respectively. Coherence time is multiplied by corresponding harmonic number h. Calculations made with simulation code FAST [77].
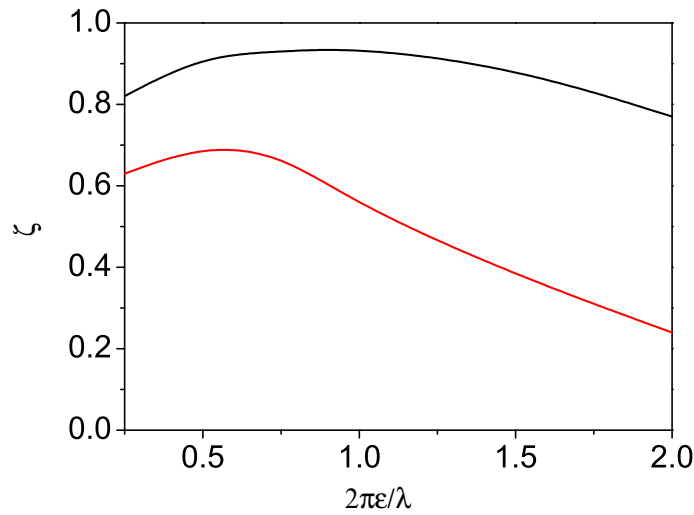

Fig. 51: Optimized XFEL: degree of transverse coherence ζ_{sat} in saturation versus parameter $\hat{\epsilon} = 2\pi\epsilon/\lambda$. Black and red lines refer to first and third harmonics, respectively. Calculations made with simulation code FAST [77].

When we analyse expressions for the radiation power, we find that the dependencies for the ratios of the power of higher harmonics to the fundamental become universal functions of emittance parameter when we factorize them with factor A_{JJh}^2/A_{JJ1}^2. Relevant plots are presented in Fig. 47. For large values of the undulator parameter K, asymptotic values of A_{JJh}^2/A_{JJ1}^2 are equal to 0.22 and 0.11 for the third, and fifth harmonics, respectively. In the range of emittance parameter from 0.25 to 2, contributions to the total power of the third (fifth) harmonic are between 0.3% and 1.4% (0.07% and 0.16%). Note that the contribution of higher harmonics to the total power increases in the deep non-linear regime, and may constitute a substantial amount (see Fig. 49).
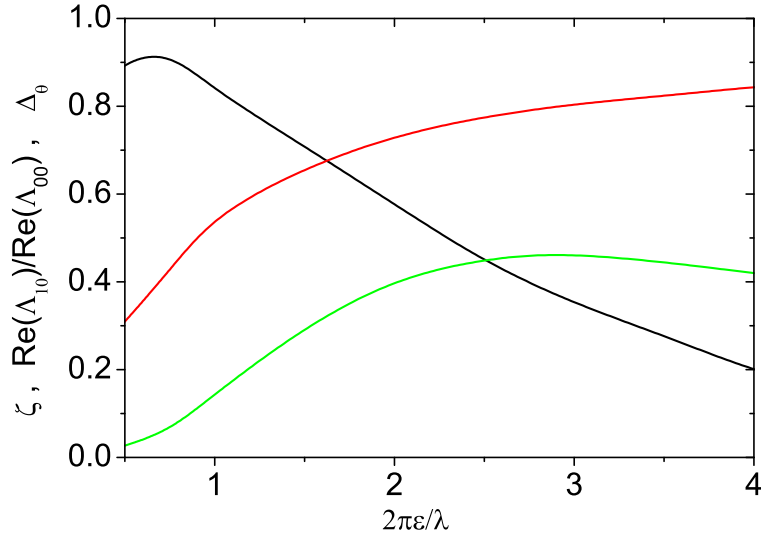
Fig. 52: Optimized SASE FEL: (black) degree of transverse coherence ζ, (red) ratio of gain $\mathrm{Re}(\Lambda_{10})/\mathrm{Re}(\Lambda_{00})$, and (green) r.m.s. deviation of photon beam centre of gravity Δ_θ in terms of r.m.s. size of photon beam. Simulations run with code FAST [77].
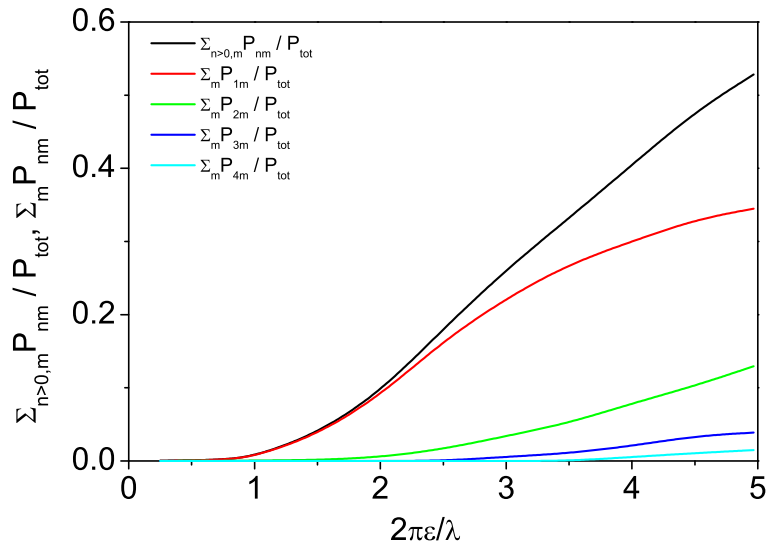

Fig. 53: Optimized SASE FEL: partial contributions of asymmetrical modes to total power versus emittance parameter $\hat{\epsilon} = 2\pi\epsilon/\lambda$; SASE FEL operates in saturation. Black curve is total contribution of asymmetrical modes, and colour curves correspond to azimuthal indices from 1 to 4. Simulations run with code FAST [77].

4.3.3 Mode degradation and pointing stability

The diffraction parameter scales with the emittance parameter as $B \simeq 13 \times \hat{\epsilon}^{5/2}$. Starting from $\hat{\epsilon} > 1$ the gain of the TEM_{10} mode approaches very close to the gain of the ground TEM_{00} mode (see Fig. 52). The contribution of the TEM_{10} mode to the total power progresses with the increase of the emittance parameter (see Fig. 53). Starting from $\hat{\epsilon} > 2$, the azimuthal modes TEM_{2n} appear in the mode contents, and so on. The maximum value of the degree of transverse modes (which occurs at the end of the linear regime) degrades gradually with the increase of the emittance parameter (see Fig. 52).

Mode degeneration has a significant impact on the pointing stability of a SASE FEL. Figure 53 shows the relative contribution to the total radiation energy of the modes with higher azimuthal indices. Typical intensity distributions in the far zone are shown in Fig. 54. Transverse intensity patterns in
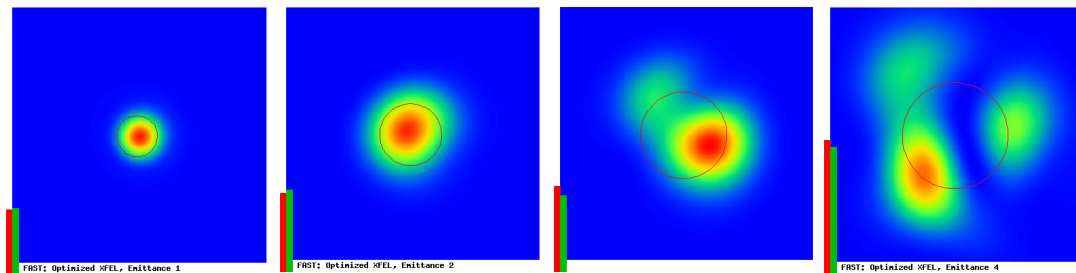
Fig. 54: Typical slice distribution of radiation intensity for optimized SASE FEL with (left to right) $\hat{\epsilon} = 1, 2, 3, 4$. Circle denotes r.m.s. spot size. SASE FEL operates at saturation. Simulations run with code FAST [77].

Table 1: Parameter space of X-ray FELs

	LCLS	SACLA	EXFEL	SWISS FEL	PAL XFEL
Energy [GeV]	13.6	8.0	17.5	5.8	10
Wavelength [A]	1.5	0.6	0.5	0.7	0.6
ϵ_n [mm-rad]	0.4	0.4	0.4	0.4	0.4
$\hat{\epsilon}$	1	2.7	1.5	3.4	2.1

slices have a rather complicated shape, owing to the interference of the fields of statistically independent modes with different azimuthal indices. These slice distributions are essentially non-Gaussian when the relative contribution of higher azimuthal modes to the total power approaches 10%. The shapes of the intensity and phase distributions change drastically on a scale of the coherence length, and the source point position and pointing jumps from spike to spike. Figure 52 presents a quantitative description of this phenomenon, using the notion of the r.m.s. deviation of the photon beam centre of gravity Δ_θ expressed in terms of the r.m.s. size of the photon beam. We see that there is no perfect pointing of the photon beam, and that for $\hat{\epsilon} \gtrsim 2$ fluctuations of the pointing exceed 40%. Averaging of slice distributions over a radiation pulse results in a smoother distribution. However, with a limited number of longitudinal modes, the centre of gravity of the radiation pulse (position) and its shape jitter from shot to shot; this is frequently referred to as poor pointing stability. This effect has been observed at FLASH [47] experimentally, and should evidently take place at other X-ray facilities. Only in the case of a long radiation pulse, or after averaging over many pulses, does the intensity distribution approach, asymptotically, an azimuthally symmetrical shape.

Table 1 presents a list of parameters of the X-ray FELs compiled for the shortest design wavelength [17–19, 22, 24]. We assume the normalized emittance to be the same for all cases ($\epsilon_n = 0.4$ mm-mrad). A lower electron beam energy results in a larger value of the emittance parameter, and the output radiation will have poor spatial coherence and poor pointing stability of the photon beam. Note that the spatial jitter is of a fundamental nature (shot noise in the electron beam), and takes place even for an 'ideal' machine.

There are very limited means of suppressing the mode degeneration effect by controlling the spread of longitudinal velocities (due to energy spread and emittance) [6, 51, 68]. Energy spread can be increased with a laser heater [84]. The price for this improvement is a significant increase in saturation length and reduction of the FEL power. Stronger focusing of the electron beam in the undulator helps to improve transverse coherence by reducing the diffraction parameter and increase of the velocity spread. However, this will also result in the increase in saturation length. Finally, with fixed energy of the electron beam, an available undulator length will define the level of a spatial coherence and spatial jitter of the photon beam.

References

[1] A.M. Kondratenko and E.L. Saldin, *Part. Accelerators* **10** (1980) 207.

[2] Ya.S. Derbenev *et al.*, *Nucl. Instrum. Methods* **193** (1982) 415. https://doi.org/10.1016/0029-554X(82)90233-6

[3] J.B. Murphy and C. Pellegrini, *Nucl. Instrum. Methods* **A237** (1985) 159. https://doi.org/10.1016/0168-9002(85)90344-4

[4] R. Bonifacio *et al.*, *Opt. Commun.* **50** (1984) 373. https://doi.org/10.1016/0030-4018(84)90105-6

[5] R. Bonifacio *et al.*, *Phys. Rev. A* **33** (1986) 2836. https://doi.org/10.1103/PhysRevA.33.2836

[6] E.L. Saldin *et al.*, *The Physics of Free Electron Lasers* (Springer-Verlag, Berlin, 1999).

[7] M. Hogan *et al.*, *Phys. Rev. Lett.* **81** (1998) 4867. https://doi.org/10.1103/PhysRevLett.81.4867

[8] S. V. Milton *et al.*, *Science* **292** (2001) 2037. https://doi.org/10.1126/science.1059955

[9] A. Tremaine *et al.*, *Nucl. Instrum. Methods* **A483** (2002) 24. https://doi.org/10.1016/S0168-9002(02)00280-2

[10] V. Ayvazyan *et al.*, *Phys. Rev. Lett.* **88** (2002) 104802. https://doi.org/10.1103/PhysRevLett.88.104802

[11] V. Ayvazyan *et al.*, *Eur. Phys. J.* **D20** (2002) 149. https://doi.org/10.1140/epjd/e2002-00121-4

[12] V. Ayvazyan *et al.*, *Eur. Phys. J.* **D37** (2006) 297. https://doi.org/10.1140/epjd/e2005-00308-1

[13] W. Ackermann *et al.*, *Nature Photonics* **1** (2007) 336. https://doi.org/10.1038/nphoton.2007.76

[14] K. Tiedtke *et al.*, *New J. Phys.* **11** (2009) 023029. https://doi.org/10.1088/1367-2630/11/2/023029

[15] S. Schreiber and B. Faatz, *High Power Laser Sci. Eng.* **3** (2015) e20. https://doi.org/10.1017/hpl.2015.16

[16] B. Faatz *et al.*, *New J. Phys.* **18** (2016) 062002. https://doi.org/10.1088/1367-2630/18/6/062002

[17] P. Emma *et al.*, *Nature Photonics* **4** (2010) 641. https://doi.org/10.1038/nphoton.2010.176

[18] T. Ishikawa *et al.*, *Nature Photonics* **6** (2012) 540. https://doi.org/10.1038/nphoton.2012.141

[19] H.S. Kang *et al.*, Current Status of PAL-XFEL Project, Proceedings of the 5th International Particle Accelerator Conference (IPAC 2014), Dresden, Germany, June 15-20, 2014, Christine Petit-Jean-Genaz, Gianluigi Arduini, Peter Michel, Volker R.W. Shaa (Eds.), JACoW conferences, Geneva, Switzerland: CERN, paper THPRO019 (2014).

[20] Jang-Hui Han for PAL-XFEL Beam Commissioning Team, Beam Commissioning of PAL-XFEL, Proceedings of the 7th International Particle Accelerator Conference (IPAC 2016), Busan, Korea, May 8-13, 2016, Kyung Sook Kim, In Soo Ko, Kyung Ryul Kim, Volker R.W. Schaa (Eds.), JACoW conferences, Geneva, Switzerland: CERN, paper MOXBA01 (2016).

[21] D.E. Kim *et al.*, Development of PAL-XFEL Undulator System, Proceedings of the 7th International Particle Accelerator Conference (IPAC 2016), Busan, Korea, May 8-13, 2016, Kyung Sook Kim, In Soo Ko, Kyung Ryul Kim, Volker R.W. Schaa (Eds.), JACoW conferences, Geneva, Switzerland: CERN, paper THPOW45 (2016).

[22] M. Altarelli, R. Brinkmann, M. Chergui, W. Decking, B. Dobson, S. Dusterer, G. Grubel, W. Graeff, H. Graafsma, J. Hajdu, J. Marangos, J. Pfluger, H. Redlin, D. Riley, I. Robinson, J. Rossbach, A. Schwarz, K. Tiedtke, T. Tschentscher, I. Vartaniants, H. Wabnitz, H. Weise, R. Wichmann, K. Witte, A. Wolf, M. Wulff, M. Yurkov (Eds.), The European X-Ray Free-Electron Laser: Technical design report, Preprint DESY 2006-097, DESY, Hamburg, 2006 (see also http://xfel.desy.de).

[23] F. Brinker *et al.*, Commissioning of the European XFEL Injector, Proceedings of the 7th International Particle Accelerator Conference (IPAC 2016), Busan, Korea, May 8-13, 2016, Kyung Sook Kim, In Soo Ko, Kyung Ryul Kim, Volker R.W. Schaa (Eds.), JACoW conferences, Geneva, Switzerland: CERN, paper TUOCA03 (2016).

[24] R. Ganter (Ed.), Swiss FEL, Conceptual Design Report, PSI Bericht Nr. 10-04 (April 2012).

[25] E. Allaria *et al.*, *Nature Photonics* **6** (2012) 699. https://doi.org/10.1038/nphoton.2012.233

[26] K.J. Kim, *Nucl. Instrum. Methods* **A250** (1986) 396.
https://doi.org/10.1016/0168-9002(86)90916-2

[27] J.M. Wang and L.H. Yu, *Nucl. Instrum. Methods* **A250** (1986) 484. https://doi.org/10.1016/0168-9002(86)90928-9

[28] W.B. Colson, in *Laser Handbook*, Eds. W.B. Colson *et al.* (North-Holland, Amsterdam, 1990), Vol. 6, p. 115.

[29] R. Bonifacio *et al.*, *Phys. Rev. Lett.* **73** (1994) 70. https://doi.org/10.1103/PhysRevLett.73.70

[30] P. Pierini and W. Fawley, *Nucl. Instrum. Methods* **A375** (1996) 332. https://doi.org/10.1016/0168-9002(95)01221-4

[31] E. L. Saldin *et al.*, *Nucl. Instrum. Methods* **A393** (1997) 157. https://doi.org/10.1016/S0168-9002(97)00450-6

[32] E. L. Saldin *et al.*, *Opt. Commun.* **148** (1998) 383. https://doi.org/10.1016/S0030-4018(97)00670-6

[33] E.L. Saldin *et al.*, *Nucl. Instrum. Methods* **A507** (2003) 101. https://doi.org/10.1016/S0168-9002(03)00847-7

[34] E.L. Saldin *et al.*, *Nucl. Instrum. Methods* **A562** (2006) 472.
https://doi.org/10.1016/j.nima.2006.02.166

[35] S. Krinsky and R.L. Gluckstern, *Phys. Rev. ST Accel. Beams* **6** (2003) 050701.
https://doi.org/10.1103/PhysRevSTAB.6.050701

[36] S. Krinsky and Y. Li, *Phys. Rev.* **E73** (2006) 066501. https://doi.org/10.1103/PhysRevE.73.066501

[37] L.H. Yu and S. Krinsky, *Nucl. Instrum. Methods* **A285** (1989) 119. https://doi.org/10.1016/0168-9002(89)90436-1

[38] S. Krinsky and L.H. Yu, *Phys. Rev. A* **35** (1987) 3406. https://doi.org/10.1103/PhysRevA.35.3406

[39] E.L. Saldin *et al.*, *Opt. Commun.* **186** (2000) 185. https://doi.org/10.1016/S0030-4018(00)01061-0

[40] E.L. Saldin *et al.*, *Nucl. Instrum. Methods* **A507** (2003) 106. https://doi.org/10.1016/S0168-9002(03)00848-9

[41] E.L. Saldin *et al.*, *Opt. Commun.* **281** (2008) 1179. https://doi.org/10.1016/j.optcom.2007.10.044

[42] E.L. Saldin *et al.*, *New J. Phys.* **12** (2010) 035010. https://doi.org/10.1088/1367-2630/12/3/035010

[43] E.L. Saldin *et al.*, *Opt. Commun.* **281** (2008) 4727. https://doi.org/10.1016/j.optcom.2008.05.033

[44] G. Geloni *et al.*, *New J. Phys.* **12** (2010) 035021. https://doi.org/10.1088/1367-2630/12/3/035021

[45] Z. Huang and K.-J. Kim, *Phys. Rev. ST Accel. Beams* **10** (2007) 034801.
https://doi.org/10.1103/PhysRevSTAB.10.034801

[46] V. Ayvazyan *et al.*, *Nucl. Instrum. Methods* **A507** (2003) 368.
https://doi.org/10.1016/S0168-9002(03)00946-X

[47] R. Ischebeck *et al.*, *Nucl. Instrum. Methods* **A507** (2003) 175.
https://doi.org/10.1016/S0168-9002(03)00866-0

[48] M. Dohlus *et al.*, *Nucl. Instrum. Methods* **A530** (2004) 217.
https://doi.org/10.1016/j.nima.2004.04.221

[49] E.L. Saldin *et al.*, *Nucl. Instrum. Methods* **A562** (2006) 472.
https://doi.org/10.1016/j.nima.2006.02.166

[50] E.A. Schneidmiller and M.V. Yurkov, *J. Mod. Opt.* **63** (2016) 293.
https://doi.org/10.1080/09500340.2015.1066456

[51] E.A. Schneidmiller and M.V. Yurkov, Fundamental limitations of the SASE FEL photon beam pointing stability, Proceedings of the 37th International Free Electron Laser Conference (FEL 2015), Daejeon, Korea, Heung-Sik Kang, Dong Eon Kim, Schaa, R.W. Volker (Eds.), JACoW: Geneva, Switzerland, paper TUP021 (2015).

[52] E.A. Schneidmiller and M.V. Yurkov, Transverse coherence and fundamental limitatiton on the pointing stability of X-ray FELs, Proceedings of the 7th International Particle Accelerator Conference (IPAC 2016), Busan, Korea, May 8-13, 2016, Kyung Sook Kim, In Soo Ko, Kyung Ryul Kim, Volker R.W. Schaa (Eds.), JACoW conferences, Geneva, Switzerland: CERN, paper MOPOW012 (2016).

[53] A.J. Schmitt and J.H. Gardner, *Phys. Rev. A* **60** (1986) 6. https://doi.org/10.1063/1.337631

[54] R. Bonifacio *et al.*, *Nucl. Instrum. Methods* **A293** (1990) 627. https://doi.org/10.1016/0168-9002(90)90334-3

[55] W.M. Fawley *et al.*, Merits of a Sub-Harmonic Approach to a Single-Pass, 1.5-A FEL, Proceedings of the 1995 Particle Accelerator Conference, May 1-5, 1995, Dallas, Texas, USA, L.T. Gennari, R.H. Siemann (Eds.), IEEE, Piscataway, NJ, p. 219 (1995).

[56] Z. Huang and K. Kim, *Phys. Rev. E* **62** (2000) 7295. https://doi.org/10.1103/PhysRevE.62.7295

[57] Z. Huang and K. Kim, *Nucl. Instrum. Methods* **A475** (2001) 112. https://doi.org/10.1016/S0168-9002(01)01553-4

[58] H. Freund *et al.*, *Nucl. Instrum. Methods* **A445** (2000) 53. https://doi.org/10.1016/S0168-9002(00)00113-3

[59] H. Freund *et al.*, *IEEE J. Quant. Electr.* **36** (2000) 275. https://doi.org/10.1109/3.825873

[60] S. Biedron *et al.*, *Nucl. Instrum. Methods* **A483** (2002) 94. https://doi.org/10.1016/S0168-9002(02)00430-8

[61] S. Biedron *et al.*, *Phys. Rev. ST Accel. Beams* **5** (2002) 030701. https://doi.org/10.1103/PhysRevSTAB.5.030701

[62] A. Tremaine *et al.*, *Phys. Rev. Lett.* **88** (2002) 204801. https://doi.org/10.1103/PhysRevLett.88.204801

[63] W. Brefeld *et al.*, *Nucl. Instrum. Methods* **A507** (2003) 431. https://doi.org/10.1016/S0168-9002(03)00960-4

[64] E.L. Saldin *et al.*, *Phys. Rev. ST Accel. Beams* **9** (2006) 030702. https://doi.org/10.1103/PhysRevSTAB.9.030702

[65] E.A. Schneidmiller and M.V. Yurkov, Coherence properties of the odd harmonics of the radiation from SASE FEL with planar undulator, Proceedings of the 34th International Free Electron Laser Conference (FEL 2012), Nara, Japan, August 26-31, 2012, Toshinari Tanaka, Volker R. W. Schaa (Eds.), JACoW : Geneva, Switzerland, paper MOPD08 (2012).

[66] E.A. Schneidmiller and M.V. Yurkov, *Phys. Rev. ST Accel. Beams* **15** (2012) 080702. https://doi.org/10.1103/PhysRevSTAB.15.080702

[67] G. Moore, *Opt. Commun.* **52** (1984) 46. https://doi.org/10.1016/0030-4018(84)90071-3

[68] E.L. Saldin *et al.*, *Opt. Commun* **97** (1994) 272. https://doi.org/10.1016/0030-4018(93)90152-U

[69] M. Xie, *Nucl. Instrum. Methods* **A445** (2000) 59. https://doi.org/10.1016/S0168-9002(00)00114-5

[70] E.L. Saldin *et al.*, *Nucl. Instrum. Methods* **A475** (2001) 86. https://doi.org/10.1016/S0168-9002(01)01549-2

[71] K.J. Kim, *Phys. Rev. Lett.* **57** (1986) 1871. https://doi.org/10.1103/PhysRevLett.57.1871

[72] J.M. Wang and L.H. Yu, *Nucl. Instrum. Methods* **A250** (1986) 484. https://doi.org/10.1016/0168-9002(86)90928-9

[73] S. Krinsky and L.H. Yu, *Phys. Rev. A* **35** (1987) 3406. https://doi.org/10.1103/PhysRevA.35.3406

[74] J. Goodman, *Statistical Optics* (John Wiley and Sons, New York, 1985).

[75] G. Geloni *et al.*, *Opt. Commun.* **271** (2007) 207. https://doi.org/10.1016/j.optcom.2006.10.019

[76] L. Mandel, *Proc. Phys. Soc. London* **74** (1959) 223. https://doi.org/10.1088/0370-1328/74/3/301

[77] E.L. Saldin *et al.*, *Nucl. Instrum. Methods* **A429** (1999) 233.
https://doi.org/10.1016/S0168-9002(99)00110-2

[78] W.M. Fawley, *Phys. Rev. ST Accel. Beams* **5** (2002) 070701.
https://doi.org/10.1103/PhysRevSTAB.5.070701

[79] H. Wiedemann, *Synchrotron Radiation* (Springer-Verlag, Berlin, 2003).
https://doi.org/10.2172/815294

[80] E.L. Saldin *et al.*, *Opt. Commun.* **235** (2004) 415. https://doi.org/10.1016/j.optcom.2004.02.071

[81] D. Ratner *et al.*, *Phys. Rev. ST Accel. Beams* **14** (2011) 060701.
https://doi.org/10.1103/PhysRevSTAB.14.060701

[82] W.P. Robins, *Phase Noise in Signal Sources: Theory and Applications* (Peter Peregrinus, London, 1982).

[83] E.L. Saldin *et al.*, *Opt. Commun.* **202** (2002) 169. https://doi.org/10.1016/S0030-4018(02)01091-X

[84] E.L. Saldin *et al.*, *Nucl. Instrum. Methods* **A528** (2004) 355.
https://doi.org/10.1016/j.nima.2004.04.067

[85] E.A. Schneidmiller and M.V. Yurkov, Spatial properties of the radiation from SASE FELa at the European XFEL, Proceedings of the 34th International Free Electron Laser Conference (FEL 2012), Nara, Japan, August 26-31, 2012, Toshinari Tanaka, Volker R. W. Schaa (Eds.), JACoW : Geneva, Switzerland, paper MOPD06 (2012).

[86] C. Behrens *et al.*, *Phys. Rev. ST Accel. Beams* **15** (2012) 030707.
https://doi.org/10.1103/PhysRevSTAB.15.030707

[87] E.A. Schneidmiller and M.V. Yurkov, Application of statistical methods for measurements of the coherence properties of the radiation from SASE FEL, Proceedings of the 7th International Particle Accelerator Conference (IPAC 2016), Busan, Korea, May 8-13, 2016, Kyung Sook Kim, In Soo Ko, Kyung Ryul Kim, Volker R.W. Schaa (Eds.), JACoW conferences, Geneva, Switzerland: CERN, paper MOPOW013 (2016).

[88] L. Bittner *et al.*, MCP-based photon detector with extended wavelength range for FLASH, Proceedings of the 29th International Free Electron Laser Conference (FEL 2007), Novosibirsk, Russia, August 26-31, 2007, G.N. Kulipanov, N.A. Vinokurov (Eds.), JACoW : Geneva, Switzerland, paper WEPPH007 (2007).

[89] J. Wu *et al.*, LCLS X-ray pulse duration measurement using the statistical fluctuation method, Proceedings of the 32nd International Free Electron Laser Conference (FEL 2010), Malmo, Sweden, August 23-27, 2010, Leif Liljeby (Ed.), JACoW : Geneva, Switzerland, paper MOPC14 (2010).

Appendix

A Estimates of the radiation properties in the framework of the one-dimensional model

In this section, we combine the most essential formulae of the one-dimensional theory of the FEL amplifier, describing the main characteristics of the radiation. The main physical parameter of the problem is the FEL parameter ρ (see Eq. (11)) [4, 6]:

$$\rho = \frac{\lambda_{\mathrm{w}}}{4\pi} \left[\frac{4\pi^2 j_0 K^2 A_{\mathrm{JJ}}^2}{I_A \lambda_{\mathrm{w}} \gamma^3} \right]^{1/3} ,$$

where $j_0 = I/(2\pi\sigma^2)$ is the beam current density, $\sigma = \sqrt{\beta\epsilon_{\mathrm{n}}/\gamma}$ is the r.m.s. transverse size of the electron beam, and β is the external focusing beta function. The FEL parameter ρ relates to the efficiency parameter of the three-dimensional FEL theory as $\rho = \bar{\rho}/B^{1/3}$. Basic characteristics of the SASE FEL are estimated in terms of the parameter ρ and the number of cooperating electrons $N_{\mathrm{c}} = I/(e\rho\omega)$. Here

we, present a set of simple formulae extracted from [6, 29, 32]:

$$\text{Field gain length:} \qquad L_{\text{g}} \sim \frac{\lambda_{\text{w}}}{4\pi\rho} \, ,$$

$$\text{Saturation length:} \qquad L_{\text{sat}} \sim \frac{\lambda_{\text{w}}}{4\pi\rho} \left[3 + \frac{\ln N_{\text{c}}}{\sqrt{3}} \right]$$

$$\text{Effective power of shot noise:} \qquad \frac{P_{\text{sh}}}{\rho P_{\text{b}}} \simeq \frac{3}{N_{\text{c}}\sqrt{\pi \ln N_{\text{c}}}} \, ,$$

$$\text{Saturation efficiency:} \qquad \rho \, ,$$

$$\text{Power gain at saturation:} \qquad G \simeq \frac{1}{3} N_{\text{c}} \sqrt{\pi \ln N_{\text{c}}} \, ,$$

$$\text{Coherence time at saturation:} \qquad \tau_{\text{c}} \simeq \frac{1}{\rho\omega} \sqrt{\frac{\pi \ln N_{\text{c}}}{18}} \, ,$$

$$\text{Spectrum bandwidth:} \qquad \sigma_{\omega} = \sqrt{\pi}/\tau_{\text{c}} \, . \qquad \text{(A.1)}$$

The contribution of the higher odd harmonics to the total power of SASE FEL operating at saturation is described by Eq. (15). The coherence time at saturation is inversely proportional to the harmonic number, and the relative spectrum bandwidth remains constant with harmonic number.

B Estimates of radiation properties in the framework of the three-dimensional theory

Here, we present practical formulae that enable calculation of the parameters of a FEL amplifier optimized for maximum gain of the ground TEM_{00} radiation mode. The minimum gain length L_{g} of the fundamental mode and the corresponding optimum focusing beta function β_{opt} are [66, 80]:

$$L_{\text{g}0} = 1.67 \left(\frac{I_{\text{A}}}{I} \right)^{1/2} \frac{(\epsilon_n \lambda_{\text{w}})^{5/6}}{\lambda^{2/3}} \frac{(1 + K^2)^{1/3}}{K A_{\text{JJ}}} (1 + \delta) \, ,$$

$$\beta_{\text{opt}} \simeq 11.2 \left(\frac{I_{\text{A}}}{I} \right)^{1/2} \frac{\epsilon_n^{3/2} \lambda_{\text{w}}^{1/2}}{\lambda K A_{\text{JJ}}} (1 + 8\delta)^{-1/3}$$

$$\delta = 131 \frac{I_{\text{A}}}{I} \frac{\epsilon_n^{5/4}}{\lambda^{1/8} \lambda_{\text{w}}^{9/8}} \frac{\sigma_{\gamma}^2}{(K A_{\text{JJ}})^2 (1 + K^2)^{1/8}} \, . \qquad \text{(B.1)}$$

When (for technical reasons) focusing beta is $\beta > \beta_{\text{opt}}$, the gain length is:

$$L_{\text{g}}(\beta) \simeq L_{\text{g}}(\beta_{\text{opt}}) \left[1 + \frac{(\beta - \beta_{\text{opt}})^2 (1 + 8\delta)}{4\beta_{\text{opt}}^2} \right]^{1/6} \, , \qquad \text{for } \beta > \beta_{\text{opt}}. \qquad \text{(B.2)}$$

Equation (B.1) provides an accuracy better than 5% in the range of parameters given by Eq. (30). For small energy spread, $\delta \ll 1$, the diffraction parameter B, the parameter of betatron oscillations $\hat{k}_{\beta}$, the reduced saturation length $\hat{L}_{\text{sat}}$, the reduced FEL efficiency $\hat{\eta}$, the reduced coherence time τ_{c}, the radiation bandwidth σ_{ω}, and the degree of transverse coherence ζ are functions of the parameter $\hat{\epsilon} = 2\pi\epsilon/\lambda$ and the number of electrons in the volume of coherence $N_{\text{c}} = I L_{\text{g}} \lambda / (\lambda_{\text{w}} c)$:

$$B = \frac{2\bar{\Gamma}\sigma^2\omega}{c} \simeq 12.5 \times \hat{\epsilon}^{5/2} \, ,$$

$$\hat{k}_{\beta} = \frac{1}{(\beta\bar{\Gamma})} \simeq 0.158 \times \hat{\epsilon}^{-3/2} \, ,$$

$$\hat{L}_{\text{sat}} = \bar{\Gamma} L_{\text{sat}} \simeq 2.5 \times \hat{\epsilon}^{5/6} \times \ln N_{\text{c}} \, ,$$

$$\hat{\eta} = \frac{P}{(\bar{\rho}P_{\text{b}})} \simeq 0.17/\hat{\epsilon} \, ,$$

$$\hat{\tau}_c = \bar{\rho}\omega\tau_c \simeq 1.16 \times \sqrt{\ln N_c} \times \hat{\epsilon}^{5/6} \,,$$

$$\sigma_\omega = \frac{\sqrt{\pi}}{\tau_c} \,,$$

$$\zeta_{\text{sat}} \simeq \frac{1.1\hat{\epsilon}^{1/4}}{1 + 0.15\hat{\epsilon}^{9/4}} \,. \tag{B.3}$$

The gain parameter $\bar{\Gamma}$ and efficiency parameter $\bar{\rho}$ are given by:

$$\bar{\Gamma} = \left[\frac{I}{I_A} \frac{8\pi^2 K^2 A_{\text{JJ}}^2}{\lambda\lambda_w\gamma^3} \right]^{1/2} \,, \qquad \bar{\rho} = \frac{\lambda_w \bar{\Gamma}}{4\pi} \,.$$

Equations (B.1) and (B.2) should be used for the case of a finite value of the energy spread and non-optimum beta function. Correction to the coherence time and spectrum bandwidth scales as relative increase of the gain length. Spot size and angular divergence can be calculated following Ref. [85].

Properties of the higher odd harmonics for relative contributions to the total radiation power and spectral characteristics are similar to those found in the framework of the one-dimensional model. The contribution of the higher odd harmonics to the total power at the saturation is close to that given in Eq. (15) with relevant correction on effective energy spread. The coherence time at saturation is inversely proportional to harmonic number, and the relative spectrum bandwidth remains constant with harmonic number.

C Application of statistical methods for measurements of the coherence properties of the radiation from SASE FEL

Radiation from the SASE FEL operating in the linear regime has the properties of completely chaotic polarized light. Measurements of the SASE FEL gain curve enable determination of the saturation length, which is strictly connected with the coherence time. Statistical analysis of the fluctuations of the radiation energies measured with different spatial apertures allows one to determine the number of the longitudinal and transverse modes. Thus, with these simple measurements, it becomes possible to determine the degree of transverse coherence, coherence time, and photon pulse duration. In this section, we present the theoretical background and experimental results obtained at the FLASH FEL.

The amplification process in a SASE FEL starts from the shot noise in the electron beam. Initially poor, the coherence properties of the radiation are significantly improved in the exponential stage of amplification, and reach their best values at the onset of the saturation regime [41,42]. Radiation of SASE FEL consists of wavepackets (spikes) having durations of about the coherence time. Fields $\tilde{E}$ are well correlated within one spike, and are statistically independent for different spikes. Coherence properties of the radiation are described with temporal and spatial correlation functions (g_1 and γ_1), coherence time, and degree of transverse coherence (τ_c and ζ), given by Eq. (7). Radiation from a SASE FEL operating in the linear regime has properties of completely chaotic polarized light [6, 32], and the probability distribution of the radiation energy is a gamma distribution (Eq. (3)). This distribution is the function of the only parameter—the number of radiation modes, M. The parameter M is equal to the inverse squared value of the standard deviation of the radiation energy, $M = 1/\sigma_E^2$, and $\sigma_E^2 = \langle (E - \langle E \rangle)^2 \rangle / \langle E \rangle^2$.

We consider the electron bunch with Gaussian longitudinal profile of r.m.s. pulse duration σ_z. Figure 20 shows the evolution along the undulator of the radiation pulse energy, fluctuations, and r.m.s. photon pulse length. Normalized values of these parameters exhibit nearly universal dependencies for $\rho\omega\sigma_z \gtrsim 1$. A maximum of fluctuations and a minimum of the pulse duration are obtained at the end of the exponential gain regime. The saturation point (corresponding to maximum brilliance of the radiation [41]) is defined by the condition for fluctuations to decrease by a factor of three with respect to the maximum value. In the framework of the one-dimensional model, the maximum value of the coherence

time and saturation length,

$$(\tau_{\rm c})_{\rm max} \simeq \frac{1}{\rho\omega}\sqrt{\frac{\pi \ln N_{\rm c}}{18}} \; , \qquad L_{\rm sat} \simeq \frac{\lambda_{\rm w}}{4\pi\rho}\left(3 + \frac{\ln N_{\rm c}}{\sqrt{3}}\right) \; ,$$

are expressed in terms of the FEL parameter ρ [4] and the number of cooperating electrons $N_{\rm c} = I/(e\rho\omega)$ [6, 32]. Here, $\omega = 2\pi c/\lambda$ is the frequency of the amplified wave, I is the beam current, $-e$ is the charge of an electron, and $\lambda_{\rm w}$ is the undulator period. A practical estimate for parameter ρ comes from the observation that, in the parameter range of SASE FELs operating in the vacuum ultraviolet and X-ray wavelength ranges, the number of field gain lengths to saturation is about 10 [32]. Thus, the parameter ρ and coherence time $\tau_{\rm c}$ relate to the saturation length as:

$$\rho \simeq \lambda_{\rm w}/L_{\rm sat} \; , \qquad \tau_{\rm c} \simeq \lambda L_{\rm sat}/(2\sqrt{\pi}c\lambda_{\rm w}) \; . \tag{C.1}$$

For the number of modes $M \gtrsim 2$, the r.m.s. electron pulse length and minimum FWHM radiation pulse length $\tau_{\rm ph}^{\rm min}$ at the end of the linear regime are given by [86, 87]:

$$\tau_{\rm ph}^{\rm min} \simeq \sigma_z \simeq \frac{M\lambda}{5\rho} \simeq \frac{M\lambda L_{\rm sat}}{5c\lambda_{\rm w}} \; . \tag{C.2}$$

The minimum radiation pulse duration expressed in terms of coherence time (Eq. (C.1)) is $\tau_{\rm ph}^{\rm min} \simeq 0.7 \times M \times \tau_{\rm c}$.

Lengthening of the radiation pulse occurs when the amplification process enters the saturation regime. This happens as a result of two effects. The first effect is lasing to saturation of the tails of the electron bunch, and the second effect is pulse lengthening due to slippage effects (one radiation wavelength per undulator period). The effect of lasing tails gives the same relative radiation pulse lengthening as illustrated in Fig. 20. At the saturation point, pulse lengthening is about a factor of 1.4 with respect to the minimum pulse for the linear regime given by Eq. (C.1), and it is increased by up to a factor of two in the deep non-linear regime. The slippage effect is more pronounced for relative lengthening of short pulses.

The total number of modes in the radiation pulse is the product of the number of longitudinal and transverse modes, $M_{\rm Total} = M_{\rm Long} \times M_{\rm Trans}$. This is the origin of an idea to use measurements of the fluctuations of the radiation pulse energy to derive the degree of the transverse coherence. Measurements of the fluctuations of the total pulse energy and of the radiation energy after a pinhole gives us the total number of modes $M_{\rm Total}$, and the number of longitudinal modes $M_{\rm Long}$, respectively. Their ratio gives the number of transverse modes $M_{\rm Trans} = M_{\rm Total}/M_{\rm Long}$. The degree of transverse coherence is equal to the inverse value of the number of transverse modes [41]:

$$\zeta = \frac{1}{M_{\rm Trans}} = \frac{M_{\rm Long}}{M_{\rm Total}} \; . \tag{C.3}$$

Numerical simulations with code FAST [77] confirm this physical consideration. We see from Fig. C.1 that, in the exponential gain regime, the squared ratio of the fluctuations exactly follows the degree of transverse coherence calculated with rigorous statistical definition (Eq. (7)). We should stress that simple statistical measurements give the fundamental quantity without making any additional assumptions. This happens as a result of the fundamental nature (Gaussian statistics) of the light produced by the SASE FEL in the exponential gain regime. Pinhole techniques enable the evolution of the degree of transverse coherence to be traced, up to the onset of the saturation regime.

The experimental technique is as follows. The gain curve of the SASE FEL is measured at the first step (average radiation energy and fluctuations versus undulator length), and the saturation length is determined. A practical hint for determination of the saturation point is the decrease of the fluctuations by a factor of three with respect to the maximum value. Using the value of the saturation length, we derive
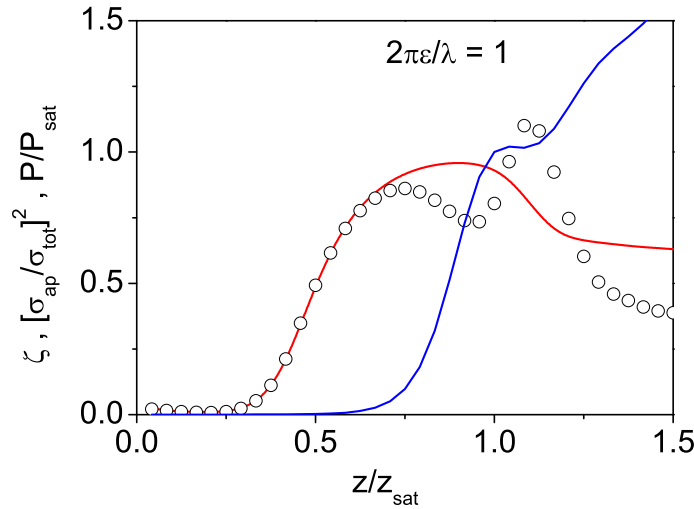
Fig. C.1: Evolution of (red) degree of transverse coherence ζ and (blue) FEL power P. Circles show ratio of fluctuations of radiation energy in pinhole to fluctuations of total energy, $\sigma^2_{E,\mathrm{ap}}/\sigma^2_{E,\mathrm{tot}}$. Simulations run with code FAST [77].

the FEL parameter ρ and coherence time τ_c (Eq. (C.1)). Then, the FEL process is stopped at the end of the high-gain linear regime (the FEL power is a factor of 20 less than the saturation level, see Fig. 20). Fluctuations are measured by using a pinhole aperture to select the central part of the photon pulse. Essential electron beam and machine parameters (charge, orbit, compression signal, RF parameters) for each shot are also recorded. The final step of the experimental procedure is the gating of the experimental results with machine parameters. The final data set contains mainly fundamental fluctuations of the radiation pulse energy related to SASE FEL process. The inverse squared value of fluctuations gives the number of longitudinal modes M_{Long}. The radiation pulse length is derived from Eq. (C.2). Additional measurements of the fluctuations for full radiation pulse energy enable determination of the number of total and transverse modes and the degree of transverse coherence (Eq. (C.3)).

Here we present the results of experimental measurements at FLASH of the number of the number of modes, coherence time, and degree of transverse coherence [86, 87]. FLASH is equipped with a set of detectors for measurements of the energy in the radiation pulse: gas monitor detector, micro channel plate (MCP) based detector, photodiode, and thermopile [14, 88]. Detectors are installed in several positions along the photon beam line. The MCP detector is installed in front of all the other detectors and is used for precise measurements of the radiation pulse energy. The MCP measures the radiation scattered by a metallic mesh (Cu, Fe, and Au targets are used) placed behind an aperture located 18.5 m downstream of the undulator. The electronics of the MCP detector itself have low noise, about 1 mV at the level of signal of 100 mV (1% relative measurement accuracy).

C.1 Measurements of the number of modes and pulse duration at FLASH [86]

The measurement procedure is organized as follows. We tune the SASE process to the maximum signal at a full undulator length of 27 m (six undulator modules). Then we apply an orbit kick (by means of switching on steerers) after the fourth undulator module, such that the FEL amplification process is suppressed in the last two undulator modules. The level of the radiation pulse energy after four undulator modules is about a factor of 20 less than the saturation level. This point corresponds to the end of the high-gain exponential regime with a minimum photon pulse length. To evaluate the number of longitudinal modes, we put a small (1 mm) aperture centred on the photon beam. Then we record radiation pulse energies (readings of the MCP detector) at this point. However, this is not all: fluctuations of the
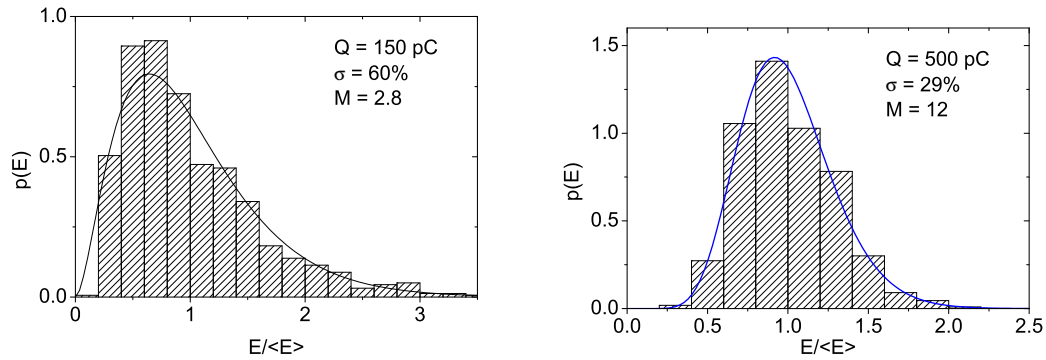
Fig. C.2: Experimental results from FLASH: probability distributions for energy in radiation pulses at end of exponential growth regime. Radiation wavelength, 13.5 nm. Left: 150 pC bunch charge. Right: 500 pC bunch charge. Solid lines show gamma distribution with $M = 2.8$ and $M = 12$ for 150 pC and 500 pC bunch charges, respectively.

electron beam and machine parameters may contribute to the fluctuations of the radiation pulse energy, but only fundamental SASE FEL fluctuations are essential for us. The final step of the experimental procedure is gating of the experimental results, enabling selection of only fundamental fluctuations of the radiation pulse energy related to the SASE FEL process. To do this, we record essential electron beam and machine parameters (bunch charge monitor readings, beam position monitor readings, readings of the pyroelectric detectors, read back values of RF parameters) for each shot, together with the readings of the MCP detector. Fluctuations of machine parameters are detected with this set of readings. If the machine (or electron beam) parameters deviate beyond a prescribed threshold, this event is excluded from data set. The number of events after the selection procedure must be sufficiently large, to provide the required statistical accuracy.

Experiments were performed for two different tunings of the beam formation system: a short pulse with 150 pC bunch charge, and a long pulse with 500 pC bunch charge. Figure C.2 shows the probability distribution of the radiation energy. Sets of raw data contained about 1400 (1700) measurements, and about 800 (550) measurements remained after the selection procedure for the 150 pC (500 pC) bunch charge. The measured number of radiation modes is 2.8 and 12 for the 150 pC and 500 pC bunch charges, respectively. Within current experimental conditions, the saturation length is estimated to be about 22 m for both cases of the bunch charge. Assuming the Gaussian shape of the lasing fraction of the electron bunch, we apply Eq. (C.2) to determine the r.m.s. electron pulse length, and obtain the following values: 6.2 μm (20 fs) and 26 μm (86 fs) for the 150 pC and 500 pC bunch charges, respectively. The FWHM pulse duration of the photon pulse in the end of the linear regime is approximately the r.m.s. electron pulse duration.

In parallel with statistical measurements, we recorded radiation spectra [86]. In the case of 150 pC, the single-shot spectra were dominated by two or three spikes. There were about ten spikes in the spectrum for the 500 pC bunch charge. Note that the spectrum is simply a Fourier transform of the temporal structure, and that the average number of spikes (modes) in the temporal domain should be about the same as the number of spikes in the spectral domain. These qualitative observations are in a good agreement with the measured number of modes.

C.2 Measurements of the degree of transverse coherence at FLASH [87]

Measurements were made in the framework of the experimental program at FLASH, with the aim of characterizing the transverse coherence of the radiation. Measurements were made in the same way as described before, except with one more statistical run with full pulse energy to define the total number
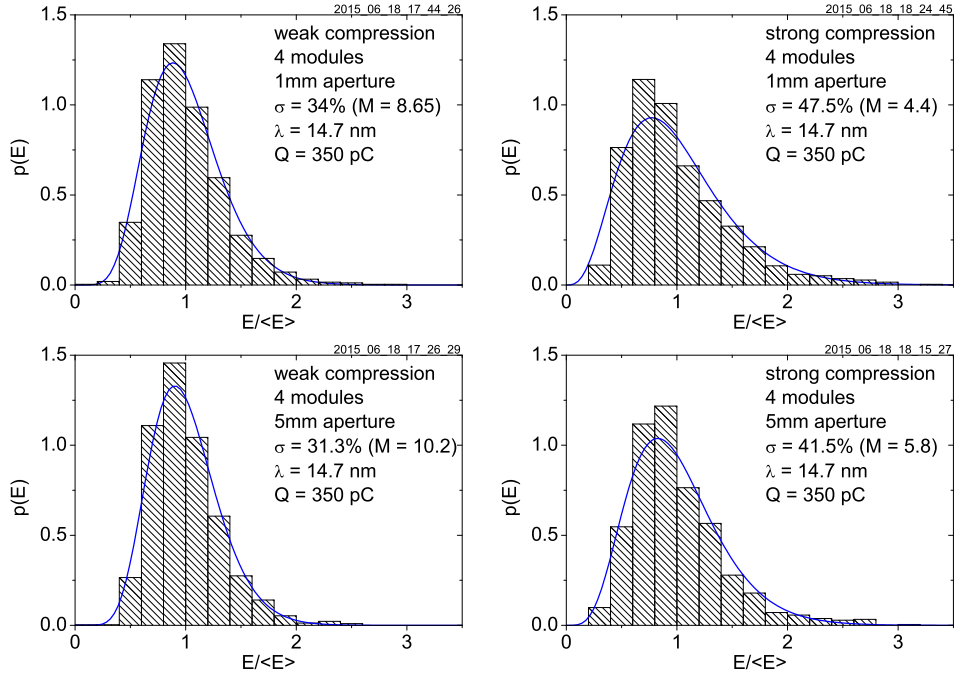
Fig. C.3: Experimental results from FLASH: probability distributions of the radiation energy. Left: weak compression. Right: strong compression. Upper and lower rows relate to pinhole and full pulse energy measurements.

of modes in the radiation pulse. Then the degree of transverse coherence is given by $\zeta = M_{\text{Long}}/M_{\text{tot}}$. Two regimes (weak and strong) of compression were characterized (see Fig. C.3). For weak and strong compression, with 1 mm aperture measurements, we find the number of longitudinal modes M_{Long}, 8.65 and 4.4, respectively. Measurements with full energy gives us the total number of modes, equal to $M_{\text{tot}} = 10.2$ for weak compression, and $M_{\text{tot}} = 5.8$ for strong compression. The ratio of these two measurements gives us the degree of transverse coherence, 85% and 75% for weak and strong compression, respectively. The obtained values are in reasonable agreement for the values expected at FLASH in these parameter range [50].

In conclusion to this section, we can state that statistical measurement is an extremely powerful tool for characterization of the main SASE FEL parameters: the FEL parameter ρ, saturation length, coherence time, photon pulse duration, and degree of transverse coherence. The method is based on the fundamental principles, and measured values have strict physical meaning (Eq. (7)). Statistical measurements have been used at FLASH since the start of its operation [10–13, 86]. There was also a trial experiment at LCLS [89]. However, FLASH is currently the only facility where statistical measurements are routinely used for SASE FEL characterization. Statistical measurements are conceptually simple, but rely on two important technical requirements. The first requirement is availability of a fast and precise radiation detector capable of measuring radiation energy of every pulse with high relative accuracy for a wide range of radiation intensities. At FLASH, we use an MCP detector with relative measurement accuracy better than 1%. The second requirement is small jitter of the machine parameters, much less than the fundamental SASE FEL fluctuations. Good phase stability of the superconducting accelerator FLASH helps a lot. In addition, the success of the technique depends on the quality of diagnostics enabling detection of jitters of the electron beam and machine parameters.